UNIVERSITÀ DEGLI STUDI DI MILANO

FACOLTÀ DI SCIENZE E TECNOLOGIE

Corso di Laurea in Fisica

Tesi di Laurea Magistrale

Observation of Superfluidity in a Dipolar Supersolid through Non-Classical Rotational Inertia

Relatori
prof. Davide Emilio GALLI
dott. Luca TANZI
prof. Giovanni MODUGNO

Studente
Julián Gabriel Maloberti
matricola: 916937

Consiglio Nazionale delle Ricerche
Istituto Nazionale di Ottica

Anno accademico 2018-2019

Summary

A supersolid is a paradoxical phase of matter proposed more than 50 years ago, which displays simultaneously two different types of order in the same single component material – solid order and superfluidity. In a seminal work of 1970, the physicist A. J. Leggett showed that a supersolid presents a superfluid fraction necessarily lower than unity even at zero temperature, originating from the breaking of translational symmetry. In particular he derived an upper limit for the superfluid fraction, and proposed an experimental procedure to observe it, by measuring a reduction of the moment of inertia under slow rotations.

Non-classical rotational effects have been searched for decades in a peculiar solid system, solid helium, where the zero-point motion of atoms is so large that was presumed to create a stable Bose-Einstein condensate of zero-point vacancies. Despite extensive efforts, experimental verification of supersolidity in solid helium has remained elusive. In 2019, the CNR-INO/LENS experimental team, where I performed this thesis work, discovered a supersolid phase in a dipolar BEC with strongly magnetic Dy atoms. The main idea is that for a peculiar regime of strong dipolar interactions the system forms an array of overlapped quantum droplets, establishing mutual coherence and breaking translational invariance, while remaining globally superfluid. So far, the superfluid nature of dipolar supersolids has been tested through the study of excitation modes not related to rotations. In particular no experiments have measured its superfluid fraction, in the spirit of the original experiments proposed by Leggett and realized (unsuccessfully) with solid helium

In this thesis I study experimentally the fate of the rotational moment of inertia in a supersolid of dipolar dysprosium atoms. In particular, I show that, as expected by Leggett in his original work, a dipolar supersolid features a reduction of the rotational inertia and maintains a finite superfluid fraction. This is done by studying a peculiar collective excitation already employed for probing superfluidity in standard superfluids: the scissors mode. This mode is a small-angle rotational oscillation in an elliptical harmonic potential. To achieve the necessary experimental conditions to excite and study the scissors oscillation in the supersolid regime, I upgraded the existing experimental setup, implementing new optical potentials for trapping and manipulating the atoms, thus realizing the excitation scheme. From the measured moment of inertia, I infer a superfluid fraction that is different from zero and of order of unity, providing direct evidence of the superfluid nature of the dipolar supersolid. Finally, I compare the measured superfluid fraction with Leggett's prediction for our system, finding agreement within an order of magnitude.

Contents

Introduction

A supersolid is a new counterintuitive phase of matter, which displays simultaneously two different types of order in the same single component material – solid order and superfluidity. In other words, in a supersolid the particles composing the rigid solid structure are not localized in a single lattice site but, can tunnel from one site to the others, flowing without friction.

The supersolid state of matter was firstly proposed by the physicists Andreev & Lifshitz [1] in solid helium, where the zero-point motion of atoms is so large that was presumed to create a stable Bose-Einstein condensate of zero-point vacancies [2], realizing a system solid and superfluid together. For decades the helium community has searched for signatures of superfluidity in solid He. In particular, in 1970 A. J. Leggett suggested an experimental procedure, the torsion oscillator experiment, to probe superfluidity in a solid system, by measuring a reduction of its moment of inertia under slow rotations [3]. In addition he suggested the lowering of the superfluid fraction of the supersolid when put into slow rotation in an annular geometry.

Despite extensive efforts, experimental verification of supersolidity in solid He has remained elusive. In 2004 Kim & Chain reported an observation compatible with the nonclassical rotational effect in a sample of solid He [4]; however their results have been refuted by subsequent analysis [5]. The consensus is now that the possible superfluid fraction of bulk solid He is below 10^{-4} [6].

The idea behind these experiments was to look for superfluidity in a system that is naturally solid, like solid He. The achievement of Bose-Einstein condensation (BEC) of neutral atoms in 1995, has given the possibility to face the supersolid problem from another point of view. Atomic BECs are naturally superfluid systems whose interparticle interactions can be manipulated in various ways. Instead of looking for superfluidity in solids, scientists have studied ways to imprint a density modulation on a natural superfluid. In 2019, the CNR-INO/LENS experimental team, who have supervised this thesis, discovered a supersolid phase in a dipolar BEC with strongly magnetic Dy atoms [7]. The main idea was to employ the anisotropic and long-range character of the interparticle interactions for imprinting a solid-like density modulation on the superfluid system [8]. In a pioneering experiment, they could spot a small range of parameters where a coherent, density-modulated state exists, thus presenting the ingredients required for a one-dimensional supersolid. The phenomenon is quite robust; it appears for different atomic species (different Dy and Er isotopes) and for different parameter values [9, 10].

So far, the superfluid nature of the supersolid has been tested through the study of

excitation modes not related to rotations, which can be described in terms of the hydrodynamic equations for superfluids [11, 12, 13]. In particular no experiments have measured the superfluid fraction of the dipolar supersolid, in the spirit of the original experiments with solid Helium.

The objective of this thesis is the implementation of an experiment measuring non-classical rotational effects when a dipolar supersolid is put into rotation, thus estimating its superfluid fraction. In the experiment we employ a specific rotation technique that fits the asymmetric, small-sized systems available in the laboratory. We excite a peculiar collective excitation, the scissors mode, a small-angle rotational oscillation in an elliptical harmonic potential that naturally holds the system. This technique, inspired by an excitation mode of nuclei, has been proposed and employed [14, 15] to demonstrate superfluidity of ordinary BECs. We study the modification of the scissors mode frequency across the transition from the BEC to the supersolid regime, so we can directly compare the supersolid with a fully superfluid system. From the measured frequency, we determine a reduced moment of inertia in both regimes, implying superfluidity of the supersolid. Next, we define a superfluid fraction specific for our system, in analogy with Leggett's prediction.

The thesis is organized as follows:

- In Chapter 1 we present the theoretical overview of the supersolid state of matter, with peculiar interest in its superfluid character. In the first part I discuss the characteristics that define a supersolid, starting with the solid and superfluid order. After an historical overview I illustrate the current state of the art of supersolids. In the second part, I will focus on its superfluid character, by firstly enunciating the properties that a wave function needs to have to show NCRI, introducing a topological demonstration for the manifestation of superfluidity. Finally, we introduce Leggett's argument that gives an upper limit for the superfluid fraction of supersolids.

- Chapter 2 is devoted to present the Bose-Einstein condensation of a dipolar quantum gas, its characteristic (long-range) interactions and Feshbach resonances, as well as its main excitations and instabilities. Then, we will introduce the main theoretical ingredients in order to obtain a dipolar supersolid from a dipolar quantum gas, and we will report on its first experimental observation. Finally, we will briefly discuss the collective excitations of a trapped superfluid as possible probes of superfluidity. In particular, we will focus on the scissors mode oscillation.

- In Chapter 3, we present the experimental ingredients to obtain a dipolar supersolid. We will first introduce the main characteristics of ^{162}Dy, the strongly magnetic element we use to produce a dipolar supersolid. Then we will give a short introduction to the cooling techniques employed to achieve a BEC of Dy atoms, and the experimental strategy implemented to obtain a dipolar supersolid. Finally, we will explain how we fit the supersolid, and its main characteristics, such as its lifetime.

- Chapter 4 presents the central results of this thesis: the measurement of the scissors frequency and of the moment of inertia of a dipolar supersolid. First I discuss the methods employed to excite the scissors mode of a BEC and a SS in order to unveil their superfluid behavior. We analyze the time-of-flight images to get information on the shape evolution and the scissors frequency of the gas. We also perform a thermal

analysis of the scissors mode in the BEC regime to confirm its superfluid character, to then focus on the modification of the scissors mode frequency across the transition from BEC to the supersolid regime.

Finally, I give some conclusive remarks and an outlook on future experiments.

The results presented in this Thesis have been the object of one article, reference [16], submitted to Science in December 2019.

Chapter 1

On the supersolid phase of matter

This chapter is divided in two parts. In the first part I will discuss the main characteristics that define a supersolid, starting with the definitions of the order in a solid and in a superfluid. Then, after a brief historical introduction with particular interest in helium, we will give the state of the art of supersolidity. In the second part we will focus on a peculiar phenomenon which defines the equilibrium properties of a superfluid: the occurrence of non-classical rotational inertia (NCRI) when put into rotation. We will enunciate the properties that a wave function needs to have to show NCRI, introducing a topological condition for the manifestation of superfluidity. We will finally use the NCRI effect to estimate the superfluid fraction of a supersolid system. Following an argument by Leggett, we will find an upper limit for NCRI. In particular we will focus on the experimental possibility to relate the NCRI phenomenon to the superfluid fraction.

1.1 Order in a supersolid

Supersolidity is a counterintuitive, macroscopic manifestation of quantum mechanics: owing to quantum physical processes, a supersolid is expected to display simultaneously two different types of order in the same single component material – solid order and superfluidity. In other words, in a supersolid the particles composing the rigid solid structure are not localized in a single lattice site but, can tunnel from one site to the others, flowing without friction. In the following I will discuss in detail the solid order and superfluidity.

1.1.1 Order in a solid

A solid is a phase of matter characterized by structural rigidity and resistance to a force applied to the surface. Its atoms are bound to each other, either in regular configuration, forming crystals, or irregularly, as occurs in glasses. Here we will focus on crystals. The fundamental property of a crystal is the periodicity of the local density $\rho(\mathbf{r})$, which determines the probability to find one particle at position $\mathbf{r}$. If one translates a gas or a liquid (or in general a system that does not brake translational invariance) by *any* vector one

statistically found the same configuration of particles, that is $\rho(\mathbf{r})$ remains unchanged. In a crystal, this is true only for a discrete sets of vectors $\mathbf{T}$, and one speaks of translational symmetry breaking of the system [17].

In order to identify the symmetry let us define the local density variation from the averaged value $\delta\rho(\mathbf{r}) \equiv \rho(\mathbf{r}) - \langle\, \rho \,\rangle$. In a homogeneous fluid $\rho(\mathbf{r}) = \langle\, \rho \,\rangle$ thus $\delta\rho(\mathbf{r}) = 0$. Instead for a crystal $\delta\rho(\mathbf{r})$ does not vanish identically and the order is expressed through

$$\delta\rho(\mathbf{r}) = \delta\rho(\mathbf{r} + \mathbf{T}) \tag{1.1}$$

where $\mathbf{T}$ sets the lattice periodicity. The condition expressed in equation (1.1) is named *density long-range order* (LRO). The vector $\mathbf{T}$ is the *order parameter* of the crystal, a quantity that defines the order.

An important point is that condition (1.1) occurs *spontaneously* in a solid, as a result of the interactions among elementary constituents, at specific thermodynamic conditions. Such a spontaneous breaking of translational symmetry is an integral part of the definition of solid, and it has two main consequences. The first one is that a crystal is macroscopically rigid, that is the system obtains the property of resistance to shear, which fluids do not possess. The second consequence is that a new kind of excitations arises, the so-called Nambu-Goldstone modes. In a crystal these modes manifest as vibrations of the lattice. This waves also referred to as phonons, play a major role in the physical properties of the crystal, for example determining its thermal and electrical conductivity.

1.1.2 Order in a superfluid

The concept of superfluidity does not describe a single phenomenon but a complex of phenomena that normally occur in conjunction, all of them related to the flow properties of the system [18]. A superfluid flows with zero viscosity: it flows through thin capillaries without apparent friction (generating a "superleak") and can flow in the form of a thin film over a rim of the bucket containing it; it has effectively infinite thermal conductivity; it also shows the phenomenon of persistent currents, i.e., a current once started in a ring is metastable and does not decay over time (astronomically speaking). It is now clear that the occurrence of superconductivity is a frictionless flow of charged particles.

However, superfluids show their most spectacular properties when put under rotation. When the angular velocity of the rotating container is small, a superfluid shows a moment of inertia smaller than a classical system: this phenomenon has been called non-classical rotational inertia (NCRI), and is one of the most striking manifestations of superfluidity. The NCRI phenomenon is different from that of frictionless flow, where the superfluid does not rotate because no energy is transferred from the container to the system. The occurrence of the NCRI effect tells that, for low velocities, no angular momentum can be carried by the ground state of a rotating superfluid. When instead the angular velocity is large, also superfluids can carry angular momentum, but in the form of quantized vortices. This effect has been measured for the first time in 1967 by Hess & Fairbank in a famous experiment where a sample of liquid helium rotating in a cylindrical container, was cooled through the lambda temperature [19].

The first superfluid discovered in nature is helium: below the lambda transition liquid helium becomes superfluid (helium II). In this sense the system can have a thermal (normal)

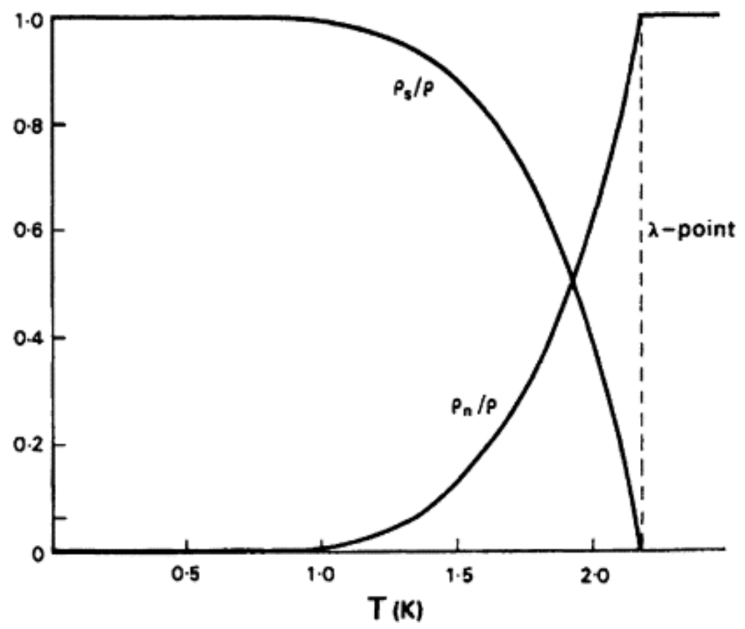

Figure 1.1: **Two-fluid model:** Here is showed the lambda transition at $T_\lambda = 2.17$ K between He I/He II and the behaviour of f_n and f_s with T. In this model a superfluid has two different components: the *normal* component (with fraction f_n) behaves as a normal fluid, and the superfluid component (with fraction f_s) carries no rotational inertia.

component and a superfluid component

$$\rho(\mathbf{r}) = \rho_s(\mathbf{r}) + \rho_n(\mathbf{r}) \tag{1.2}$$

The superfluid component carries zero inertia and zero entropy while the normal component is subject to the classical laws of physics. In figure 1.1 it is illustrated the trend of the two components with the temperature for He II. Nowadays it is known that in neutron stars there is a superfluid flow, or ultracold quantum gases are other realizations of superfluid systems.

A wealth of theoretical and experimental work, spanning now over several decades, has afforded a satisfactory theoretical understanding of the microscopic origin of superfluidity. It is now understood that superfluidity in three dimensions is a macroscopic manifestation of Bose-Einstein condensation of a large number of bosons [17]. When superfluidity appears in a system of identical fermions, condensation occurs via the creation of pairs of fermions - the *Cooper* pairs - which mechanism is described in the BCS theory. The occurrence of superfluidity in less than three dimensions is possible without the presence of condensation. Indeed in two dimensions, the condensation is forbidden according to the *Marming-Wagner theorem*. However, a system of bosons can manifest a superfluid character above the *Berezinskii-Kosterlitz-Thouless* transition.

The BEC consists of the macroscopic occupation of one single-particle quantum state - the ground-state - by a large fraction of all N particles of the system. If we consider the

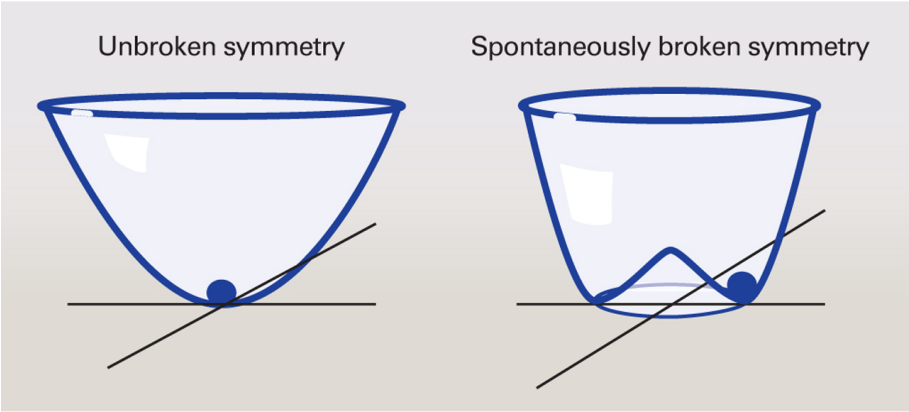

Figure 1.2: **Gauge U(1) symmetry:** Above T_c the phase φ is not defined and the system is symmetric. Below T_c the system creates the typical mexican hat potential and the system falls in one of the possible states between 0 and 2π, breaking the gauge symmetry.

one-body density matrix

$$n(\mathbf{r}, \mathbf{r}') = \langle \hat{\psi}^\dagger(\mathbf{r})\, \hat{\psi}(\mathbf{r}') \rangle \tag{1.3}$$

where the field operators $\hat{\psi}^\dagger(\mathbf{r})$ and $\hat{\psi}(\mathbf{r})$ are the creation and annihilation particles operators at position $\mathbf{r}$. It represents the probability to annihilate a particle at position $\mathbf{r}$ and to simultaneously create it at position $\mathbf{r}'$. A large single state occupation number means

$$n(\mathbf{r}, \mathbf{r}') \to n_0 \quad \text{as} \quad |\mathbf{r} - \mathbf{r}'| \to \infty \tag{1.4}$$

where n_0 is the fraction of particles that occupy the ground state: the condensed fraction. This statement implies that a macroscopic system in which a particle is removed at position $\mathbf{r}$ has a finite quantum-mechanical amplitude over a system where is removed an identical particle at an arbitrarily large distance away from $\mathbf{r}$. When this occurs it is said of *off-diagonal long-range order* (ODLRO). In short: particles are indistinguishable and completely delocalized over the sample.

Even though BEC and superfluidity are intimately related phenomena, condensed fraction should not be confused with the superfluid fraction $f_s = \rho_s/\rho$. For example in the superfluid liquid Helium, where interactions are strong, the condensed fraction is approximately 8% even at $T = 0$, while the superfluid fraction is 100%. On the other hand in BEC of weakly interacting particles, n_0 corresponds to the superfluid fraction and at T=0 approaches the value of 100 %.

In a BEC the particles behave collectively as a complex classical field. A classical field means that it is possible to describe the system with a complex order parameter $\Psi(\mathbf{r}) = f(\mathbf{r}) \exp[i\varphi(\mathbf{r})]$, whose modulus f and a phase φ are related with the density of the atoms in the BEC, $n = |f|^2$ and their velocity $\mathbf{v} \propto \nabla\varphi$. In this sense, the Bose-Einstein condensate transition spontaneously breaks the gauge U(1) symmetry. When a system has a U(1) symmetry, the absolute value of the phase of the quantum state is irrelevant, but only phase differences have a physical implication. Therefore it is invariant by any change of the phase. In figure 1.2, at the left, the quantum state (represented as a blue ball) is

in the center, thus symmetric under rotation. We have seen that in a superfluid the phase φ must be defined in the order parameter Ψ, therefore the system must choose a defined phase (on the right in figure 1.2 the blue ball is in a defined position outside the center).

Like in crystals the consequences of a broken symmetry are the imprints of a *generalized rigidity* and the appearance of new excitations. The superfluid rigidity is the stiffness to excite a single degree of freedom of the ensemble, which manifests macroscopically as its superfluid character. The new excitation appears when the superfluid is excited at low momentum. It is created a density wave - a phonon - that propagates through the system making oscillates similar to a solid.

1.1.3 Supersolids: state of the art

The supersolid phase of matter displays simultaneously the two types of order already discussed in 1.1. The first theoretical proposals suggesting the existence of such a paradoxical "superfluid quantum crystal", appeared 50 years ago [1, 2, 3]. The physical system that the scientists had in mind was solid helium, where the zero-point motion of atoms is so large that was presumed to create a stable Bose-Einstein condensate of zero-point vacancies, realizing a system solid and superfluid together (figure 1.3). For decades the helium community has searched for signatures of superfluidity in solid He. In particular, in 1970 A. J. Leggett suggested an experimental procedure to probe superfluidity in a solid system, by measuring a reduction of its moment of inertia under slow rotations [3].

Despite extensive efforts, experimental verification of supersolidity in solid He has remained elusive [6]. Following the original suggestion by Leggett, in 2004 Kim & Chain reported on an observation compatible with non-classical rotational effects in a sample of solid He [4]. The experimental set-up consists of a torsional oscillator containing a cylindrical cell filled with solid He (figure 1.4.a). The period τ of the oscillator is related to the rotational inertia I through the relationship $\tau = 2\pi\sqrt{I/K}$, where K is an elastic constant determined mainly by the rigidity of the rod. They reported a decrease of the period oscillation below a temperature of the order of 100 mK, with a shift proportional to the temperature (figure 1.4.b). Despite the phenomenon was initially attributed to the presence of a finite superfluid fraction, their results have been refuted by subsequent analysis, relating the period oscillation decrease with an increase of the elastic constant K [5]. The consensus is now that the possible superfluid fraction of bulk solid He is below 10^{-4} [6, 17, 20]. The helium community is now studying the behavior of a He monolayer on graphite, which had been suggested to support supersolidity, and is indeed showing interesting signals [21], although there is an ongoing debate about its real nature.

The idea behind these experiments was to look for superfluidity in a system that is naturally solid, solid He. In 1995, the physicists Ketterle, Wieman, and Cornell achieved Bose-Einstein condensation (BEC) in atomic gases, realizing for the first time a system which is naturally superfluid and where the inter-particle interactions can be manipulated in various ways. As a result, the supersolid problem has been approached from another point of view: instead of looking for superfluidity in solids, scientists have studied ways to imprint a density modulation on a natural superfluid. The majority of the proposals appeared in the last 20 years deal with BECs with some special kind of inter-particle interactions, providing a characteristic length-scale at which the energy of the BEC is minimized by an emergent solid-like density modulation. Few examples are Rydberg atoms

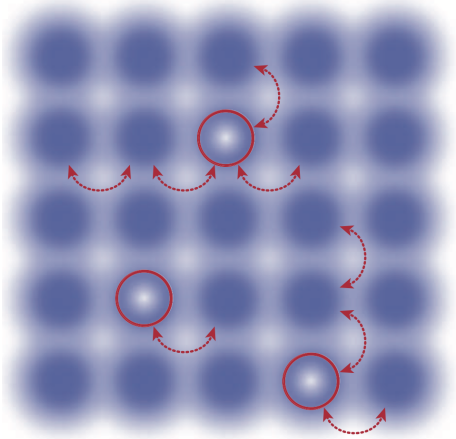

Figure 1.3: **Quantum tunneling of vacancies.** In the original model of supersolidity, the number of atoms is less than the number of lattice sites. The lattice thus contains vacancies (red circles), which are able to exchange their positions with neighbouring atoms (blue dots) so easily that they are delocalized throughout the whole system. These vacancies are bosons, which at low temperatures may form a Bose–Einstein condensate. As a result, the atoms themselves are not localized at particular sites as in a classical lattice. Some of the mass can flow without friction through the rest, which remains a rigid solid. Taken from [6].

[22], cavity-coupled gases [23], spin-orbit coupled systems [24], and dipolar gases [8, 25].

In 2017 Ketterle and Esslinger reported the creation of an ultracold quantum gas with supersolid properties. Esslinger placed a Bose-Einstein condensate inside two coupled optical cavities, and the gas acquired modulation without losing its superfluidity [26]. Ketterle instead used the coupling between an external field and an intrinsic property of the atoms, the spin-orbit coupling, to create a periodic interference between them, hence the characteristic modulation of the wave function [27]. However, in both systems the inter-atomic interactions are mediated by a light field; as a result, the emerging lattice structure is rigid and cannot carry elastic waves [28], preventing the non-trivial coupling between liquid and solid characters.

Better candidates for supersolidity are BECs of magnetic atoms with strong dipole-dipole interactions [8]. When a magnetic BEC is confined in the direction of polarization of the dipoles, the interplay of dipolar and contact interactions gives rise to a roton minimum in the dispersion relation, introducing a natural length scale for self-organization [8]. Seminal experiments have recently observed the roton spectrum [29], the roton instability [30] and the formation of quantum droplets arrays in the post-instability dynamics [31]. These droplets, also observed in mixtures of BECs [32, 33], are however typically strongly bound due to the competition of mean-field interaction and quantum fluctuations [34]. Therefore, they lack the mutual coherence necessary for a supersolid [35].

In 2019, the CNR-INO/LENS experimental team, who have supervised my theses, discovered a supersolid phase in a dipolar BEC with strongly magnetic Dy atoms. The main idea was to find an interaction regime of extremely weakly bound droplets, in order to

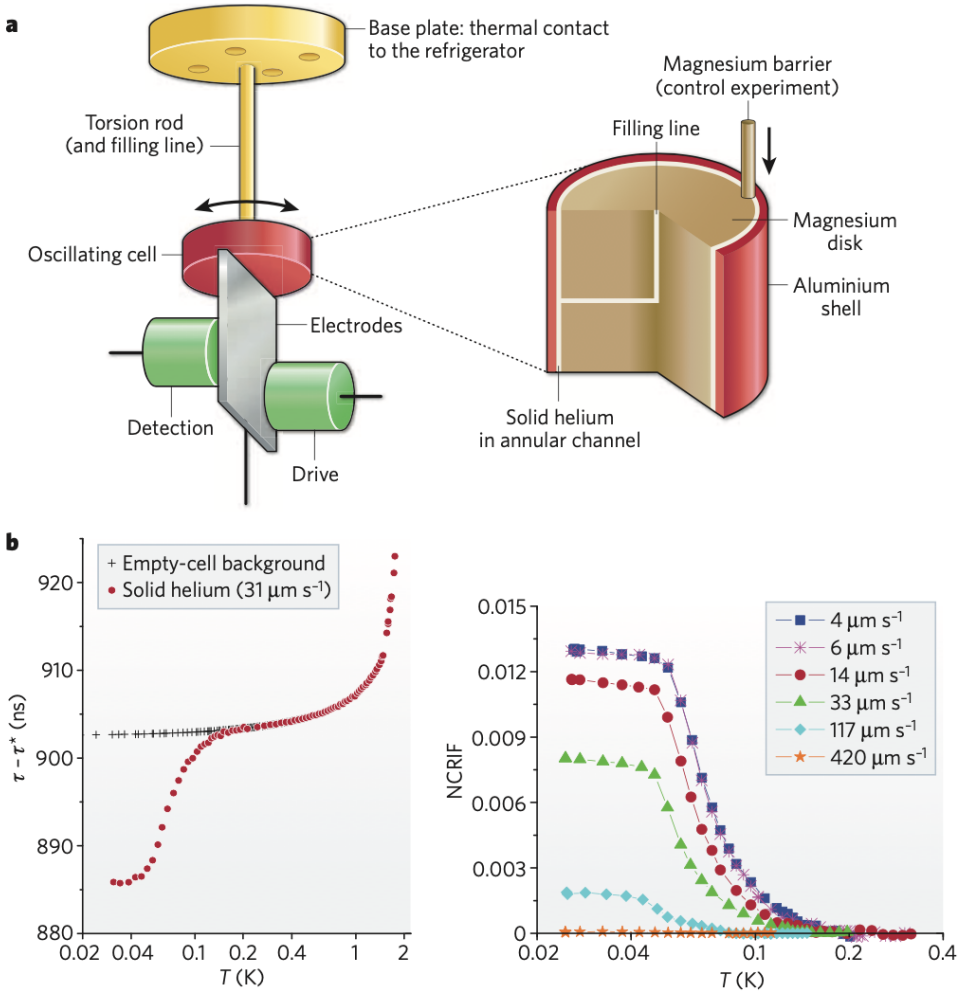

Figure 1.4: **Torsion oscillator experiment: a)** Typical setup of the torsion oscillator experiment carried by Kim & Chain. **b)** Left: Below a certain critical temperature, they observed a reduction of the period of oscillation τ, indicating the presence of the NCRI effect. The period is proportional to $\tau \propto \sqrt{I/K}$, with I the inertia and K the elastic constant of the solid. Right: The respective (supposed) superfluid fraction for different angular velocities. It has been pointed out afterward that the decrease of the oscillation period is a consequence of the hardening of the crystal (an increase of K) and not to the NCRI effect (decrease of I). Taken from [6].

increase their capability to overlap and establish mutual coherence. In a pioneering experiment, they could spot a small range of parameters where a coherent, density-modulated state exists, thus presenting the ingredients required for a one-dimensional supersolid [7]. Rapidly, these findings have been replicated by other experiments [9, 10], raising a lot of interest in the scientific community. The phenomenon is quite robust; it appears for different

atomic species (different Dy and Er isotopes) and for different parameter values. The lifetime is of the order of 100-200 ms, long enough to allow further experimental investigation of the properties of supersolids.

What sets dipolar supersolids apart from the previous experiments is that no external influence is needed to generate the density modulation, but it naturally arises from the inter-atomic interactions. Recent experimental investigations have demonstrated the appearance of two distinct Goldstone modes due to the simultaneous occurrence of superfluid and solid order [11, 12, 13]. These results show that in dipolar supersolids the superfluid and solid characters are coupled. Very importantly, these works directly demonstrate that the supersolid lattice is compressible, as expected for He supersolids and differently from supersolids with light-mediated interactions.

Despite these initial accomplishments, many questions still remain. In particular, no experiments have measured the superfluid fraction of the dipolar supersolid, in the spirit of the original experiments with solid Helium. This is the objective of my Thesis: to implement an experiment able to measure non-classical rotational inertia in a dipolar supersolid, and estimate its superfluid fraction, so as to close the loop with respect to the initial works.

1.2 Non-classical rotational inertia as probe to superfluidity

As introduced in section 1.1.2, one of the key manifestations of superfluidity in liquids and gases is the reduction of their moment of inertia under slow rotations. In this section we will focus on this peculiar property of superfluids: we will show that the NCRI effect is a proper definition of superfluidity (since it is directly related to the topological properties of the superfluid wavefunction) and can be employed to quantify the superfluid fraction. We will then investigate the NCRI effect in a supersolid. Since the supersolid wavefunction is modulated, the superfluid fraction is expected to be smaller than one, even at zero temperature. Following the original work by Leggett, we will show that the measurement of the NCRI effect in a solid can be used to estimate its superfluid fraction, therefore assessing its supersolid character. Finally, we will also derive an upper limit for the superfluid fraction of a one-dimensional supersolid in an annular geometry. A similar calculation will be used in chapter 4 to estimate the superfluid fraction of a dipolar supersolid.

1.2.1 Non-classical rotational inertia

To introduce what is meant by NCRI let us imagine this simple experiment, known as the torsion oscillator experiment. We take an empty cylinder container and put it on the axis of a rotative platform. When the platform starts rotating (at sufficiently low speed) the container follows almost instantaneously the rotation, and no energy is dissipated as heat. We now repeat the experiment with the container filled with a normal liquid. At first, the fluid will stay at rest (in the lab frame). Although some energy is dissipated as heat in bringing the liquid into rotation, after long enough time equilibrium is reached and the fluid and the container will rotate with the platform.

As already discussed, in 1967 Hess & Fairbank tried this experiment with ^{4}He. They

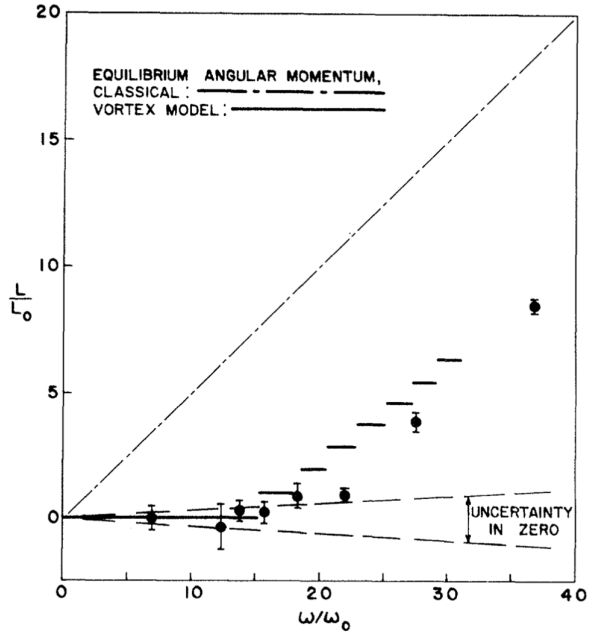

Figure 1.5: **Hess & Fairbank experiment:** Angular momentum L of the superfluid versus angular velocity ω of the rotor, after helium is cooled in rotation.The dashed line is the angular momentum of a classical system. The solid line segments are the equilibrium state predicted by the vortex model. Taken from [19].

started rotating slowly a container filled with liquid He and gradually lowered the temperature. While above the lambda transition (in the He I phase) the system was rotating with the container as a normal fluid, below $T_\lambda = 2.17$ K (in the He II phase) they observed that He gradually stopped the rotation. Eventually, at $T \to 0$, it was stationary in the lab frame (see figure 1.5), showing that the equilibrium behavior of the system has zero rotational inertia. Remarkably, the container didn't just start rotating from rest for $T < T_\lambda$. If that were the case, the experiment could have been interpreted as the manifestation of the absence of viscosity in He II, still a superfluid effect, but different from NCRI. A fluid with zero viscosity is a system with zero internal frictional force and no resistance to a shear stress when perturbed below a certain velocity (the Landau critical velocity in the case of a superfluid). Instead, the Hess & Fairbank experiment shows the true equilibrium behavior of a superfluid, and gives information on the nature of its wavefunction [3].

As discussed in section 1.1.2, the superfluid phase is characterized by what one might call "generalized BEC". As a consequence, a superfluid can be described by the BEC order parameter, and the superfluid velocity is, by definition, the gradient of the phase

$$\mathbf{v}_s = \frac{\hbar}{m}\boldsymbol{\nabla}\varphi \tag{1.5}$$

Since the velocity is proportional to the gradient of a scalar quantity, it follows that the superfluid flow must be irrotational: $\boldsymbol{\nabla} \times \mathbf{v}_s = 0$. Therefore, the circulation around any closed loop in the superfluid is proportional to the total phase difference around the loop.

Since the phase φ of the order parameter must be single-valued module 2π, integration of equation (1.5) leads to the Onsager-Feynman quantization condition for the superfluid velocity

$$\oint \mathbf{v}_s \, dl = \frac{h}{m} n \tag{1.6}$$

where n is a positive integer. For a cylindrical superfluid rotating at low angular velocities, $\omega \to 0$, this prescription turns into a vanishing of both angular momentum L and moment of inertia $I = \langle L \rangle / \omega$: the superfluid shows NCRI. A finite value of the angular momentum can appear only for sufficiently large ω at integer multiples of the reduced Planck constant $\hbar$, through the occurrence of quantized vortices.

As shown in figure 1.5, with their experiment of Hess & Fairbank showed that when the system is rotated at $\omega < \omega_c$, no vortex is created and the angular momentum of the fluid is transferred to the walls of the container, while the superfluid gradually stopped the rotation. Only when rotated at $\omega > \omega_c$ the system acquires a quantized angular momentum though the creation of vortices [19].

1.2.2 NCRI and superfluid fraction

In the previous section we have introduced phenomenologically the Hess & Fairbank experiment and related the occurrence of NCRI to the irrotational character of the velocity flow in a superfluid. In this section we will directly use the NCRI phenomenon to define the superfluid fraction of the system. Also, we will show that the occurrence of NCRI in a quantum system gives a direct clue to the topological nature of its ground-state wavefunction.

To be more quantitative, let us consider N particles with mass m in a cylinder container with radius R and thickness d, and take $d \ll R$, like in figure 1.6. When put into rotation at low angular velocities the classical momentum of inertia is defined in the common way as $I_c = NmR^2$, and the classical rotational energy $E_c = E_{\text{lab}} - E_0$ reads

$$E_c = \frac{1}{2} I_c \, \omega^2 \tag{1.7}$$

where E_0 is the energy for $\omega = 0$ and E_{lab} is the energy measured in the laboratory frame.

If our system is governed by quantum mechanics than we need a more general definition of rotational inertia than I_c. We may assume from symmetry arguments that the energy of rotation is proportional to ω^2 for small ω, so we can define a moment of inertia I by the relation

$$I = \lim_{\omega \to 0} \left(\frac{\partial^2 E}{\partial \omega^2} \right) \tag{1.8}$$

By measuring the total momentum of inertia $I = \langle L \rangle / \omega$ in the lab frame, it is possible to quantify the *superfluid fraction* defined in (1.2). The definition reads

$$f_s = \frac{\rho_s}{\rho} = \left(1 - \frac{I}{I_c} \right) \tag{1.9}$$

Note that for $f_s = 0$ the system is normal, while for $f_s = 1$ the system stays at rest in the lab frame (but rotates in the opposite direction in the rotating frame).

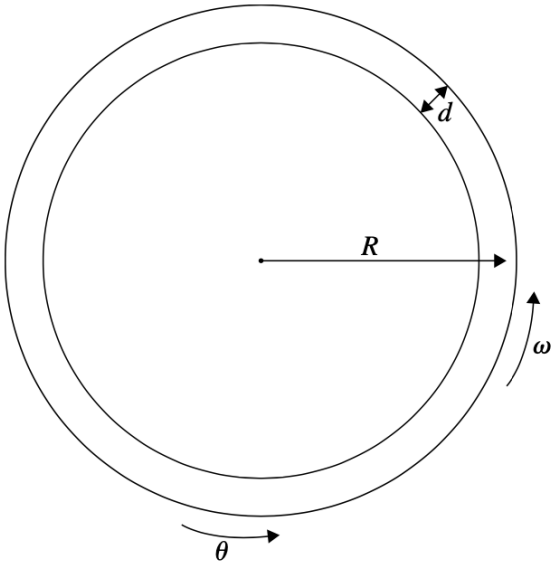

Figure 1.6: **One dimensional ring:** The ring geometry treated here. With periodic boundary conditions this system can represent an infinite one dimensional superfluid. Taken from [18]

Now we want to investigate what properties a system must have to show NCRI, and further how these properties determine the superfluid wave function. To do so we construct a trial wave function $\Psi(\mathbf{r}_1, \mathbf{r}_2, ..., \mathbf{r}_N)$ which minimizes the energy of the system. In the following, we will consider cylindrical coordinates: $\mathbf{r}_i \to (r_i, z_i, \theta_i)$, and for simplicity, we will not write the dependence on r_i, z_i where it is understood.

Let us consider first the system at rest. The ground state wave-function Ψ_0 obeys the time-independent Schrödinger equation $\hat{H}\Psi_0 = E_0\Psi_0$. This function must satisfy two conditions:

- The symmetry condition for a bosonic system:

$$\Psi_0(\theta_1, ..., \theta_i, \theta_j, ..., \theta_N) = +\Psi_0(\theta_1, ..., \theta_j, \theta_i, ..., \theta_N) \tag{1.10}$$

- The single-valuedness boundary condition (SVBC):

$$\Psi_0(\theta_1, ..., \theta_i + 2\pi, ..., \theta_N) = \Psi_0(\theta_1, ..., \theta_i, ..., \theta_N) \tag{1.11}$$

The SVBC says that if we take one particle once round the ring, holding all the others fixed, we must come back to the wave function with which we started. Apart from these conditions, we know that Ψ_0 can be taken real, and, for a Bose system, nodeless.

Let us now consider the situation where the walls are rotating with angular velocity $\omega < \omega_c$. The Schrödinger equation is now time-dependent in the lab frame, so, to solve the problem we must transform it into the frame of the rotating walls and seek the ground state in that frame. The rotating wave function $\Psi_0'(\theta_1', ..., \theta_N')$ obeys the new Schrödinger

equation $\hat{H}'\Psi_0' = E_0'\Psi_0'$, with the new rotating Hamiltonian $\hat{H}' = \hat{H} - \boldsymbol{\omega} \times \hat{\mathbf{L}}$, and subject to a changed SVBC

$$\Psi_0'(\theta_1', ..., \theta_i' + 2\pi, ..., \theta_N') = \exp[-2\pi i\, \alpha]\, \Psi_0'(\theta_1', ..., \theta_i', ..., \theta_N') \tag{1.12}$$

where $\alpha = \omega/\omega_c = \omega m R^2/\hbar$. As a result, the ground state energy in the rotating frame E_0' is now in general a function of ω: $E_0' = E_0'(\omega)$. Moreover the energy in the lab frame E_{lab} is related to $E_0'(\omega)$ by

$$E_{\text{lab}} = E_0 + E_c - \left[E_0'(\omega) - E_0\right] \tag{1.13}$$

where $-\left[E_0'(\omega) - E_0\right]$ is the energy deviation from a normal system. Therefore, there are two different cases which can occur for $\omega \neq 0$:

- Rigid rotation (solid or fluid): $\omega \neq 0$ and $E_0'(\omega) = E_0 \;\rightarrow\; E_{\text{lab}} = E_0 + E_c$
- NCRI effects (superfluid): $\omega \neq 0$ and $E_0'(\omega) > E_0 \;\rightarrow\; E_{\text{lab}} < E_0 + E_c$

Thus the occurrence of NCRI, in general, lowers the ground state energy in the lab frame from the classical value, until for $f_s = 1 \rightarrow E_{\text{lab}} = E_0$, $\forall\omega < \omega_c$. Inserting (1.8) into the definition of the superfluid fraction (1.9), and using the equation (1.13) for the energy we get

$$f_s = \lim_{\omega\to 0} \frac{1}{I_c}\left(\frac{\partial^2 E_0'(\omega)}{\partial\omega^2}\right) \tag{1.14}$$

hence if $E_0'(\omega)$ is independent of ω, the system can not be superfluid and the particles follow the rotating container at any angular velocity. Instead, in the truly ground state of a perfect superfluid ($f_s = 1$) the inertia is zero and the fluid stays at rest in the lab frame.

1.2.3 Superfluidity and topology

In the previous section, we have seen that a system can rotate in two ways: classically or with NCRI. Now we will discuss how these two different rotational properties are correlated with the ground state wave function of the system Ψ_0. What we have to do now is to solve the original Schrödinger equation subject to the altered SVBC (1.12), in order to account for the system's rotation. Intuitively, we have to put enough extra "kinks" in the wave function to fulfill the SVBC, while keeping the extra energy to a minimum.

It helps to draw a diagram of the ground state wavefunction in the rotating frame Ψ' (see figure 1.7). The axes of the diagram correspond to the variable θ_1 and θ_2, and we denote by heavy dots the "lattice points" $(2n\pi, 2m\pi)$. Due to the SVBC the wave function is always completely specified by its behavior in the first cell OABC. Moreover, because of symmetry conditions, it is always symmetric with respect to reflection in the line OB, hence it is completely specified by its value in the octant OAB.

If we split the wave function by its amplitude $f(\mathbf{r})$ and the phase $\varphi(\mathbf{r})$, the SVBC (1.12) says that irrespective of α (thus ω), f must be unaffected by translation by a lattice vector, e.g., $f(O) = f(A)$. For the ground state Ψ_0 also the phase must be unaffected by a lattice translation. For Ψ_0' in the rotating frame, a translation by a lattice vector must increase φ by $2\pi\alpha$. Thus if $\varphi(O) = 0$, then $\varphi(A) = 2\pi\alpha$ and $\varphi(B) = 4\pi\alpha$. As a consequence, the

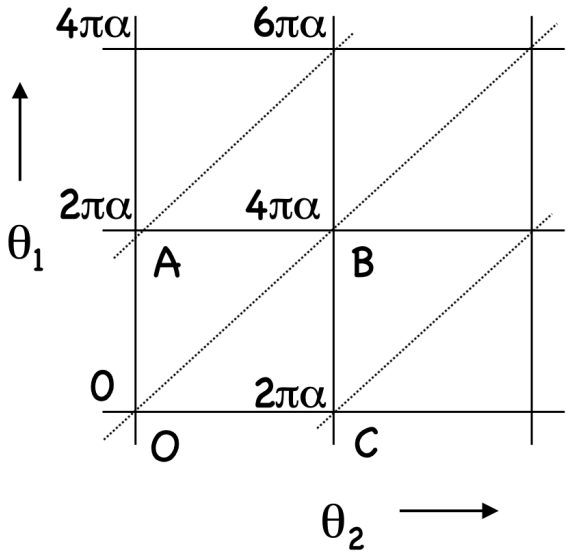

Figure 1.7: **Two-dimensional topology diagram:** The axes of the diagram correspond to the variable θ_1 and θ_2, and we denote to heavy dots the lattice points $(2n\pi, 2m\pi)$. Thus O is the point (0,0), A is $(2\pi, 0)$, C is $(0, 2\pi)$, and B is $(2\pi, 2\pi)$.

behaviour of the system under rotation depends on the topological properties of the wave function. Now three different situations can arise:

(1) The system can modify trivially its ground state Ψ_0 to meet the altered SVBC, without expenditure of energy. This situation occurs when Ψ_0 is localized in a region small compared to the unit cell and drops off exponentially outside. We can, therefore, change the phase of the wave function in the region where Ψ_0 is exponentially small to fulfill the altered SVBC at no extra cost in energy $(E'(\omega) - E_0)$. In this case $\Psi'_0 = \Psi_0$, and if the rotating boundary conditions are switched on suddenly, the system follows adiabatically and does not dissipate energy in coming into equilibrium. This is the situation characteristic of a normal solid.

(2) The original ground state wave function can not be trivially modified without expenditure of energy. This situation occurs when Ψ_0 is not localized but has non-trivial nodal hyperplanes so that we cannot move from O to A,B, etc without crossing at least one such hyperplane. We can, therefore, put $f' = f$ everywhere, and $\varphi' = \varphi$ at one side of the nodal hyperplane and $\varphi' = \varphi + 2\pi\alpha$ on the other. The discontinuity occurs where $\Psi_0 = 0$, and therefore costs no extra energy. Then the system will not follow adiabatically the boundary conditions when they are suddenly switched on, but after a sufficiently long time, the system will rotate with the container. This means that energy is dissipated as heat in bringing the system into equilibrium. This situation is typical of a normal liquid.

(3) There is no wave function that obeys the modified SVBC and yields $E'_0(\omega) = E'_0$. In this case, the system stays in the ground state and modifies it. Since this costs energy, $E'_0(\omega) \neq E'_0$ and f_s is finite. Ψ_0 is such that there exist at least some paths leading from O to A such that Ψ_0 is everywhere larger or equal than a constant on these pats. Now, at least in the regions where Ψ_0 does not vanish, an arbitrary wave function can be

written in the form $\Psi_0' = A\exp[i\Phi]\Psi_0$. Where A and Φ are functions of $(\mathbf{r}_1, \mathbf{r}_2, ..., \mathbf{r}_N)$ and $\Phi(...\theta_i + 2\pi...) = \Phi(...\theta_i...) + 2\pi\alpha$. Choosing $A = 1$ and using the reality of Ψ_0 we find

$$E'(\omega) - E_0 = \int d\theta_1 ... d\theta_N \sum_i \left(\frac{\partial\Phi}{\partial\theta_i}\right)^2 \Psi_0^2(\theta_1 ... \theta_N) \tag{1.15}$$

But we have

$$\int_0^{2\pi} d\theta_i \left(\frac{\partial\Phi}{\partial\theta_i}\right) = 2\pi\alpha \ (\mathrm{mod}\ 2\pi) \tag{1.16}$$

and, by hypothesis, at least on some paths going from 0 to 2π, Ψ_0^2 is finite. Then the right hand of equation (1.15) is finite. Thus $E_0'(\omega)$ depends non-trivially from ω and the system shows NCRI. This is a *sufficient* condition for superfluidity in the sense of NCRI at $T = 0$. We can say that this is the *definition* of superfluidity.

To sum up: the equilibrium behavior under slow rotation of a quantum system at $T = 0$ is determined by the ground state wave function Ψ_0. If Ψ_0 vanishes (or becomes exponentially small) on all paths leading from $\theta_i \to \theta_i + 2\pi$, the system is normal; otherwise it is superfluid. In other words, if we can find a way of taking one particle around the ring, arriving back at the situation where all other particles are in their original position, in such a way that Ψ_0 remains finite, then the system is superfluid. Otherwise, it is normal.

Following this criterion, one finds that no Bose system can be normal at $T = 0$. Due to the property of ODLRO, the ground state wave function Ψ_0 of a BEC is always nodeless, thus it is included into the case **(3)**. Hence we can say that *BEC implies superfluidity*, in the sense of NCRI. Now let us examine how the NCRI effect manifests in a supersolid.

1.2.4 NCRI in a supersolid

In 1970, Leggett suggested that "the property of non-classical rotational inertia possessed by superfluid liquid helium may be shared by some solids" [3]. Leggett was thinking about supersolidity in solid He. In his seminal paper, he showed that such a supersolid (a solid with non-zero NCRI) should possess a superfluid fraction smaller than unity even at zero temperature, due to the modulated nature of the wavefunction. He also suggested the way to measure the presence of a finite superfluid fraction, by measuring the NCRI effect with a torsion oscillator experiment, similar to the one performed by Hess & Fairbank for a purely superfluid sample.

I will now follow Leggett's argument, in order to derive an upper bound for the superfluid fraction in a (density modulated) supersolid sample. The calculation is performed in the same geometry introduced in section 1.2.2. We consider N particles with mass m in a cylinder container with radius R and thickness d, with $d \ll R$ as in figure 1.6. We however consider a solid system, that is the density $\rho(\mathbf{r})$, does not tend to a constant value even deep inside the sample (in other words $\rho(\mathbf{r})$ shows strong variations over the sample, which is different than saying that the atoms are localized). The Hamiltonian of this system is

$$\hat{H} = -\frac{\hbar^2}{2m}\sum_{i=1}^{N}\nabla_i^2 + \frac{1}{2}\sum_{i,j=1}^{N} U(\mathbf{r}_i - \mathbf{r}_j) + \sum_{i=1}^{N} V(\mathbf{r}_i) \tag{1.17}$$

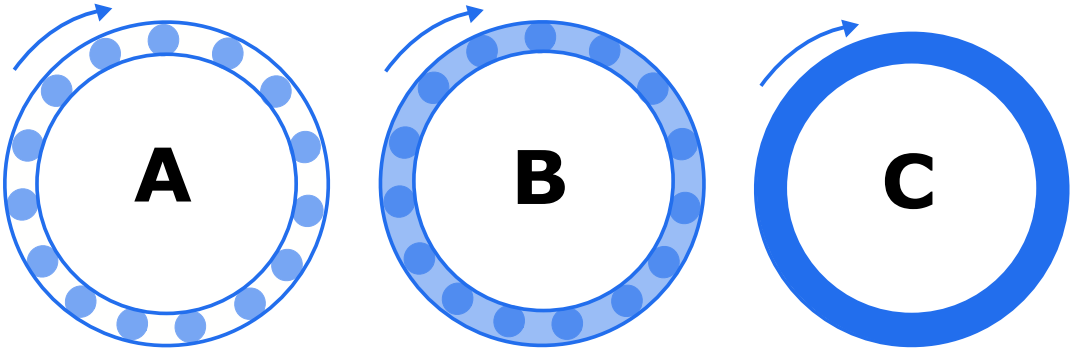

Figure 1.8: **Superfluid in a 1D ring:** Here it is shown the case of a superfluid in a rotating annulus with (A) separated superfluid droplets ($Q_0 = 0$), (B) modulated wave function but globally coherent ($0 < Q_0 < 1$), and (C) homogeneous superfluid ($Q_0 = 1$).

where the first term is the kinetic energy, U is the interparticle interaction and V is the time-independent external potential. As in section 1.2.2, we construct a trial wavefunction Ψ_0 satisfying the altered boundary conditions (1.12), in the form:

$$\Psi_0'(\mathbf{r}_1, ..., \mathbf{r}_N; \omega) = \exp\Big[i \sum_{i,j=1}^{N} \varphi(\mathbf{r}_i; \omega)\Big] \Psi_0'(\mathbf{r}_1, ..., \mathbf{r}_N) \tag{1.18}$$

where φ satisfies the boundary conditions (1.12). When applying Ψ_0 to the Hamiltonian, we obtain that the energy is:

$$\langle H \rangle = E_0 + \frac{\hbar^2}{2m} \int (\nabla\varphi)^2 \rho(\mathbf{r}) d\mathbf{r} \tag{1.19}$$

Since we are neglecting terms in d/R the problem is unchanged if we "unroll" the annulus to form a rectangular parallelepiped of length $2\pi R$, and change the boundary conditions (1.12) in:

$$\varphi(2\pi R, y, z) = \varphi(0, y, z) - 2\pi\alpha \tag{1.20}$$

where x, y, and z are Cartesian coordinates and x runs from 0 to $2\pi R$. We then apply standard variational methods to choose φ so as to minimize (1.19). Because of the symmetric character of $\rho(\mathbf{r})$ we can focus on the supersolid unit cell. Assuming a unit cell with axes a, b and c parallel to the x, y and z directions respectively, we introduce the normalized coordinates $x' = x/a$; $y' = y/b$; $z' = z/c$ and normalized density $\rho'(\mathbf{r}) = \rho(\mathbf{r})/\langle\rho\rangle$. We find

$$\langle H \rangle = E_0 + \frac{1}{2} N m R^2 \omega^2 Q_0 \tag{1.21}$$

where

$$Q_0 = \left[\int_0^1 \frac{dx'}{\int_0^1 \int_0^1 \rho'(\mathbf{r}) dy' dz'} \right]^{-1} \leq 1 \tag{1.22}$$

comparing (1.21) with (1.14) we get

$$f_s \leq Q_0 \tag{1.23}$$

Note that for a homogeneous superfluid where $Q_0 = 1$ we have the trivial result $f_s \leq 1$ (figure 1.8.C). If instead the wavefunction is modulated, the value of Q_0, and therefore the superfluid fraction, diminishes (figure 1.8.B). In the limit of a vanishing density for some $\mathbf{r}$ in the unit cell, $Q_0 = 0$ and the system behaves as non-superfluid (figure 1.8.A). In general the quantity Q_0 becomes very small when there exists any yz plane in the unit cell near which there is very small probability of finding an atom. In other words, it is extremely small unless there is an appreciable probability of "exchange" of particles between sites. However, it is important to remark that is the lack of translational invariance of the ground state wave function, not that of the Hamiltonian, that reduces the value of the superfluid fraction.

In 1970, Leggett calculated the value of Q_0 for the case of solid Helium, using its known exchange constant and lattice constant. He found an upper bound for the superfluid fraction in solid He of the order: $f_s < 3 \times 10^{-4}$. Remarkably recent experiments have not observed a superfluid fraction in solid He-4 above this value. A similar quantity can be computed also for the case of a dipolar supersolid, where the unit cell is not composed by a single atom, but by a superfluid cluster of many atoms. For this reason in dipolar supersolids Q_0 is expected to be much larger than in solid He. The precise calculation of this quantity for a dipolar supersolid is reported in Chapter 4, together with the experimental measurement.

Chapter 2

From Bose-Einstein condensation to supersolidity

Previous reports of supersolid-like states in Bose-Einstein condensates used external influences to induce the modulation of the wave function [26, 27]. What sets dipolar supersolids apart from other cold-atom experiments is that no external influence is needed to generate this modulation, but naturally arises from internal interactions. As a consequence, in dipolar supersolids, the emergent crystalline structure, which spontaneously breaks the translational invariance typical of a uniform gas, is deformable.

In this chapter, we will introduce Bose-Einstein condensation in a dipolar gas, and we will discuss its main properties: the long-range and anisotropic character of the interactions, its peculiar excitation spectrum and its stability diagram. Then, we will introduce the main ingredients required to obtain a dipolar supersolid from a dipolar quantum gas, and we will report on its first experimental observation. Finally, we will briefly discuss the collective excitations of a trapped superfluid as possible probes of superfluidity. In particular, we will focus on the so-called *scissors* mode. This excitation is the oscillatory rotation of the gas in response to a sudden rotation of the trap, analog to the torsion oscillator experiment introduced in section 1.2.2. We will show that this oscillation can reveal the presence of non-classical rotational inertia effects in the gas, thus test its superfluid character.

2.1 Dipolar quantum gas

The occurrence of quantum condensation of bosons was firstly predicted by A. Einstein in 1925, after S. Bose derived the statistical description of photons in 1924, from then on known as Bose-Einstein distribution. As already discussed in section 1.1.2 this state appears when, at sufficiently low temperatures, a macroscopic number of bosons occupy the same quantum state, the ground state of the system. A direct consequence of BEC is the occurrence of superfluidity and NCRI. It is, in fact, the discovery of He II, the superfluid phase of ^{4}He in 1937 by Kapitza and Allen & Misener the first evidence of Bose-Einstein condensation, only pointed out by London in 1938 who associated the lambda transition of a superfluid with the BEC transition. To observe a condensate in its purer form we have to wait until 1995, when Ketterle, Wieman & Cornell, due to the development of laser

cooling and trapping of neutral atoms, firstly achieved quantum degeneracy in ultracold alkali gases. The main interaction between alkaline atoms arises from the Lennard-Jones potential, a spherical symmetric short-range interaction that treat the particles as hard spheres with a weak attractive potential.

In 2005 T. Pfau achieved the condensation of chromium, an atomic species with a high intrinsic magnetic dipole moment [36], and afterwards has been condensed also dysprosium and erbium [37, 38]. The resulting attractive dipole potential together with the repulsive contact interaction leads to new and exciting excitations. Among them is of particular interest the roton mode, a peculiar excitation similar to ^{4}He, essential to reach the supersolid phase.

In the following, we will discuss the main features of Bose-Einstein condensation with particular interest on dipolar gases. We briefly explain the nature of the interactions in play: the contact interaction and dipole-dipole interaction, besides an important feature to control their relative strength, the Feshbach resonances. Hence we will treat the Hamiltonian of the gas with a mean-field approach. We will consider the stability condition of the ground state of a homogeneous and a trapped gas, which includes geometry and excitations, besides an important consequence of a polarized gas: the elongation of the shape towards the direction of the dipoles.

2.1.1 Bose Einstein condensation

As discussed in section 1.1 Bose-Einstein condensation is a consequence of Bose statistics, and consists on the macroscopic occupation of the ground state of the system. In general, to see the effects of quantum statistics in a system, we need it to be degenerate. Namely, its thermal energy k_BT should be much lower than the characteristic quantum mechanical energy ε of the system, with k_B the Boltzmann constant. Generally speaking, ε is of the order of h/md^2 where h is the Planck constant and d is the distance between particles. So this condition implies at least that $\lambda_{dB} \sim d$ where λ_{dB} is the thermal de Broglie wavelength of a free particle with mass m

$$\lambda_{dB} = \sqrt{\frac{h^2}{mk_BT}} \tag{2.1}$$

Since $\lambda_{dB} \propto T^{-1/2}$ a we need low temperature and high densities. The criterion above is not enough alone, to see the effects of quantum statistics we also need that the particles should be able to change places fairly easily. Considering two identical bosons the not symmetrized wave function is $\psi(\mathbf{r}_1, \mathbf{r}_2)$. Indistinguishability implies that we have to properly symmetrize the wave function

$$\Psi_S(\mathbf{r}_1, \mathbf{r}_2) = \frac{1}{\sqrt{2}} \Big[\psi(\mathbf{r}_1, \mathbf{r}_2) + \psi(\mathbf{r}_2, \mathbf{r}_1)\Big] \tag{2.2}$$

We need at least some regions of phase space where $\psi(\mathbf{r}_1, \mathbf{r}_2)$ and $\psi(\mathbf{r}_2, \mathbf{r}_1)$ are *both* appreciable. That is we need some values of $\mathbf{r}_1$ and $\mathbf{r}_2$ such that before we symmetrize the wave function there is an appreciable probability of finding particle 1 at $\mathbf{r}_1$ and particle 2 at $\mathbf{r}_2$, *and* an appreciable probability of finding 1 at $\mathbf{r}_2$ and 2 at $\mathbf{r}_1$.

Extending the above criteria to a macroscopic number of particles we have Bose-Einstein condensation. As a consequence of quantum statistics it is possible to obtain the main

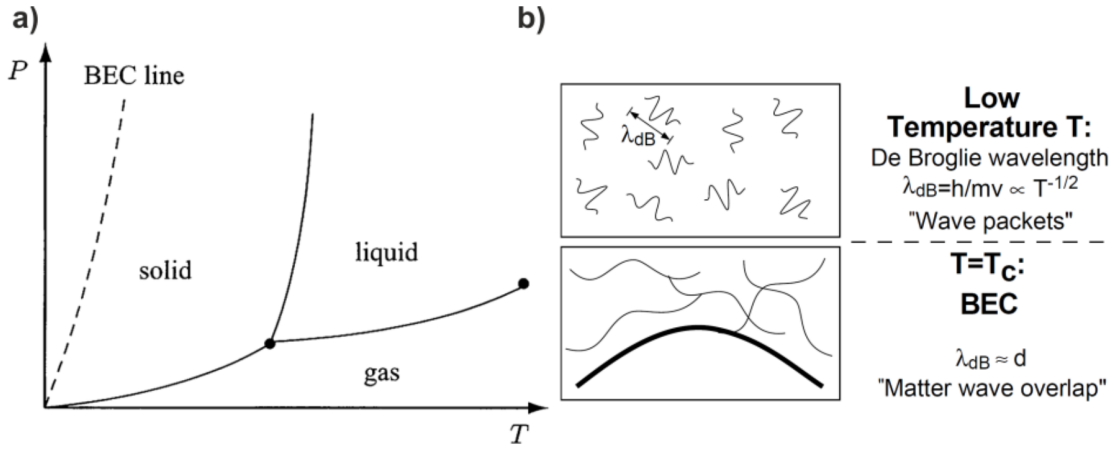

Figure 2.1: **Representation of a BEC: a)** A shematic $P - T$ phase diagram. The natural transition line for condensation is from a solid phase, pointing that gaseous BECs are metastable. **b)** Representation of a gas in a box before and after the BEC transition.

properties following qualitative arguments. We start considering an ideal gas of N Bosons equally distributed in a box of volume V, obtaining a particle density of $n = N/V$. In the thermodynamic limit the ground state of the system is the free particle state of momentum $\mathbf{p} = \hbar\mathbf{k} = 0$. In order to render the above statement more quantitative, we introduce the *momentum distribution*

$$\tilde{n}(\mathbf{k}) = \frac{1}{N}\langle\hat{\psi}^\dagger(\mathbf{k})\,\hat{\psi}(\mathbf{k})\rangle \tag{2.3}$$

where $\langle ...\rangle$ stands for thermal expectation value and $\hat{\psi}^\dagger(\mathbf{k}), \hat{\psi}(\mathbf{k})$ are Bose creation and annihilation operators of a particle with momentum $\hbar\mathbf{k}$.

In condensate the $\tilde{n}(\mathbf{k})$ operator will take the form

$$\tilde{n}(\mathbf{k}) = n_0\delta(\mathbf{k}) + \tilde{n}_{NC}(\mathbf{k}) \tag{2.4}$$

hence condensation is reached in momentum space, and particles are delocalized all over the box. In ultracold gases condensation is reached not in a box potential yet in a harmonic oscillator trap, indeed the ground state is not the zero-momentum state but the *vacuum* state, i.e., the gaussian state with energy $E = \hbar\omega/2$.

To quantify the condensation it is useful to employ the concept of phase space degeneracy, a parameter that tells how much a system is quantumly degenerate. Is defined as $D \coloneqq n\lambda_{dB}^3$. As can be seen in figure 2.1, in a thermal gas the inter-particle spacing is much larger than the de Broglie wavelength, $d \gg \lambda_{dB}$, hence $D \ll 1$ and the system follows the classical laws of thermodynamics. In a condensate the wave functions of the single particles overlap, hence $D \sim 1$ and it is not possible to treat the gas as a set of distinguishable localized particles. The atoms become indistinguishable, completely delocalized inside the box, and is necessary to use a single macroscopic wave function $\Psi = \sqrt{N}\phi_0$, where ϕ_0 is the wave function of a single particle in the ground state.

Bose-Einstein condensation occurs when $D \sim 1$. This condition can be experimentally reached by increasing the density while decreasing the temperature. Accordingly, using

equation (2.1), it is then possible to estimate the critical temperature for Bose-Einstein condensation:

$$T_c = \frac{2\pi\hbar^2 n^{2/3}}{m k_B} \tag{2.5}$$

Typical critical temperatures in ultracold gases are $T_c = 50\text{nK} \div 2\text{mK}$ with densities of $10^{14} \div 10^{15}\text{cm}^{-3}$.

Reached the critical temperature, not all the particles collapse immediately into the ground state, instead, for a confined gas, the condensate fraction follows:

$$n_0 = 1 - \left(\frac{T}{T_c}\right)^{\alpha} \tag{2.6}$$

where α depends on the geometry of the trap. For a 3D box potential $\alpha = 3/2$, while for a 3D harmonic trap $\alpha = 3$ [39]. The non-condensed fraction includes the thermal fraction n_T and the quantum depletion n_{qf}. The last one is due to quantum correlation between atoms at short distances. In contrast to liquid helium, however, the interactions in ultracold quantum gases are very weak, due to the diluteness condition. Therefore, this component can in general be neglected, and an almost pure condensate can be achieved.

2.1.2 Role of the interactions

Despite an ultracold quantum gas is very dilute - compared to a solid where densities are of the order of 10^{23} cm^{-3}, i.e., 8 orders of magnitude higher - since the kinetic energy is very low, most of its properties are governed by the interactions between particles. In the following, we present aspects of the interactions relevant to the description of a dipolar Bose-Einstein condensate, which are the isotropic, short-range contact interaction and the anisotropic long-range dipolar interaction. We also introduce an important experimental tool to control the relative strength between the two: Feshbach resonances.

Short-range interactions

When two neutral atoms approach each other, they feel an attractive electric force due to the mutual induced dipole-dipole interaction, the Van der Waals attraction, which scales as $-r^{-6}$. At very short distances the electron orbitals start to overlap, giving rise to a strong repulsion, ultimately due to Pauli's exclusion principle, which scales as r^{12}. These two contributions lead to the Lennard-Jones pseudo potential, whose characteristic interaction length r_0 satisfies the diluteness condition

$$r_0 << d \tag{2.7}$$

Under this condition, we can neglect interactions among three or more particles and consider only two-body interactions. Since below the critical temperature the coherence length is much larger than r_0 ($\lambda \sim d$), as two particles approach each other they interact before they resolve the molecular shape of the interatomic potential. This condition is expressed as $r_0/\lambda << 1$.

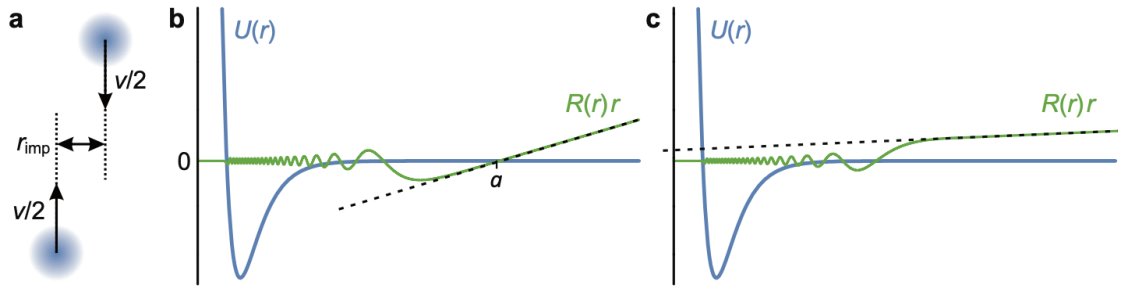

Figure 2.2: **Elastic scattering of two neutral atoms: a)** In the center of mass frame of two colliding particles the angular momentum of the interaction is determined by the relative velocity v and impact parameter r_{imp}. **b,c)** The value of the scattering length a_s is determined by the intersection of the r axis with the asymptote of the radial wave function $R(r)r$ (dashed line). Slightly different potentials can result in positive (**b**) or negative (**c**) a_s. Adapted from [40].

Following the scattering theory, in this regime interactions with angular momentum different from 0 are forbidden and only elastic s-wave scattering between particles can take place. This allows replacing the real interatomic potential, i.e., the Lennard-Jones potential, with a contact pseudo-potential, which is isotropic and can be characterized by a single parameter: the s-wave scattering length a_s [41]. This potential reads

$$V_{contact}(\mathbf{r}) = g\delta(\mathbf{r}) = \frac{4\pi\hbar^2 a_s}{m}\delta(\mathbf{r}) \tag{2.8}$$

where $\delta(\mathbf{r})$ is the Dirac delta function and g is the contact coupling strength, which depends only on a_s. A positive scattering length implies a repulsive potential, while negative a_s represents an attractive one. The value of a_s can be very different from one potential to another and depends on the molecular bound. In figure 2.2 it is shown a schematic representation of contact interactions. From now on the weakly interaction regime corresponds to the request

$$a_s << d \tag{2.9}$$

In cold atoms experiments the magnitude and even the sign of a_s can be tuned using an external magnetic field. This phenomenon is called the Feshbach resonances (FRs).

Feshbach resonances

The FRs is a physical phenomena that involves the resonance of two potentials in a scattering event. Is used in atoms physics to continuously change and control the mean-field scattering length a_s. In experiments with quantum gases this possibility is important for two reasons: control the collision properties can be essential for the attainment of the condensate and the possibility to control the mean-field interaction opens up a variety of interesting applications (ref review FRs 2010).

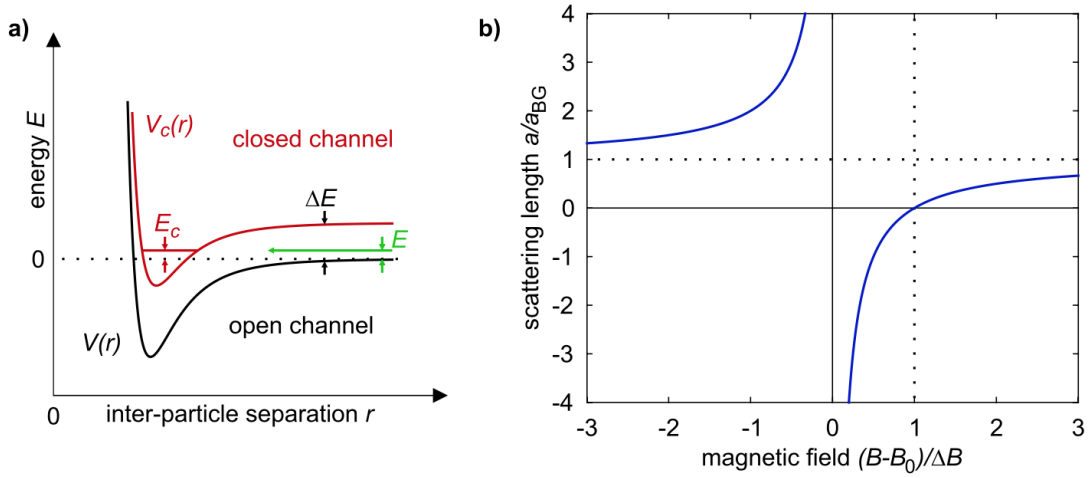

Figure 2.3: **Feshbach resonance: a)** The open and closed channel of the interaction. The resonance occurs when the interacting kinetic energy E equals the binding energy E_c. The energy difference ΔE is tunable by an external magnetic field. **b)** Scattering length *vs* magnetic field. At the resonant condition a_s diverges according to (2.10). The zero crossing is obtained for $B = \Delta B + B_0$.

First theoretical studies on FRs were done by Feshbach in 1958 in the context of nuclear physics [ref] and later on brought into the context of atomic physics [ref] by Fano in 1961. There are a variety of FRs to control a quantum system, such as magnetic, optical or orbital FRs. Here we will only focus on Magnetic FRs.

To understand the physical idea behind the FRs we have to consider two atoms interacting with energy E along two molecular potentials: $V_{bg}(R)$ or "open" channel and $V_c(R)$ or "closed" channel, showed in figure 2.3. The open channel leads to elastic scattering between two atoms, while the closed channel can change their internal states and lead to a molecular bound. As the two particles approach each other the only accessible potential is the open channel (also referred as entrance channel), due to the very low kinetic energy of the collision ($E \approx 0$). The closed channel is not accessible at first, nevertheless, once the particles get sufficiently close to each other, if the bound energy E_c is equal to the kinetic energy E, resonant coupling leads to a strong mixing between open and closed channel and a very weakly-bound and short-lived diatomic molecule is formed. This effect changes the scattering lengths of the atoms. If the two channels have different magnetic moments $\mu_{bg} - \mu_c = \delta\mu \neq 0$, they are differently affected by an external magnetic field. Using Zeeman splitting it is then possible to control the molecular potential and thus the resonance condition, leading to a tunable scattering length. In particular this quantity is modified near the resonance condition in according to

$$a_s(B) = a_{bg}\left(1 - \frac{\Delta B}{B - B_0}\right) \tag{2.10}$$

The background scattering length a_{bg} is the value associated with the open channel $V_{bg}(R)$, B_0 is the resonant magnetic field and ΔB the resonance width. For $B \simeq B_0$ a diatomic

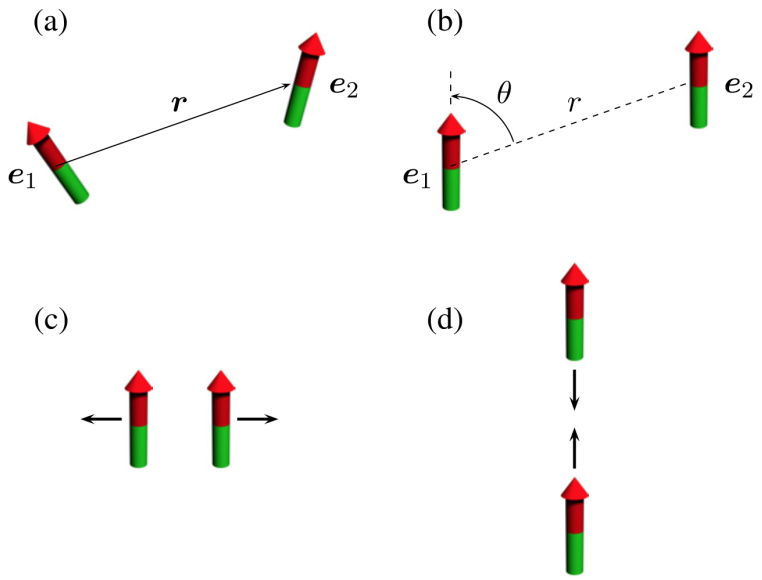

Figure 2.4: **Dipole-dipole interaction:** Two particles interacting via DDI. **a)** The non polarized case. **b)** The polarized case. **c)** The repulsive side by side configuration. **d)** The attractive head-to-tail configuration. Adapted from [42].

molecule is formed and the scattering length diverges.

Long-range interactions

In ultracold dipolar gases also the dipole-dipole interaction (DDI) must be considered [39]. This interaction arises from the natural action between two magnetic dipoles. In the presence of strong enough external magnetic field, the dipoles align along the field such that the atomic cloud gets polarized, the DDI simplifies as follows

$$V_{dd}(r,\theta) = \frac{\mu_0 \mu_m^2}{4\pi} \frac{1 - 3\cos^2\theta}{r^3} \tag{2.11}$$

here μ_0 is the vacuum permeability, μ_m^2 the intrinsic magnetic dipole moment of the atom, θ the angle along the polarization direction and r the distance between the dipoles. The essence of this interaction is its long-range nature ($\sim r^{-3}$) and anisotropic character [42]. It is easy to see the anisotropy from the angle dependence: the dipole force can be repulsive for $\theta = 0$ (side by side configuration) or attractive for $\theta = \pi/2$ (head-to-tail configuration), as illustrated in figure 2.4. It is interesting to note that the interaction vanishes for the so-called "magic angle" $\theta = \arccos(1/\sqrt{3}) \simeq 54.7°$.

A potential is defined to be short-range if the homogeneous properties of a large system, such as the energy, can be defined by local quantities only, like the density n ($\mu = \mu(n)$). If instead the number of particles N has to be explicitly specified ($\mu = \mu(N, n)$), due to strong (diverging) dependence on N, the potential is long-range [42].

In order to see the long-range nature of the dipolar interaction we have to see its

behavior at large distances, that is the following integral must converge for large R:

$$\mu = \int_b^R V_{dd}\, r^{D-1} \mathrm{d}r \propto [r^{D-3}]_b^R \tag{2.12}$$

where D is the dimensionality of the system and b some short (but finite) distance cutoff. Following this definition, in D dimensions the potential is short-range if it decays at large distance faster than r^{-D}. This is true only if $D < 3$. Hence, the dipole-dipole interaction is long-range in three dimensions, and short-range in one or two dimensions.

Due to the long-range character of DDI in principle all partial waves with angular momenta $l > 0$ contribute to the scattering process, moreover the anisotropy couples these partial waves with different angular momenta. Therefore, it's not possible to describe the scattering process with a short-range, isotropic contact interaction as done for the molecular potential. Nevertheless, for low enough scattering energies, a first-order Born approximation is still valid and the dipolar scattering can be approximated to be universal and scatters only into s-wave channel.

For further discussions, it is convenient to quantify the strength of the DDI. To do so, it is useful to define the dipolar scattering length a_{dd} and dipolar coupling strength g_{dd}, as previously done with the contact interaction a_s and g

$$a_{dd} = \frac{m\mu_0\mu_m^2}{12\pi\hbar^2} \qquad \text{and} \qquad g_{dd} = \frac{4\pi\hbar^2 a_{dd}}{m} \tag{2.13}$$

And the ratio between this two parameters is the dimensionless relative interaction strength

$$\varepsilon_{dd} = \frac{a_{dd}}{a_s} \tag{2.14}$$

The dipolar scattering length a_{dd} is defined such that the mean-field energy of a three-dimensional homogeneous dipolar condensate becomes negative for $\varepsilon_{dd} > 1$, that is the system becomes unstable and collapses. Nevertheless, in real experiments the condensate is confined, and, as we will discuss in section 2.1.4, the stabilization condition depends strongly on the geometry of the cloud, as suggests the anisotropic character of the DDI. Therefore with the proper trap configuration, ε_{dd} can get bigger values, reaching the strong dipolar regime, beyond $\varepsilon_{dd} = 1$. In fact, the supersolid phase occurs in this regime. Since the background value of ε_{dd} is an intrinsic property of the atomic species considered, the method of Feshbach resonances is essential in order to freely changed it, by tuning a_s.

Combining the short-range interaction and the DDI it is possible to write the resulting interaction potential of a dipolar condensate:

$$V_{int}(r,\theta) = g\delta(r) + \frac{3g_{dd}}{4\pi}\frac{1-3\cos^2\theta}{r^3} \tag{2.15}$$

2.1.3 Mean-field description

The first approach to a system of many interacting particles is the so-called mean-field approximation [39]. This implies that each particle feels an effective potential that is the average of all other particle interactions. The many-body Hamiltonian of a condensate of

interacting bosons confined in an external potential V_{ext}, written in second quantization reads

$$\begin{aligned}\hat{\mathcal{H}} = \int \mathrm{d}^3 r\, \hat{\Psi}^\dagger(r)\bigg(-\frac{\hbar^2}{2m}\nabla^2 + V_{ext}(\mathbf{r})\bigg)\hat{\Psi}(\mathbf{r}) + \\ +\frac{1}{2}\int \mathrm{d}^3 r\, \mathrm{d}^3 r'\, \hat{\Psi}^\dagger(r)\hat{\Psi}^\dagger(\mathbf{r}')V_{int}(\mathbf{r}-\mathbf{r}')\hat{\Psi}(\mathbf{r})\hat{\Psi}(\mathbf{r}')\end{aligned} \tag{2.16}$$

where $\hat{\Psi}^\dagger(\mathbf{r})$ and $\hat{\Psi}(\mathbf{r})$ are the creation and annihilation bosonic operators. These operators fulfill the normalization $N = \int \mathrm{d}^3 r\, \hat{\Psi}^\dagger(\mathbf{r})\hat{\Psi}(\mathbf{r})$. In the Heisenberg representation the operators are time dependent

$$\begin{aligned}i\hbar\,\partial_t\hat{\Psi}(\mathbf{r},t) = \Big[\hat{\Psi}(\mathbf{r},t), \hat{\mathcal{H}}\Big] = \\ = \bigg(-\frac{\hbar^2}{2m}\nabla^2 + V_{ext}(\mathbf{r}) + \int \mathrm{d}^3 r'\, \hat{\Psi}^\dagger(\mathbf{r}',t)V_{int}(\mathbf{r}-\mathbf{r}')\hat{\Psi}(\mathbf{r}',t)\bigg)\hat{\Psi}(\mathbf{r},t)\end{aligned} \tag{2.17}$$

Since numerical simulations of this Hamiltonian are very complicated, sometimes impossible, it is useful to introduce a classical field approximation, first introduced by Bogoliubov in order to study the ground state dispersion relation of a condensate. The approximation states that it is possible to write the bosonic operator in terms of a classical function Ψ with a small perturbation in second quantization $\delta\hat{\Psi}$, which corresponds to quantum fluctuations

$$\hat{\Psi}(\mathbf{r},t) = \Psi(\mathbf{r},t) + \delta\hat{\Psi}(\mathbf{r},t) \tag{2.18}$$

The function Ψ is the superfluid order parameter introduced in section 1.1.2, is the macroscopic wave function of the condensate and is equal to $\sqrt{N}\varphi_0$, where φ_0 is the single-particle wavefunction. This approximation assumes a large occupation of the ground state of the system, thus does not prove the existence of the condensate, and considers the quantum depletion negligible [39]. This assumption is doable in ultracold quantum gases where quantum fluctuations are weak. Nevertheless, as we will see in section 2.2.2, the contribution of these fluctuations is crucial in order to stabilize the supersolid.

Using the ansatz of a slowly varying wave function $\Psi(\mathbf{r},t) = \psi(\mathbf{r})exp(-i\mu t/\hbar)$, where μ is the chemical potential, we can separate-off the time dependence and end-up with the stationary *dipolar Gross-Pitaevskii Equation* (dGPE)

$$\mu\psi(\mathbf{r}) = \bigg(-\frac{\hbar^2}{2m}\nabla^2 + V_{ext}(\mathbf{r}) + \Phi_{contact}(\mathbf{r}) + \Phi_{dd}(\mathbf{r})\bigg)\psi(\mathbf{r}) \tag{2.19}$$

where we used the mean-field potentials of the contact interaction $\Phi_{contact}(\mathbf{r}) = gn(\mathbf{r})$ and dipolar interaction $\Phi_{dd}(\mathbf{r}) = \int \mathrm{d}^3 r\, V_{dd}(\mathbf{r}-\mathbf{r}')n(\mathbf{r}')$. Here $n(\mathbf{r},t) = |\Psi(\mathbf{r},t)|^2$ is the density.

Now, in order to discuss the ground state properties and excitations of the condensate, we must derive the energy functional

$$E(n,\mathbf{r}) = \int d^3 r \left(\frac{\hbar^2}{2m}\nabla^2 + V_{ext}(\mathbf{r}) + \frac{\Phi_{contact}(\mathbf{r}) + \Phi_{dd}(\mathbf{r})}{2}\right)n(\mathbf{r}) \tag{2.20}$$

The lowest energy configuration can be obtained by imposing the usual variational ansatz $\delta(E-\mu N) = 0$, with the chemical potential found above (2.19) [39].

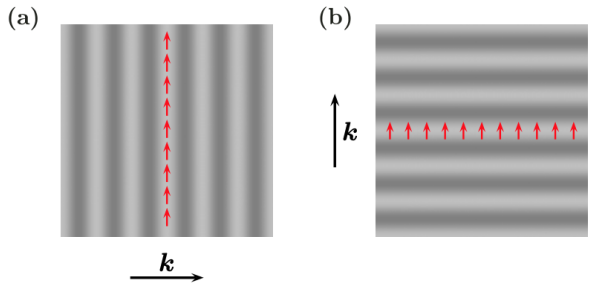

Figure 2.5: **Phonons excitations: a)** A phonon excitation in a homogeneous dipolar BEC with $\alpha = \pi/2$ creates vertical planes with a head to tail configuration, which is instable for ε_{dd} bigger than 1. **b)** When the dipoles are parallel to the wave vector ($\alpha = 0$) the configuration is side by side and more stable. Taken from [42]

2.1.4 Instabilities

Because of the partially attractive nature of the dipolar condensate, the stability condition of the ground state and the role of the excitations is a problem that needs to be addressed. Firstly we will treat the homogeneous gas. Hence we will treat a trapped condensate and the role of the geometry and the strength interaction ε_{dd} in the stability. Finally, we will discuss a consequence of the polarization of the gas: the magnetostriction.

Homogeneous gas

We consider here the excitations of a 3D homogeneous dipolar condensate, that is with no external potential. For a condensate with a given equilibrium density n and interaction ε_{dd}, the corresponding Bogoliubov dispersion relation is determined by the Fourier transform $\tilde{V}_{int}(\mathbf{q})$ of the two-body interaction potential (2.15)

$$E(q) = \hbar\omega(q) = \sqrt{\left(\frac{\hbar^2 q^2}{2m}\right)^2 + \frac{\hbar^2 q^2}{2m} gn\Big[1 + \varepsilon_{dd}(3\cos^2\alpha - 1)\Big]} \tag{2.21}$$

where α is the angle between the direction of the dipoles and the excitation q. Lets now consider phonon solutions ($q \to 0$). The speed of propagation of the excitation reads

$$c_s = \lim_{q\to 0} \frac{E(q)}{q} = \sqrt{\frac{\hbar g n}{2m}} \sqrt{1 + \varepsilon_{dd}(3\cos^2\alpha - 1)} \tag{2.22}$$

Fixed the value of ε_{dd}, the anisotropy of the DDI brings to different sound speeds for different values of α. A large c_s value implies a more stable system against compression, while a small c_s value corresponds to a softening of the mode. The velocity is maximum for $\alpha = 0$ and minimum for $\alpha = \pi/2$. In particular, in the latter case, a phononic excitation becomes imaginary for $\varepsilon_{dd} \geq 1$ and the system becomes unstable. Furthermore, a purely dipolar ($g = 0$) 3D homogeneous condensate is unstable, as the cloud tends to acquire a head-to-tail configuration while c_s is zero (equation 2.22), thus as the number of dipoles increases the system goes into a macroscopic collapse.

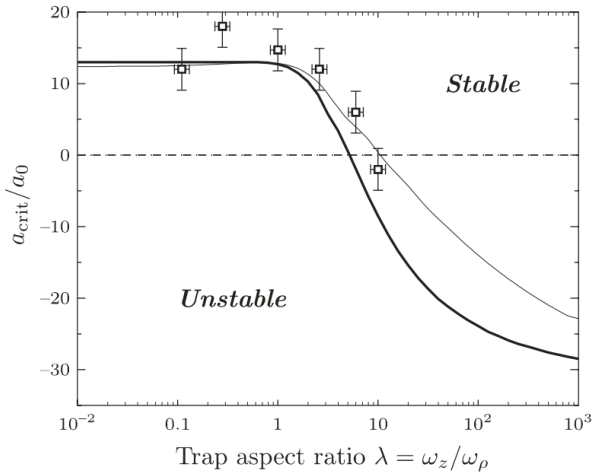

Figure 2.6: **Stability diagram:** Here is shown the stability diagram of a cylindrical dipolar condensate in the plane (λ, a_s). The dots correspond to experimental data, the thick lane is obtained using a gaussian ansatz of the wave function and the thin line to numerically solving the equation (2.17). Very prolate traps ($\lambda \ll 1$) can stabilize for smaller values of a_s. As $a_s \propto \varepsilon_{dd}^{-1}$ it is possible to reach the strong dipolar regime $\varepsilon_{dd} > 1$ necessary to achieve a dipolar supersolid. Taken from [42]

Trapped gas

The ground state configuration of a non-dipolar condensate with attractive interactions ($a < 0$) it is stable only for low enough atoms number in a trapped configuration. In particular, for $N|a|/a_{\rm ho} \leq 0.58$, where N is the atoms number and $a_{\rm ho} = \sqrt{\hbar/m\omega}$ is the harmonic oscillator length.

In a dipolar condensate, the situation is slightly different. The attractive nature of the dipoles can be hidden by strongly confining the atoms in the dipole direction. Let us consider a cylindrical trap with the dipoles aligned in the z-axis with a certain confinement parameter $\lambda = \omega_z/\omega_\rho$, where ω_ρ is the radial frequency. For an oblate trap ($\lambda > 1$) the DDI is mostly repulsive (side by side configuration) and it is easier to stabilize the system. Instead for a prolate trap ($\lambda < 1$), the DDI is most attractive (head-to-tail configuration), therefore it is more difficult to achieve stabilization. It is now intuitive that the stability condition depends on the balance between the trap geometry and the interaction strength. In particular, given a value of λ exists a critical value of a_s (hence ε_{dd}) for which the condensate becomes unstable [42]. Following equation (2.14) the lower can be a_s, the bigger ε_{dd}. A typical stability diagram is shown in figure (2.6).

An important effect that arises in a trapped dipolar condensate in the presence of an external magnetic field is the elongation of the cloud in the direction along the orientation of the dipoles. In a condensate in the Thomas-Fermi distribution, the atoms generate a mean-field potential with the shape of a saddle, with the minima along the direction of the dipoles. Therefore the system minimizes the energy by assuming a head-to-tail configuration, changing the shape of the cloud and its volume. This effect, called *magnetostriction*,

strongly depends on the value of ε_{dd} [42].

A good comprehension of the stabilization parameters is important to experimentally achieve the supersolid in a prolate trap. Moreover, the magnetostriction effect on the cloud shape geometry is crucial when studying the in trap modes. As we will see in section (2.3.3) the resulting frequency of certain collective excitations of a dBEC and a SS strongly depends on their configuration ground state. Another important excitation that could lead to an instability in a trapped dipolar condensate is the so-called *roton* mode. But since its important role in the creation of the supersolid is treated more carefully in the next chapter.

2.2 Dipolar supersolid

In this chapter, we will discuss the two main ingredients that give rise, under proper conditions, to a novel regime with supersolid properties in a dipolar quantum gas. First, we will introduce the roton mode, an excitation of a trapped dipolar condensate that leads to a finite momentum instability, able to imprint a density modulation with finite wavelength to the dipolar quantum gas. We will then discuss the stabilizing effects of quantum fluctuations on a collapsing dipolar condensate. We will show that, for a narrow range of scattering length and trap confinement, these two ingredients give rise to a coherent stripe modulation, in other words, a supersolid. Finally, we will introduce some of the main features of a trapped dipolar supersolid, such as its excitation spectrum and its main collective excitations.

2.2.1 Roton instability

As discussed in section 2.1.4, the excitations of a condensate can lead to the collapse of a homogeneous gas when $\varepsilon_{dd} \geq 1$, but in an oblate trap a condensate can stabilize even in the strong dipolar regime. Here we introduce a different kind of instability occurring in a dipolar BEC, when trapped in a quasi-2D geometry, or in an oblate trap: the roton instability.

The concept of roton has been introduced by Lev Landau in 1960 when he was trying to give a phenomenological description of the dispersion relation of superfluid 4He. He introduced the concept of two quasi-particles: phonons, sound waves with linear dispersion at low momentum, and rotons, parabolic collective excitations at higher momentum with a characteristic local energy minimum Δ. The roton minimum is a consequence of the competition between attractive and repulsive forces. In general, it originates from the fact that at intermediate momenta one has a local structure produced by the tendency of atoms to stay apart [8].

In order to elucidate the origin of the roton minimum in a quasi-2D dipolar gas, let us assume an infinite "pancake" trap, i.e. a cylindrically symmetric with $L_\rho \to \infty$ and a low confinement length L_z. Here z is the directions of the dipoles, while ρ is the radial coordinate in the plane perpendicular to z. A typical excitation spectrum of this system is shown in figure 2.7. For momenta $q \ll 2\pi/L_z$ the existence of a confinement in the z-direction prevent excitations along the z-axis. Therefore the excitations have a 2D (in-plane) character. Since the dipoles are perpendicular to the plane of the trap, they repel

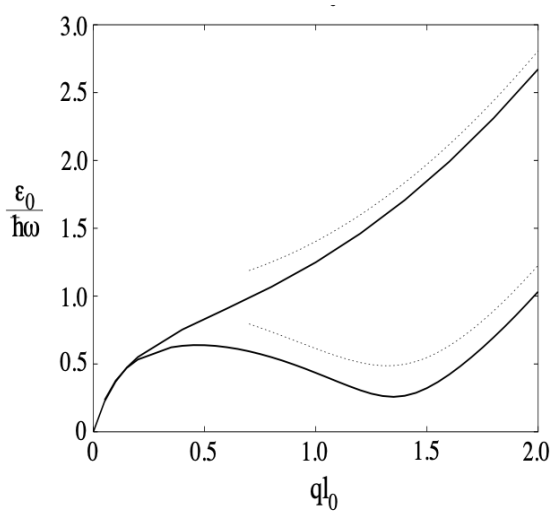

Figure 2.7: **Roton dispersion relation:** Typical dispersion law ϵ for different values of the parameter ε_{dd} and $\mu/\hbar\omega$. The solid curves show the numerical results, and the dotted curves the result of equation 2.19. Taken from [8].

each other and the in-plane excitations are phonons. For $q \gg 2\pi/L_z$, excitations can acquire a 3D character and the inter-particle repulsion is reduced, since dipoles can interact also in a head-to-tail configuration. This decreases the excitation energy under an increase of q. The spectrum reaches a minimum at $E(q) = \Delta$ and then starts to grow with a parabolic curve, as the excitations acquire a free particle character [8].

In dipolar condensates, the position and amplitude of the roton are tunable. In particular the roton momentum q_{rot} depends on the vertical confinement L_z; thus it can be tuned by changing the trap confinement in the z direction. The roton gap delta depends instead on the dipolar strength ε_{dd}; it can be tuned by changing the density of the sample or, more easily, by tuning the contact scattering length a_s. When the roton energy falls to zero, the frequency becomes imaginary. The subsequent exponentially growth of the $q = q_{rot}$ state modulates the condensate wave function with periodicity $d = 1/q_{rot}$, a rotonic instability and a rotonic instability develops.

The roton instability and the rotonic spectrum of a dipolar BEC phase were observed in 2018, by the Innsbruck group with an Erbium dipolar gas [29, 30]. However no studies on the time evolution of a "rotonized" dipolar gas were performed in these work, in order to test its potential supersolidity.

2.2.2 Quantum fluctuations

In 2016, the Stuttgart group explored the fate of an unstable dipolar condensate trapped in an oblate trap [43]. As discussed in section 2.2.1, in this configuration the excitation spectrum of the dipolar gas shows a roton minimum, and for large enough ε_{dd} the system should undergo a roton instability. As shown in figure 2.8, the experiment report the formation of a peculiar droplet crystal, presumably triggered by the roton instability. At the instability the condensate, instead of collapse, reassembles itself in several self-bound droplets, which

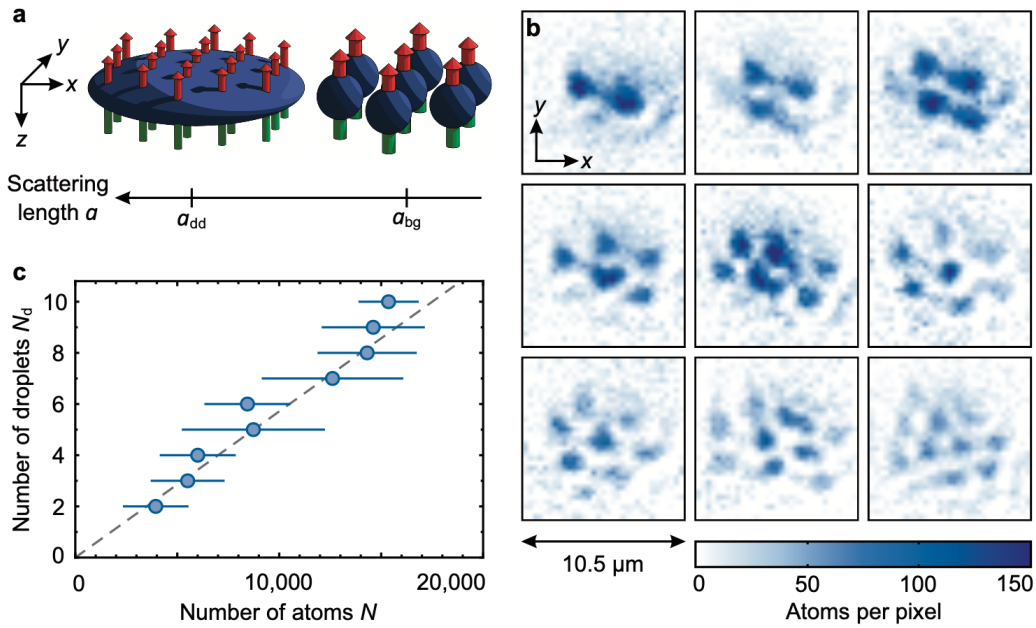

Figure 2.8: **Droplet lattice: a)** A quantum gas of dysprosium atoms confined in a pancake geometry go through a droplet crystal by lowering a_s. **b)** The droplets arrange themselves in an auto-induced triangular lattice with a number of droplets from 2 to 10. **c)** The number of droplets is proportional to the number of atoms, with $\sim$ 2000 atoms per droplet. Taken from [43].

repel each others, forming an ordered lattice. Even though every single droplet is superfluid, no evidence of superfluidity or mutual phase coherence between droplets was found. However, these droplets are particularly interesting. They are indeed a stable self-bound quantum state, occurring in a system that should collapse at the mean field level.

Subsequent experimental and theoretical works [43, 44, 45, 46], have shown that the stabilization mechanism of quantum droplets stems from quantum fluctuations, which are almost negligible in standard BECs, but relevant in attractive dipolar BECs. The same mechanisms was predicted to stabilize also a mixture of (non dipolar) Bose-Einstein condensates in 2015 [34], as observed two years ago [32, 33]

Quantum fluctuations are the energy fluctuations of vacuum arising from the zero-point motion of the collective modes of the condensate, due to Heisenberg's uncertainty principle. 1957 Lee, Huang & Yang quantified this correction term starting from the Bogoliubov transformation of a (single component) weakly interacting (non dipolar) BEC [47]:

$$\hat{\mathcal{H}} = E_0 + \sum_{\boldsymbol{q}} \varepsilon_{\boldsymbol{q}} \hat{b}^\dagger_{\boldsymbol{q}} \hat{b}_{\boldsymbol{q}} \tag{2.23}$$

Here E_0 is the energy of the ground state, i.e. the vacuum, and $\hat{b}^\dagger_{\boldsymbol{q}}$ and $\hat{b}_{\boldsymbol{q}}$ are the Bogoliubov quasi-particle creation and annihilation operators.

The density population that is depleted from the vacuum Δn results in a shift of the ground state energy E_0, and thus in a modification of the chemical potential μ. The

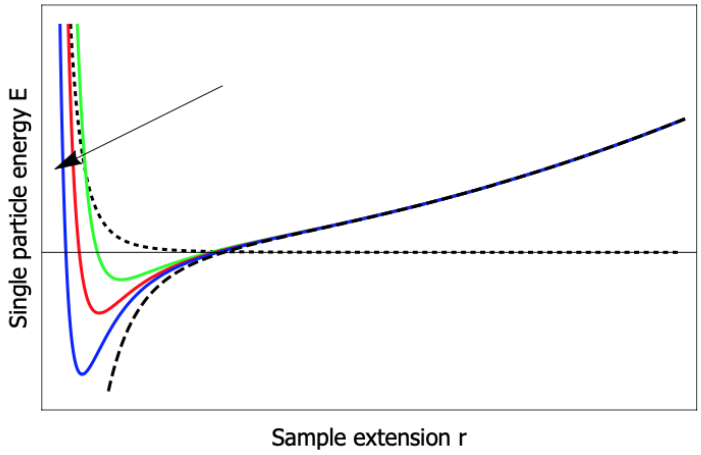

Figure 2.9: **Beyond mean field stabilization:** The mean field energy is reported with the dashed line, while the corresponding LHY correction for the same a_s with the dotted line. In color is presented the sum of the two contributions for different a_s. The direction of the arrow indicates the increase on a_s [ref Famá].

calculation for a dipolar gas was first performed by by Lima and Pelster [48], and the correction for $\Delta\mu$ reads:

$$\Delta\mu(\mathbf{r}) = g_{\rm qf}|\psi(\mathbf{r})|^3 \qquad \text{with} \qquad g_{\rm qf} = \frac{32ga_s^{3/2}}{3\sqrt{\pi}}\left(1+\frac{3}{2}\varepsilon_{dd}^2\right) \tag{2.24}$$

Note that the LHY term is a repulsive term (it is always positive) and scales with the density as $n^{3/2}$.

In order to account for this beyond mean-field correction, we write *extended Gross-Pitaevskii equation* (eGPE) for dipolar interactions:

$$\mu\psi(\mathbf{r}) = \left(-\frac{\hbar^2}{2m}\nabla^2 + V_{ext}(\mathbf{r}) + gn + \Phi_{dd}(\mathbf{r}) + g_{\rm qf}\,n^{3/2}\right)\psi(\mathbf{r}) \tag{2.25}$$

This equation is a first order correction of equation 2.19 accounting for quantum pressure. In general this correction is negligible ($g_{\rm qf}\,n^{3/2} \ll gn+\Phi_{dd}(\mathbf{r})$) and the energy of the system follows the dashed line of figure 2.9. However when the mean field dipolar interaction is opposed to the mean field contact interaction, leading to a negative value of chemical potential, the LHY contribution stabilizes the system arising the energy (dotted line) and preventing the collapse. Therefore the system stabilizes forming a droplet with an equilibrium density given by the minimum of the sum of the mean-field and beyond mean-field energy contributions.

2.2.3 Phenomenology of a dipolar supersolid

The main ingredients to obtain a supersolid from a dipolar quantum gas are: 1) the existence of a roton minimum in the excitation spectrum, which gives rise to a density

modulation when the roton energy becomes zero; 2) the stabilizing effect of quantum fluctuations, which prevents the system from collapsing once crossed the roton instability, stabilizing an array of self-bound droplets. These droplets, are however typically strongly bound and not enough mutually coherent as required in a supersolid [35].

The occurrence of a supersolid phase in a dipolar quantum gas was observed for the first time in 2019, in the experimental apparatus where I carried out my master thesis [7]. My colleagues could spot a small range of parameters where a coherent, density-modulated state forms after crossing the rotonic instability, presenting the ingredients required for a one-dimensional supersolid. The main idea was to find an interaction regime of extremely weakly bound droplets, in order to increase their capability to overlap and establish mutual coherence. The main results are presented in figure 2.11. The momentum distribution of the dipolar quantum gas is shown for different values of contact length scattering and for different evolution times.

The upper panel ($a_s = 108\,a_0$, $\varepsilon_{dd} = 1.2$), illustrates the system in the "standard" BEC regime, which remains unvaried during time. As the scattering length is lowered to $a_s = 94\,a_0$ ($\varepsilon_{dd} = 1.38$, middle panel), a stripe modulation spontaneously emerges: the momentum distribution shows small side peaks along the weak trap axis, with characteristic momentum $k_{rot} = 1.2(2)\mu\text{m}^{-1}$, close to the roton momentum predicted for an unconfined system at the instability, $k_{rot} \approx 1.6\mu\text{m}^{-1}$. These side peaks in the momentum distribution reveals that the system has broken translational invariance in the real space: a crystal has formed. Remarkably, the shape of $\tilde{n}(k_x, k_y)$ is reproducible from shot to shot for several tens of milliseconds, signalling that the droplets composing the crystal are phase coherent. Eventually, for long times (more than 100ms), an unmodulated BEC is recovered, due to atom losses. For smaller contact scattering length values of $a_s = 88\,a_0$ ($\varepsilon_{dd} = 1.47$, lower panel) instead, the shape of the momentum distribution is irregular and unreproducible from shot to shot, suggesting that phase coherence between different droplets is lost. This observation, supported by numerical calculations, has been interpreted as the first evidence of a metastable supersolid state in a dipolar quantum gas.

Rapidly, these findings have been replicated by other experiments [9, 10], confirming the phenomenon; supersolidity appears for different atomic species (it has been tested for Dy and Er) and for different parameter values. Even though the supersolid state decays in time due to three-body losses (I will discuss about it with more details in section 3.3.3), its lifetime is sufficiently long (100-200 ms) to allow further experimental investigation of the properties of supersolids.

The first property that has been investigated in a dipolar supersolid is its peculiar excitation spectrum [11, 12, 13]. A crucial feature of a supersolid is the occurrence of two gapless excitations, reflecting the Goldstone modes associated with the spontaneous breaking of two continuous symmetries, introduced in section 1.1: 1) the breaking of phase invariance, corresponding to the locking of the phase of the atomic wave functions at the origin of superfluid phenomena; 2) the breaking of translational invariance due to the lattice structure of the system. Such modes have been the object of intense theoretical investigations, since the first theoretical models of supersolidity.

In trapped dipolar supersolid the excitation spectrum was studied by monitoring the fate of the lowest compressional mode of the system - the axial breathing mode - when crossing the superfluid-to-supersolid transition. Low-frequency compressional modes emerge naturally from the hydrodynamic equations of superfluids [41]. The hydrodynamic equations

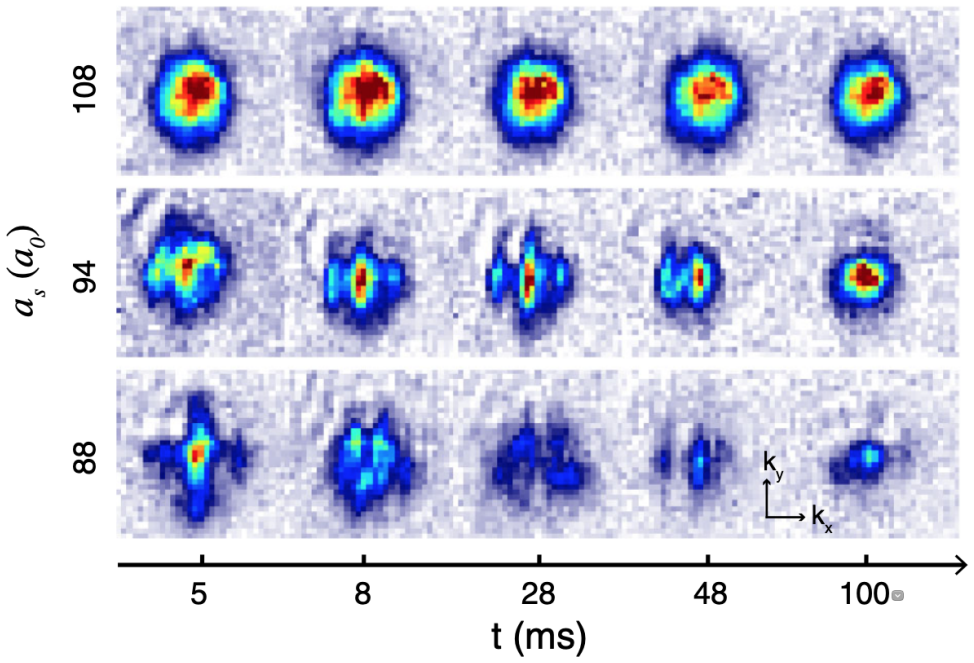

Figure 2.10: **From a BEC to a droplet crystal:** Typical momentum distribution $\tilde{n}(k_x, k_y)$ after time-of-flight for different values of s-wave length scattering. Above is a typical BEC, lowering a_s in the centre a SS phase, and below Incoherent Droplets. Taken from [7].

are the direct consequence of the locking of the phase of the order parameter and are hence peculiar to superfluid systems at low temperature. In a recent combined theoretical and experimental investigation, the CNR-INO/LENS group has discovered that, when the system crosses the superfluid-to-supersolid transition by tuning the interactions, the axial breathing mode bifurcates into two distinct excitations, similar to the bifurcation of the gapless Goldstone excitations expected for a homogeneous supersolid.

This result is plotted in figure 2.11: both the calculated (dotted lines) and the measured (points) energy of the axial breathing mode is shown as a function of the interaction ε_{dd}. For $\varepsilon_{dd} > 1.38$ the system enters in the supersolid phase (see the blue dotted line). As discussed previously, transition to the supersolid regime is marked experimentally by the appearance of an extra peaks in the momentum distribution. While in the superfluid regime the system oscillates with a single frequency, the spectrum bifurcates into two different modes at the supersolid transition, one associated with the superfluid character (blue line) and one to the solid character (red line). The SF mode is associated with the coherent transfer of particles between droplets and softness until it completely disappears in the droplet crystal phase. This softening can be justified as an increase of the effective mass of the atoms moving through the droplets, lowering the superfluid fraction of the supersolid. The higher mode is related to the lattice deformation, in particular it is the compressional oscillation of the droplets (crystal phonon) and survives in the droplet crystal phase. Since both SF

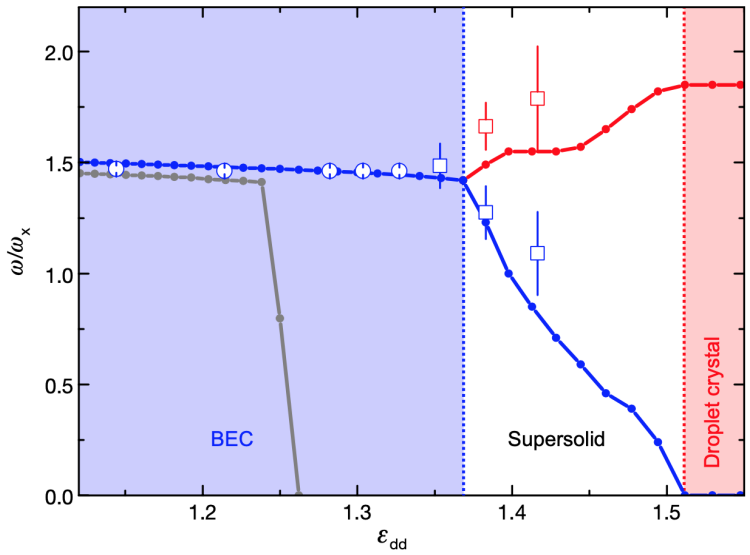

Figure 2.11: **Axial breathing mode:** The frequency plotted versus the strength interaction ε_{dd}. The different regions show the different phases, from BEC, supersolid to droplet crystal (DC) by increasing ε_{dd}. Dotted lines are the numerically predicted frequencies. Points with error bars are the experimental data. The theoretical frequency without considering the LHY term (grey line) becomes imaginary before entering the SF phase. The single frequency of a SF (blue line) that arises from the gauge broken symmetry U(1) splits into two modes when the system enters in the SS phase. The SF mode disappears in the DC phase. The crystal mode (red line) survives in the DC phase. Taken from [11].

and crystal modes oscillates with a characteristic frequency, the supersolid oscillates with the beating of both frequencies. The spontaneous bifurcation of the axial breathing mode demonstrates that the dipolar supersolid is compressible as the hypothesized supersolid helium (section 1.1), differently from the supersolids with light-mediated interactions.

2.3 Collective oscillations as probe to superfluidity

Despite supersolidity has been observed, still there no experiments have directly tested its superfluid character, on the spirit of the original torsion oscillators experiments looking for NCRI in solid Helium. One way to probe superfluidity in BECs is to study their time dependent behaviour. In particular, how the system responds to an elastic stress depends on the hydrodynamic properties of the system.

This chapter is devoted to discussing the dynamical behaviour of a condensate, with particular interest in its collective modes when trapped. I will focus on a specific collective mode, the scissors mode, that is the oscillatory rotation of an elliptical superfluid in response to a sudden rotation about a small angle. I will show that this mode, analog to the torsion oscillator, permits to directly observe in a superfluid the presence of NCRI by measuring the fraction of inertia I/I_c, thus the superfluid fraction. Precisely, I will

start discussing non dipolar condensates, to then extend the discussion of dipolar condensates and supersolids, deriving the equations that relate the scissors frequency with the superfluid fraction.

For the sake of completeness, a full theoretical picture of collective oscillations for a dipolar supersolid has not been made so far. Precise simulations of the *scissors* mode starting from the eGPE and sum rules approach are carried by the Trento's BEC group [49]. An extensive treatment of collective excitations of a dipolar BEC in the Thomas-Fermi regime can be found in [50].

2.3.1 Elementary excitations of a superfluid

The starting point to describe the dynamics of a BEC are the hydrodynamic equations. In the following we will consider only non dipolar condensates. If we multiply the time-dependent *Gross-Pitaevskii equation* (2.25) by $\Psi^*(\mathbf{r}, t)$ and subtracts the complex conjugate of the resulting equation one gets the continuity equation, which ensures the conservation of the particles number

$$\frac{\partial n}{\partial t} + \boldsymbol{\nabla} \cdot (n\mathbf{v}_s) = 0 \tag{2.26}$$

where $\mathbf{v}_s$ is the superfluid velocity of the condensate defined in (1.5). As we have seen the velocity is proportional to the of gradient of the phase φ, and thus irrotational unless when vortices are excited. The equation of motion of the velocity is the Euler equation of the *Gross-Pitaevskii equation* and reads

$$m\frac{\partial \mathbf{v}}{\partial t} = -\boldsymbol{\nabla}\left(\mu + \frac{1}{2}m\mathbf{v}^2\right) \tag{2.27}$$

where the chemical potential is $\mu = V_{ext}(r) + gn$. This equation together with (2.26) constitute the hydrodynamic equations of a superfluid.

Since the only degrees of freedom are those of the condensate order parameter, which has a magnitude and a phase, the motion of the condensate may be specified only in terms of a local density (magnitude) and a local velocity (phase). Hence the elementary excitations of the condensate may be investigated by considering small perturbations of these two quantities from the ground state density. Accordingly we write the density as $n = n_{eq} + \delta n$, where n_{eq} is the equilibrium density and δn a small deviation. Inserting this quantity together with a small velocity $\mathbf{v}$ into the hydrodynamic equations (2.26) and (2.27) one gets

$$\frac{\partial \delta n}{\partial t} = -\boldsymbol{\nabla} \cdot (n_{eq}\mathbf{v}) \qquad \text{and} \qquad m\frac{\partial \mathbf{v}}{\partial t} = -\boldsymbol{\nabla}\delta\mu \tag{2.28}$$

where $\delta\mu = g\delta n$ is the effect of the density perturbation on the chemical potential. In order for this equation to be valid, the spatial variation of the density must be smooth not only in the ground state but also during the oscillation. This is equivalent to require the wavelength of the excitation to be much larger than the healing length. Taking the time derivative of the first equation of (2.28) and eliminating the velocity by inserting the second

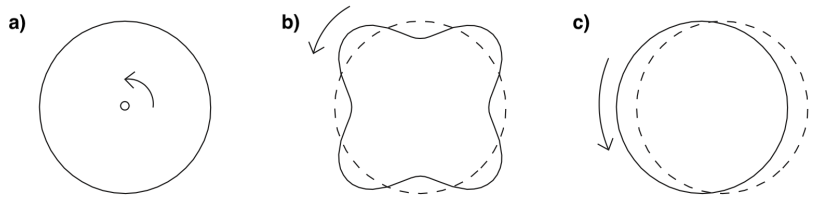

Figure 2.12: **Collective excitations with angular momentum:** Different ways to add angular momentum to a trapped condensate: **a)** A vortex: a density hole in which all atoms have the same momentum; **b)** Quadrupole oscillation: a wave density perturbation propagating on the surface or **c)** Dipole oscillation: a center of mass oscillation. Taken from [41].

equation of (2.28) we get the equation of motion for collective oscillations of Bose-Einstein condensates

$$m\frac{\partial^2 \delta n}{\partial t^2} = g\boldsymbol{\nabla}\cdot(n_{eq}\boldsymbol{\nabla}\delta n) \tag{2.29}$$

This equation describes the elementary excitations of a BEC with any equilibrium density. It is remarkable to stress that here the density is the total density and not only the superfluid density n_s. If the gas is not trapped we get the usual Bogoliubov spectrum: phonons at low momentum and free particles at higher momentum. In the following we will consider only excitations of a condensate trapped in a harmonic 3D potential $V = V_{ext}(r)$.

By considering wave-like oscillations $\delta n \propto e^{-i\omega t}$ of a condensate with a Thomas-Fermi equilibrium density $n_{eq} = (\mu - V)/g$ the equation (2.29) reduces to

$$m\omega^2\delta n = \boldsymbol{\nabla}V\cdot\boldsymbol{\nabla}\delta n - (\mu - V)\nabla^2\delta n \tag{2.30}$$

Solutions to this equation strictly depend on the symmetry of the external potential. Are characterized by the quantum numbers n_r, l and m, which states for the number of radial nodes, total angular momentum, and projection along its rotation axis. Solutions with $n_r \neq 0$ are called *compressional* modes, which lowest solution is the monopole oscillation with $n_r = 1$, $l = 0$. On the contrary, solutions with $n_r = 0$ are called *surface* modes, like the dipole oscillation ($l = 1$) or quadrupole oscillation ($l = 2$), which carry angular momentum, as illustrated in figure (2.12) [41]. The *axial breathing* mode is an oscillation that couples the monopole mode with the quadrupole mode, thus shows compression and surface shape oscillation. The oscillation with $l = 2$ and $m = 1$ correspond to a peculiar *surface* mode called *scissors* mode that we will discuss in the next chapter.

2.3.2 The scissors mode

Despite the occurrence of most of the collective oscillations are important consequences of superfluidity, in general, the emergence of this phenomenon can not be considered as direct proof of the superfluid nature of condensates. S. Stringari proposed in 1999 a conceptually easy way to observe the occurrence of non-classical rotation inertia phenomena in ordinary BECs through the measure of the *scissors* mode [14].

The scissors mode occurs in a BEC trapped in an harmonic trap with elliptical geometry, see figure 2.13.a. It is the oscillatory rotation of the cloud in response to a sudden rotation

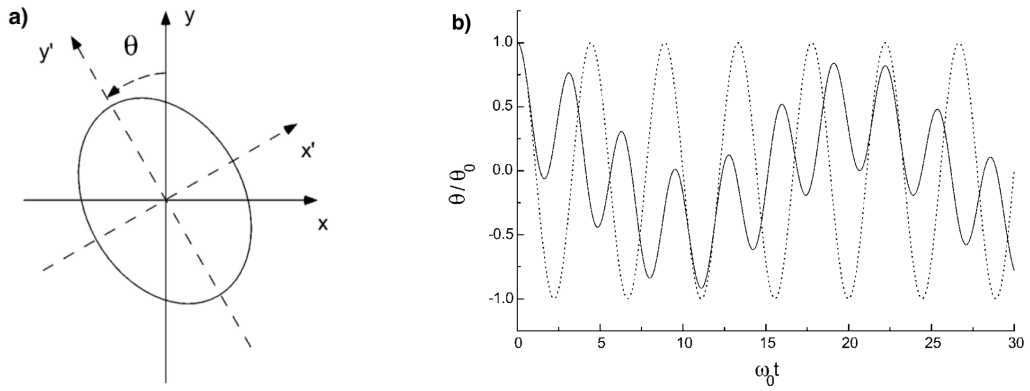

Figure 2.13: **Scissors oscillation: a)** The scissors mode is excited by abruptaly rotate the condensate by a small angle θ in the elliptical plane (x, y). **b)** Angle θ as a function of time for a thermal gas in the collisionless regime (solid line) and for a superfluid (dashed line). In a thermal gas the energy is equally splitted between the two frequencies. Adapted from [14].

of an elliptical trap about a small angle. The name comes from nuclear physics, where deformed density clouds of protons and neutrons perform an out-of-phase oscillation, thus remembering the movement of a scissor.

If, as in figure 2.13.a, we consider a scissors mode excited in the (x, y) plane, the density perturbation δn is proportional to $xye^{-i\omega t}$. Inserting this particular perturbation into equation (2.30) we get the scissors frequency of a non dipolar BEC

$$\omega_{sc} = \omega_{\perp} \equiv \sqrt{\omega_x^2 + \omega_y^2} \tag{2.31}$$

Despite the density change is the same as it would be produced by a rigid rotation of the cloud, the behaviour of the resulting oscillation depends on whether the system is superfluid or not. From equation (2.27), the velocity field of a superfluid varies as $\mathbf{v} \propto \boldsymbol{\nabla}(xy) = (y, x, 0)$, thus is an irrotational motion with zero circulation, as illustrated in figure 2.14. On the other hand, classically the velocity field depends on the interaction regime of the atoms. Two different regimes can be distinguished: the strongly interacting (or hydrodynamic) regime, and the weakly interacting (or collisionless) regime. In the hydrodynamic regime the system oscillates with one single frequency, similarly to a superfluid, but the excitation is characterized by a strong damping. As illustrated with a solid line in figure 2.13.b, in the collisionless regime (which is the characteristic regime of interactions for a quantum gas of neutral atoms) two frequencies appear at $\omega_{\pm} = |\omega_x \pm \omega_y|$. The higher mode ω_+ corresponds to an irrotational quadrupole oscillation analogue to a superfluid, while the lower mode ω_- corresponds to a rigid rotation with a velocity field proportional to $(-y, x, 0)$. This last mode is absent in a superfluid.

Is important to stress that the motion of the cloud is a "rigid" rotation around the trap axis with a defined angle, in the sense that the shape is conserved, only if the parameter

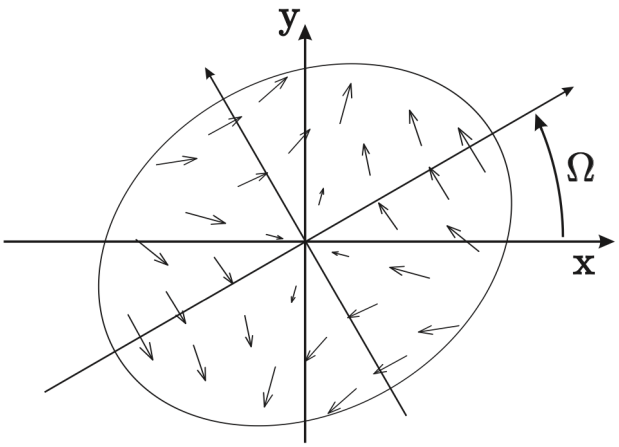

Figure 2.14: **Scissors velocity field of a superfluid:** The irrotational velocity field of a vortex-free condensate in an elliptical trap, rotating at frequency Ω. The small arrows of the velocity field indicate the direction of the quadrupolar flow. Taken from [51]

$\gamma(t) = 2\beta\theta(t)$ is much lower than β (or equivalently $\theta \ll 1$), where

$$\beta = \frac{\langle x^2 - y^2 \rangle_{t=0}}{\langle x^2 + y^2 \rangle_{t=0}} \tag{2.32}$$

is a geometrical factor that depends on the averaged in plane density distribution of the cloud orthogonal to the rotation[1]. If instead γ is larger than β the motion is a quadrupole oscillation characterized by a change of the intrinsic shape and the connection with the scissors oscillation is lost.

The parameter β can be interpreted as the deviation of the BEC shape from cylindrical symmetry. Its value is zero for a perfect cylindrical cloud and continuously grows as the cloud becomes more elongated, until in the 1D limit ($\langle x^2 \rangle \ll \langle y^2 \rangle$) $\beta = 1$. The geometry of a non dipolar condensate or a thermal gas coincides with the geometry of the trap, and the ellipticity of the cloud is given by the in plane frequencies according to

$$\alpha = \left| \frac{\omega_x^2 - \omega_y^2}{\omega_x^2 + \omega_y^2} \right| \tag{2.33}$$

In this case the deviation from cylindrical symmetry coincide with the ellipticity of the trap ($\alpha = \beta$). In a dipolar condensate with the dipoles aligned perpendicularly to the (x, y) plane in general one must consider also the shape variation due to magnetostriction explained in section (2.1.4). Hence β is a function not only of the frequency traps but also of the dipolar strength: $\beta = \beta(\vec{\omega}, \varepsilon_{dd})$ [50].

The deformation of the trap shape has a consequence on the scissors frequency. In dipolar condensates the dependence on the frequency oscillation from the trap frequencies

[1]The avarege is the usual two-dimensional space integral: $\langle ... \rangle = \frac{1}{N} \int d\mathbf{r} \, ... \, n(\mathbf{r})$

and the dipolar strength ε_{dd} is highly non-trivial. Has been calculated by H. J. O'Dell and reads

$$\omega_{sc}^2 = \frac{\alpha}{\beta}(\omega_x^2 + \omega_y^2) \tag{2.34}$$

For a non dipolar condensate where $\alpha = \beta$ one finds the previous result (2.31). If instead the magnetostriction squeezes the cloud in the long direction, β increases and $\omega_{sc} < \omega_\perp$.

2.3.3 Non-classical rotation inertia and scissors mode

In ultracold quantum gases a direct measurement of the momentum of inertia, even more, its deviation from the classical value I_c, is non-trivial. The general way to do it is through $I = \langle L \rangle / \omega$, by rotating the condensate and measuring the angular momentum and the oscillation frequency. However, the direct measurement of the angular momentum induced by the rotation of the trap is difficult in atomic gases, since most diagnostic techniques, based on optical imaging, provide information on the density profiles, either in situ or after the expansion of the gas. Nevertheless in deformed traps, the angular momentum is coupled with the quadrupole mode: by measuring its shape oscillation - the scissors frequency - it is possible to get information about the angular momentum, hence on the moment of inertia [52].

Here we consider a gas initially in equilibrium within a trap rotating with frequency Ω. At $t = 0$ we suddenly stop the rotation of the trap and the gas, due to its inertia, starts a scissors oscillation in the trap frame. The angular momentum is related to the inertia in the usual way $\langle L_z \rangle = \Omega I / N$. The starting point of our analysis is the following commutation rule for a rotation around the z-axis

$$[\hat{H}, \hat{L_z}] = i\hbar m(\omega_x^2 - \omega_y^2)\, \hat{Q} \tag{2.35}$$

where $\hat{L}_z = m \sum_{i=1}^{N} (x\mathbf{v}_y - y\mathbf{v}_x)_i$ is the usual projection of the angular momentum and $\hat{Q} = \sum_{i=1}^{N} x_i\, y_i$ is the relevant quadrupole operator. Note that an elliptical geometry ($\omega_x \neq \omega_y$) is a necessary condition in order to have a coupling between the degrees of freedom of the angular momentum $\hat{L}_z$ and the quadrupole operator $\hat{Q}$. From the first and second time derivatives of the quadrupole operator, and from the time derivative of the angular momentum operator, we got the following equations

$$\frac{d}{dt}\langle Q \rangle = \langle x\mathbf{v}_y + y\mathbf{v}_x \rangle \tag{2.36}$$

$$\frac{d}{dt}\langle x\mathbf{v}_y + y\mathbf{v}_x \rangle = -(\omega_x^2 + \omega_y^2)\langle Q \rangle \tag{2.37}$$

$$\frac{1}{m}\frac{d}{dt}\langle L_z \rangle = \alpha(\omega_x^2 + \omega_y^2)\langle Q \rangle \tag{2.38}$$

The first and second equations describe the motion of a superfluid: they constitute a closed set of equations that brings to the scissors frequency (2.31) [52]. The third equation describes the coupling between the angular momentum and the quadrupole operator and applies to both a classical and a quantum gas, that is for a system with any superfluid fraction.

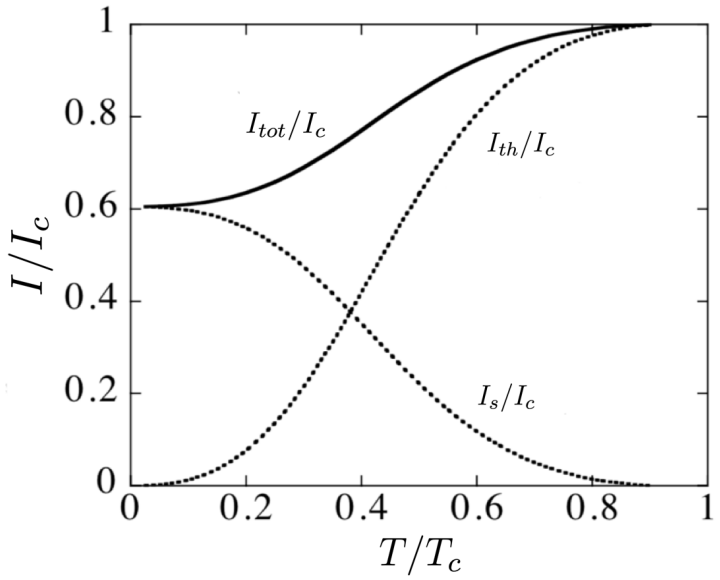

Figure 2.15: **Rotational inertia in an elliptical geometry:** Here is plotted the fraction of inertia versus the temperature of a dilute ultracold gas in an elliptical trap with aspect ratio $\sim$ 3:1 ($\beta^2 = 0.6$), emphasizing the condensed and normal fraction contributions. Due to the negligible quantum depletion, the condensed fraction corresponds to the superfluid fraction and follows equation (2.6). At $T = T_c$ the condensed fraction is zero and the inertia is classical. By lowering the temperature the normal fraction decreases and the inertia follows the solid line. At $T = 0$ the superfluid fraction is equal to unity, and the inertia follows equation (2.41). If the system were in a cylindrical geometry ($\beta = 0$) the condensed contribution I_s/I_c would be zero at any T. Taken from [53].

The knowledge of the time evolution of $Q(t)$ permits to calculate directly the angular momentum $\langle L_z \rangle$. From equation (2.38) one has

$$\langle L_z \rangle = \alpha(\omega_x^2 + \omega_y^2) \int d\omega F(\omega)/\omega \tag{2.39}$$

where $F(\omega)$ is the Fourier signal of the quadrupole operator, which is defined by $\langle Q \rangle(t) = \int d\omega F(\omega) \sin(\omega t)$. The equation (2.39) relates the scissors frequency to the angular momentum $\langle L_z \rangle$, and therefore on the moment of inertia $I = \langle L_z \rangle / \omega$. From the model-independent equation (2.37) one finds the result $\langle x\mathbf{v}_y + y\mathbf{v}_x \rangle = \int d\omega F(\omega)\omega$. For a single frequency quadrupole oscillation, such as a superfluid scissors mode, the Fourier signal $F(\omega)$ is a delta function at $\omega = \omega_{sc}$, and the integral is equal to the scissors frequency. Finally using the relation $\langle x\mathbf{v}_y + y\mathbf{v}_x \rangle = \omega \langle x^2 - y^2 \rangle$ predicted by linear response theory one finds the useful result

$$\frac{I}{I_c} = \alpha\beta \frac{\omega_x^2 + \omega_y^2}{\omega_{sc}^2} \tag{2.40}$$

with the classical inertia defined by $I_c = mN\langle x^2 + y^2 \rangle$. This equation is a major result. In analogy with the torsion oscillator experiment relates the value of the moment of inertia to the scissors frequency.

For a classical gas, the response is dominated by the low-frequency component which is of order $\alpha\omega_\perp$ and equation (2.40) yields the rigid value $I = I_c$. Let us discuss the case of a superfluid: the scissors frequency is the usual (2.34). Accordingly the momentum of inertia (2.40) reads

$$\frac{I}{I_c} = \beta^2 \tag{2.41}$$

This equation tells that the inertia of a superfluid is vanishing for a cylindrically symmetric geometry and approaches the classical value as $\beta \to 1$. An example of the rotational inertia I/I_c of a non cylindrically symmetric quantum gas above and below the critical temperature T_c is illustrated in figure 2.15. The figure emphasizes the thermal I_{th}/I_c and condensed I_s/I_c contribution to the total rotational inertia. Since in a dilute BEC the quantum depletion is negligible, the condensed fraction corresponds to the superfluid fraction $f_s = n_c$. At $T = T_c$ the inertia is classical, while at $T = 0$ the inertia is the expected from a perfect superfluid (2.41) with $\beta^2 = 0.6$.

It is worth to stress that the result (2.41) is valid only for a perfect superfluid, that is with a superfluid fraction equal to unity, which is the case of a dilute Bose-Einstein condensate. However, equation (2.40) is completely general, so it can be used to estimate I/I_c also in a supersolid, where the modulation of the wave function lowers the value of its superfluid fraction, as seen in section (1.2.4). In this case the fraction of inertia would be higher than β^2. Hence, by combining the geometry contribution (2.41) with the definition of superfluid fraction, equation (1.9), it is possible to write a more general equation for the moment of inertia

$$\frac{I}{I_c} = (1 - f_s) + f_s\beta^2 \tag{2.42}$$

To sum up, let us itemize the possible cases:

- $f_s = 0 \quad \to \quad I/I_c = 1 \quad \to$ Classical case
- $f_s = 1 \quad \to \quad I/I_c = \beta^2 \quad \to$ Superfluid case
- $0 < f_s \leq 1 \to \; I/I_c = (2.42) \to$ Supersolid case

It is now possible to relate the fraction of momentum of inertia of a superfluid with its scissors frequency, even when $f_s \neq 1$. Inserting equation (2.34) into (2.42) and solving for f_s we obtain

$$f_s = \frac{1 - I/I_c}{1 - \beta^2} = \frac{1 - \alpha\beta(\omega_x^2 + \omega_y^2)/\omega_{sc}^2}{1 - \beta^2} \tag{2.43}$$

Naturally a dilute BEC oscillates with the single frequency (2.34) and equation (2.43) yields $f_s = 1$. On the contrary if a gas with the same trap geometry α and density distribution β oscillates with a slower frequency, this implies a larger fraction of inertia and equation (2.43) yields to a lower superfluid fraction.

Chapter 3

Obtaining a dipolar supersolid

In this chapter, we present the ingredients to obtain a dipolar supersolid. We will first introduce the main characteristics of ^{162}Dy, the strongly magnetic element we use to produce a dipolar supersolid. Then we will give a short introduction to the cooling techniques employed to achieve a BEC of Dy atoms, and the experimental strategy implemented to obtain a dipolar supersolid. Finally, we will explain how we fit the supersolid, and its main characteristics, such as elementary excitations and the lifetime.

3.1 Dysprosium

Dysprosium is a rare-earth element that belongs to the group of lanthanides, showed in figure 3.1. The atomic number is 66, it melts at 1412°C at atomic pressure and it boils at 2560°C. Dysprosium possesses seven stable isotopes with different abundances. The isotope in which we are interested in is the boson with 96 neutrons, the isotope 162, whose abundance is about 25.5%. The choice dysprosium for our experiment must be searched in its high intrinsic magnetic dipolar moment, which is of $\mu_m = 9.93\,\mu_B$, the highest between all atomic elements. It is precisely this high dipolar moment responsible of strong dipolar interactions, that permits the characteristic modulation of the wave function of the supersolid. To understand where this high magnetic momentum comes from, we have to look at its electronic structure.

The 66 electrons of dysprosium lead to the electronic configuration of $[Xe]4f^{10}6s^2$, which is a submerged-shell configuration, where the $6s$ shell is inside the $4f$ shell. While the s orbital is completely filled, the f one is not. This leads to a complex electronic structure with a large orbital angular quantum number of $L = 6$ and an electronic spin of $S = 2$, resulting in a total angular momentum of $J = L + S = 8$. The resulting electronic ground state has a term symbol $^5I_8$. It is precisely this ground state that brings to a lot of interesting characteristics, including its high intrinsic dipolar moment.

The intrinsic dipolar moment, together with the mass of ^{162}Dy of $m = 161.93$ a.u., provides a value of the dipolar length scattering (2.13) of approximately

$$a_{dd} \simeq 130 a_0 \tag{3.1}$$

Considering its s-wave background length scattering $a_{bg} \simeq 92 a_0$, results in a background dipolar strength of approximately $\varepsilon_{dd} \simeq 1.42$.

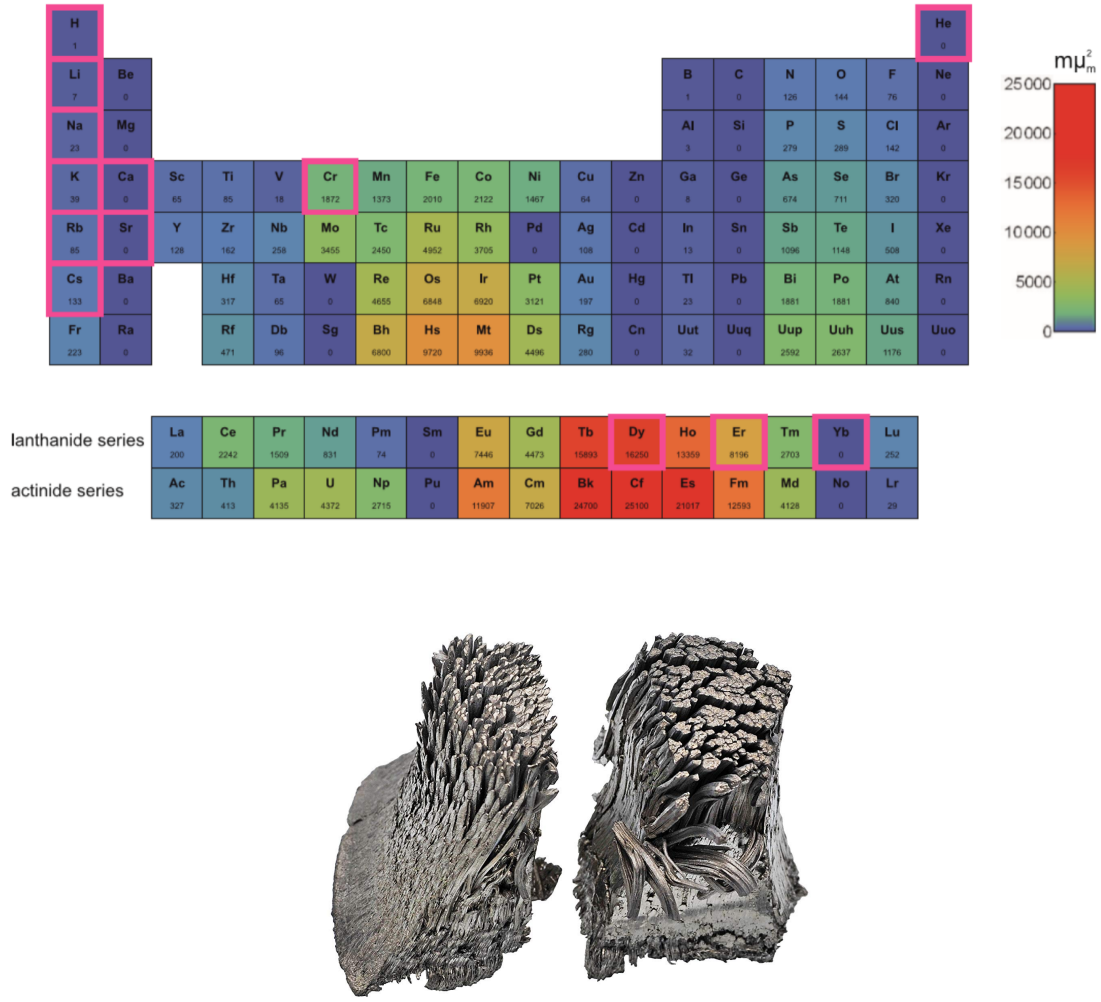

Figure 3.1: **Dysprosium:** Above: The periodic table of elements. Pink borders highlight the elements that have been successfully condensed. The color represents the dipolar character of each element. Red indicates the highest, blue the lowest. Below: The dysprosium element is characterized by a metallic silver luster. It is never found in nature as a free element, thus it must be isolated from other minerals such as Xenotime.

Another consequence of the complex electronic structure is a dense energy spectrum, partially shown in figure 3.2. This character derives from the possibility of exciting an electron of the s or f orbital equally likely. The most useful transitions to cool the atoms are the optical transitions at 421 nm and at 626 nm. The first one is a broad transition with a linewidth of $\Gamma_{421} = 2\pi \times 32.2$ MHz. It is used in the Zeeman Slower and in the Transverse Cooling, as well as in the absorption imaging. Since the thermal velocity of the atoms is ~ 450 m/s, with a broad dispersion due to the high melting temperature of

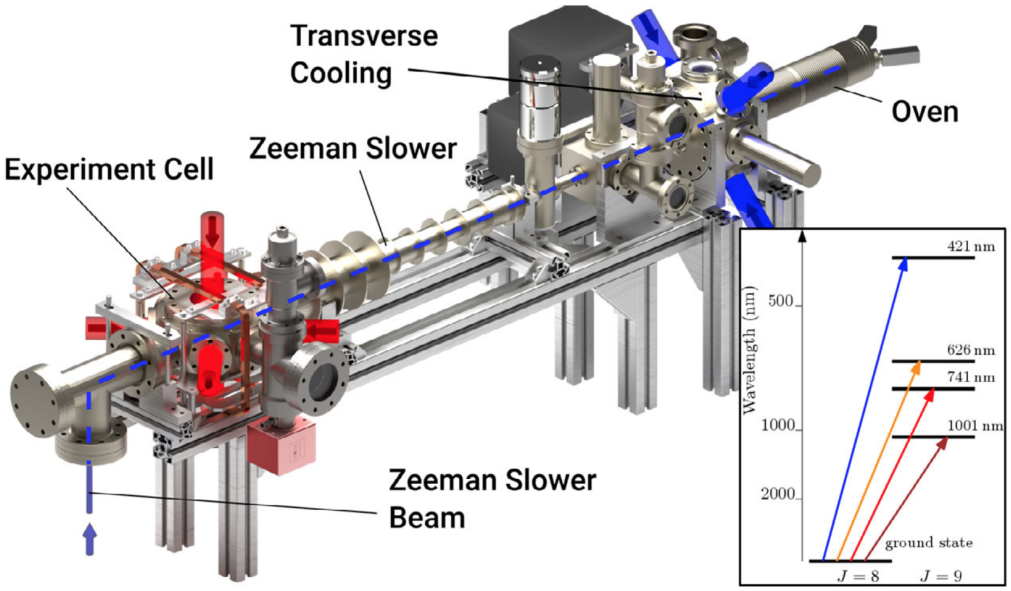

Figure 3.2: **Experimental apparatus:** Here are illustrated the main parts that constitue the vacuum chamber. The transitions in which we are interested are the broad transition at 421 nm (Blue) and the narrow transition 626 nm (Red).

Dy, the broad character of this transition suites to first slow down the atoms coming out from the oven. The second transition has a narrower linewidth of $\Gamma_{626} = 2\pi \times 136$ KHz and is used in the Magneto Optical Trap (MOT). Due to its narrow character it provides extremely cold MOT (Doppler temperature of about 6 μK).

3.2 Experimental setup

In this section, we give an overview of the setup and the steps used to create a degenerate gas and subsequently a dipolar supersolid of dysprosium. It includes basic of light-matter interaction, laser cooling, and evaporative cooling in optical dipole traps. The main steps are:

- Creation of a thermal atomic beam via sublimation of crystalline dysprosium.
- Collimation of the atomic beam with a transverse cooling (TC) and deceleration of the atomic beam with the Zeeman slower (ZS).
- Cooling and trapping in a magneto-optical trap (MOT).
- Trapping and evaporative cooling in a large-volume resonator-enhanced optical trap.
- Transfer of the atom in a crossed optical dipole trap, and forced evaporation to quantum degeneracy.
- Tuning of the experimental parameters to create the supersolid and to excite it.

- Detection of properties of the system via time-of-flight absorption imaging.

All this procedure is done in a vacuum chamber that protects the atoms from the environment. As illustrated in figure 3.2, the setup consists of 4 main parts: the effusive cell heated up by an oven, the transverse cooling chamber, the Zeeman slower arm, and the experiment chamber. But first, let us give a brief theoretical introduction of light-matter interaction.

3.2.1 Light-matter interaction

In the following treatment, we will consider an atom with two levels in an electromagnetic field produced by laser light. In the *two-level approximation*, the atom is described as a two-level system where only closed transitions are possible. When the atom absorbs a photon, the atom gets excited and acquires its momentum. Subsequently, the atom spontaneously decays in the ground state emitting the photon in random direction. The force that the light field imprints on the atom depends highly on the relative energy between the photon and the two-level transition. For resonant interactions $\omega_{21} \sim \omega_L$ the force is dissipative and brings to the phenomena of Doppler cooling. For off-resonant interactions $\omega_{21} \ll \omega_L$ ($\gg$) there is no absorption/emission of photons. Instead the light produces an induced dipole on the atom that allows its trapping in a conservative potential [40].

Resonant interaction

When an incident photon interacts with an atom, if the frequency of the photon is approximately the frequency of the atom transition the atom absorbs the photon and gets excited. This process preserves the energy $\hbar\omega_L$ and the momentum $\hbar k$ of the photon. Therefore the atom gets a kick in the direction of the photon, then spontaneously decay emitting the photon in random direction with spherical symmetry. For an atom moving in the opposite direction of the laser, the average result is to lower its velocity. This phenomenon is called radiation pressure. The force that the photon imprints on the atom is

$$F_{\text{scatt}} = \frac{\Delta p}{\Delta t} = \hbar k \Gamma_{scatt} \tag{3.2}$$

where Γ_{scatt} is the scattering rate, i.e., the number of photons absorbed in the unit time. As every absorption is followed by an emission $\Gamma_{\text{scatt}} = \gamma\rho_{22}$ where γ is the linewidth of the excited state and ρ_{22} its population. For a laser with intensity I and detuning $\delta = \omega_L - \omega_{21}$ the scattering rate reads

$$\Gamma_{\text{scatt}} = \frac{\gamma}{2} \frac{S_0}{1 + S_0 + (\frac{2\delta}{\gamma})^2} \tag{3.3}$$

where $S_0 = I/I_{sat}$ is the saturation parameter of the transition, i.e., the parameter at which by increasing the intensity, the scattering rate does not increase consequently. In general, the detuning depends on the relative velocity of the atom. Thus the Doppler shift on the frequency must be considered and the detuning reads: $\delta = \omega_L - \omega_{21} - \mathbf{k} \cdot \mathbf{v}$. The maximum force that can be implemented to an atom is in the resonant condition ($\delta = 0$) and $S_0 \gg 1$. It reads

$$F_{\text{scatt}}^{Max} = \frac{\hbar k \gamma}{2} \tag{3.4}$$

is equivalent to say that the atom acquires a momentum $\hbar k$ in the time necessary to absorb a photon $t = 2/\gamma$.

The scattering force is a fundamental property that - among other things - permits to cool atoms. By integrating a system with 6 laser beams - 2 per axis - all directed in the same point, and appropriate magnetic fields, it is possible to cool atoms at Doppler and Sub-Doppler temperatures. This mechanism is at the base of the experimental techniques of the ZS and the MOT.

Dipole interaction

When the detuning is large, the interaction is not related to the absorption/emission of photons but the field induces a dipole polarization of the electronic structure of the atom, which oscillates with the same frequency as the electric field. A full theoretical treatment uses the *dressed atom picture* in which the atom and the photon are considered all together. In the dipole approximation, the interaction can be written as

$$V(\mathbf{r}, t) = -\mathbf{d} \cdot \mathbf{E}(\mathbf{r}, t) \tag{3.5}$$

where $\mathbf{d}$ is the electric dipole operator for a single atom and $\mathbf{E}$ is the electric field. If the time averaged electric field varies with position, the shift on the energy due to the field gives rise to a force

$$F_{\text{dipole}} = -\boldsymbol{\nabla} V(\mathbf{r}) = \frac{1}{2}\alpha'(\delta)\boldsymbol{\nabla}\langle \mathbf{E}(\mathbf{r}, t)\rangle_t \tag{3.6}$$

where $\alpha'(\delta)$ is the dipole dynamic polarizability. At low frequencies $\delta < 0$ (red detuning) the polarizability is positive, and the dipole moment is in the same direction as the electric field. Therefore for frequencies below the resonance, the force is towards regions with a high electric field. On the other hand for frequencies higher than the resonance $\delta > 0$ (blue detuning) the induced dipole is in the opposite direction and the force is towards regions with a low electric field.

By focusing a laser beam is it possible to create a radiation field whose intensity has a maximum in space. If the frequency of the light is red detuned with respect to the transition the atom feels an energy minimum in space. Therefore it is possible to trap atoms in the so-called Optical Dipole Traps (ODT). Most of the laser beams have a gaussian intensity profile

$$I(r, z) = \frac{2W}{\pi w_o^2}\frac{1}{1 + (\frac{z}{z_R})^2}e^{-\frac{2r^2}{w^2(z)}} \tag{3.7}$$

where z is the propagation direction of the beam, r the radial plane perpendicular to z, W the power, w the beam waist in a generic z position, z_R the Rayleigh distance and w_0 the beam waist at the focus position. Thus atoms feel a gaussian potential that leads to a gaussian spatial distribution

$$n(x, y, z) = n_0 e^{-\left(\frac{x^2}{2\sigma_x^2} + \frac{y^2}{2\sigma_y^2} + \frac{z^2}{2\sigma_z^2}\right)} \tag{3.8}$$

As the intensity of the laser is proportional to the power W of the beam, and inversely proportional the waist w_0^2, to create an ODT are necessary high powers, focused beams and large red detuning.

The force that permits optical traps is conservative, thus it does not cool atoms. However, by slowly lowering the beam power, the most energetic atoms leave the trap, decreasing the average energy per particle. This mechanism is at the basis of evaporative cooling, which is the last cooling procedure, essential to reach quantum degeneracy.

3.2.2 Obtaining quantum degeneracy

Effusion cell and Zeeman slower

This part describes the travel of the atoms from the solid phase to the MOT in the experiment chamber. First, a high purity sample of few grams of dysprosium in its solid crystalline phase is placed into the oven. The effusive oven cell is maintained at a pressure of $\sim 10^{-7}$ Torr. By heating up the oven at $T \simeq 1200 \div 1250$°C, the atoms sublimate to the gas phase. The atomic beam spreads out of the oven in all directions, with a thermal velocity of ~ 450 m/s. As the experiment chamber is maintained at Ultra-High Vacuum (UHV) with an increasing differential vacuum from the Transverse cooling to a pressure of $< 10^{-10}$ Torr, most of the atoms spread in the direction of the experiment chamber. Since the MOT can trap atoms at velocities of a few m/s a first cooling step must be implemented. The first two cooling methods are transverse cooling and Zeeman slower. Both use the same blue laser source at 421 nm, generated by a frequency doubled Ti:Sapphire. The transverse cooling is a two-dimensional optical molasses that slows the atomic beam in the plane perpendicular to the Zeeman slower arm. Besides lowering the temperature, it increases the capture efficiency of the ZS. The overall power of the TC is ~ 75 mW, it is divided in 2 retro-reflected outputs, with a detuning of $\sim -3\,\Gamma_{421}$. On the other hand, the ZS uses ~ 150 mW of power in an elliptical molasses with a detuning of $\sim -32.8\,\Gamma_{421}$. These two techniques permits to slow the atoms from a velocity of 450 m/s to ~ 10 m/s. At the end of the ZS and right before the MOT a compensation magnetic field is produced by rectangular coils in quasi-Helmotz configuration to compensate the field emerging from the ZS itself.

Magneto optical trap

Atoms are now ready to be loaded into the MOT. A scheme of a MOT is illustrated in figure 3.3. The MOT consists of three retro-reflected laser beams at 626 nm and two circular coils in the vertical axis placed in an anti-Helmotz configuration that generates a linear magnetic field gradient parallel to the plane. The light at this wavelength is obtained by a compact diode laser device by Toptica. The horizontal beams have a power of ~ 65 mW and the vertical of ~ 90 mW. The MOT operates in two subsequent stages. In the first loading stage, the capture velocity of the MOT is artificially increased by a modulation of the laser frequency via AOMs, with a detuning of $\sim -35\,\Gamma_{626}$. In the second compression stage, the modulation is switched off and the detuning is set closer to the atomic resonance ($\sim -8\,\Gamma_{626}$) together with a decrease of the intensity, to maintain a sufficient confining force, to increase the phase space density. After the compression, the typical atom number in the MOT is of $\sim 6 \times 10^7$, with a gaussian RMS width of 450 μm in the horizontal plane and 150 μm in the vertical plane. The typical temperature at this stage is $\sim 15\mu$K.

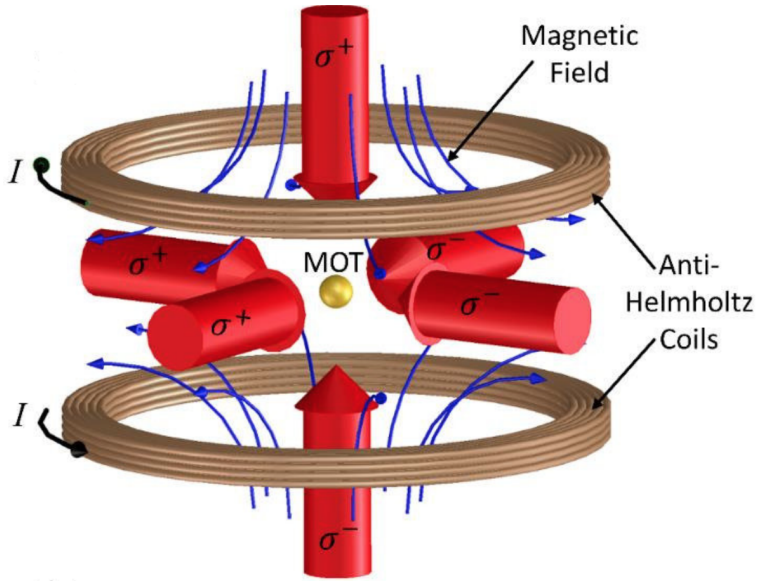

Figure 3.3: **Magneto optical trap:** Schematic rapresentation of a MOT. The atom beam coming from the Zeeman slower converge in the center of the MOT loading the atoms on it. The circular coils creates a quadupole magnetic field using the so-called anti-Helmotz configuration.

Resonator-enhanced optical dipole trap

After the MOT compression the atoms are loaded in a large-volume optical trap enhanced by an in-vacuum optical resonator. This trap is realized by a standing wave pattern inside an optical resonator, produced by a single-mode Nd:YAG laser at 1064 nm. The resonator permits to amplify the power of the seeding beam about 1000 times. Therefore we achieve large trapping volumes and trap depths without employing high power multi-mode lasers, which tend to cause heating and losses [ref]. Since the polarizability of dysprosium with light at 1064 nm is $\alpha' = 184.4$ a.u. [ref Grimm], 1W of power permits to create a trap depth of 200 μK with a waist of 320 μm. Since the resonator creates a standing wave, it produces a periodic lattice superimposed to the atomic system with periodicity $\lambda/2 = 534$ nm. At the end of the compression stage, the power of the resonator is ramped up (stage I in figure 3.4) while the atoms coming from oven cell are blocked by a pneumatic shutter. The geometrical superposition is optimized by changing the MOT position with small magnetic bias fields. The resonator reaches a loading of 3×10^7 atoms at a temperature of $\sim 30\mu$K.

Optical dipole traps

At this point atoms are evaporated in the resonator up to typical temperatures of 4 μK with few-millions atoms. During the evaporation, atoms are loaded into ODT1, an optical dipole trap with a circular waist of 41 μm and a power of 1.5 W. The evaporation sequence is shown in figure 3.4 (stage II). It consits in turning on ODT1 while slowly decrease the power of the resonator in 2 seconds. Because of the impossibility of superimposing exactly the resonator with ODT1, the loading is optimized by positioning with an angle of 8°.

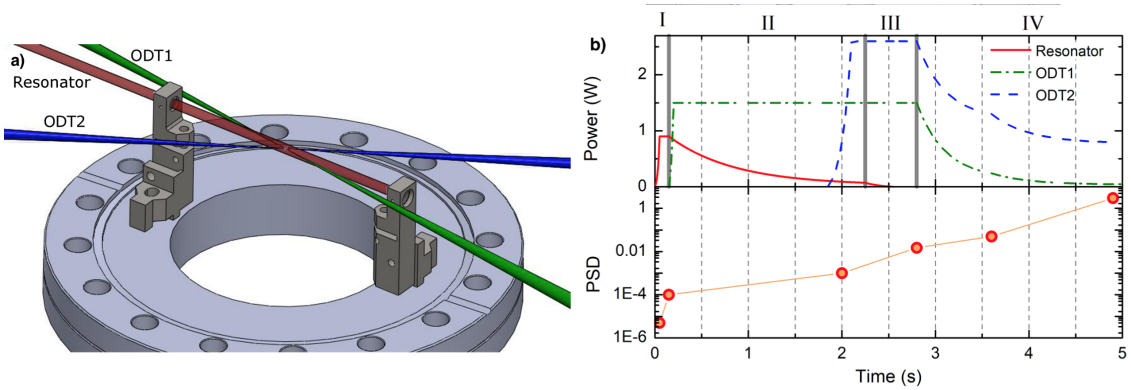

Figure 3.4: **Experiment sequence: a)** schematic of the resonator (red) and ODT1 (green) and ODT3 (blue). The angle between the resonator and ODT1 is 8°. **b)** Power of the traps and phase space degeneracy (PSD) through the experimental cycle. The sequence is divided into 4 stages: (I) MOT compression and resonator loading, (II) evaporation in the resonator, (III) the resonator is off and atoms are in ODT1-ODT3, and (IV) at the end of the evaporation in ODT1-ODT2 the gas reaches quantum degeneracy.

When the resonator is almost off and atoms are trapped in ODT1 the power of a second, elliptical dipole trap (ODT2) is ramped up (stage III). This trap is positioned with an angle of 40° with respect to ODT1. The horizontal (vertical) waist is of 81 μm (36 μm), with an initial power of 2.6 W. With these two traps it is possible to confine the atoms in the 3 directions. Finally, the atoms are further cooled by evaporation by slowly lowering the power to $P_{\mathrm{ODT1}} = 50\,mW$ and $P_{\mathrm{ODT2}} = 800\,mW$ (stage IV), where quantum degeneracy is reached and a BEC is achieved.

The two optical dipole traps are constructed to have the stronger confinement along the vertical axis, the direction of the polarization, to satisfy the stabilization condition (see section 2.1.4). Typical final frequencies are $\omega_{x,y,z} = 2\pi \times (20, 60, 90)$ Hz, with $\lambda \simeq 1.4$. All the intensity lasers used are tuned by means of AOMs and stabilized with a feedback loop.

3.2.3 Imaging

All information on atoms is obtained by absorption imaging. It is performed by a camera positioned above the experiment cell that sends blue light (421 nm) on the atoms, imaging the horizontal (x, y) plane. Absorption imaging completely destroys the atom cloud.

The imaging procedure consists of three images in rapid sequence. The first one (Img_1) sees the shadow created by the atoms, the second one (Img_2) takes a picture of the light present in the chamber without the atoms, including the lasers, and in the third one (Img_3) the beams are turned off and only the background light is captured.

The images can be taken both *in situ*, that is only a few ms after the shut off of the traps, or after a variable time of free expansion, called time-of-flight (TOF). From the intensity of the light in the pictures can be extrapolated the column density distribution

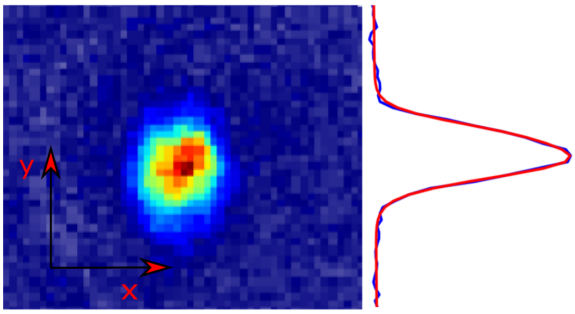

Figure 3.5: **Column density distribution:** Image of a BEC in false colors and density profile. The colors indicates optical thickness, with red as the higher and blue the lowers. The density profile (in blue) is fitted with a 1D gaussian function (red).

of the atoms

$$Img = -\ln\left(\frac{Img_1 - Img_3}{Img_2 - Img_3}\right) = \int_0^z n(x,y,z)\,\sigma I \tag{3.9}$$

where $n(x,y,z)$ is the 3D density of the cloud, σ the cross-section between the atoms and the laser that takes into account the scattering probability and I is the light intensity. Thus absorption imaging in the z-direction is equivalent to a measure of the column density distribution of the atoms. Considering a gaussian like density distribution, the image is

$$Img(x,y) = \frac{\sigma N}{2\pi}\frac{1}{\sigma_x\sigma_y}\,e^{-\left(\frac{x^2}{2\sigma_x^2}+\frac{y^2}{2\sigma_y^2}\right)} \tag{3.10}$$

By fitting the image with a two-dimensional gaussian function with a certain amplitude A it is possible to obtain the total number of atoms with $N = 2\pi\sigma_x\sigma_y A/\sigma$. Typical atoms number is $1 \div 5 \times 10^4$. Note that to convert pixels of the image into actual physical quantities a conversion of the units must be carried.

As every image sequence is destructive, to study the evolution of the atoms in the trap or the physics of the expansion the images must be taken at different times, and then reconstruct the position.

3.3 Observation of a dipolar supersolid

3.3.1 Supersolid production

Following the sequence of section 3.2.2, a polarized BEC is produced with a typical atom number of 3.5×10^4. The trap frequencies that result from the contribution of the superimposed ODT1-ODT2 are $\omega_{x,y,z} \simeq 2\pi \times (20, 60, 90) \pm 2$ Hz, with an in-plane aspect ratio $\omega_y/\omega_x = 3$. This gives an alpha value of $\alpha = 0.6$. (figure 3.6.a)

The condensate is initially created at the background scattering length $a_{bg} = 157(4)\,a_0$. We employ a specific set of three Feshbach resonances located at $B_1 = 5.145$ G, $B_2 = 5.231$ G, and $B_3 = 5.244$ G to tune the scattering length. The widths of first and second FRs are

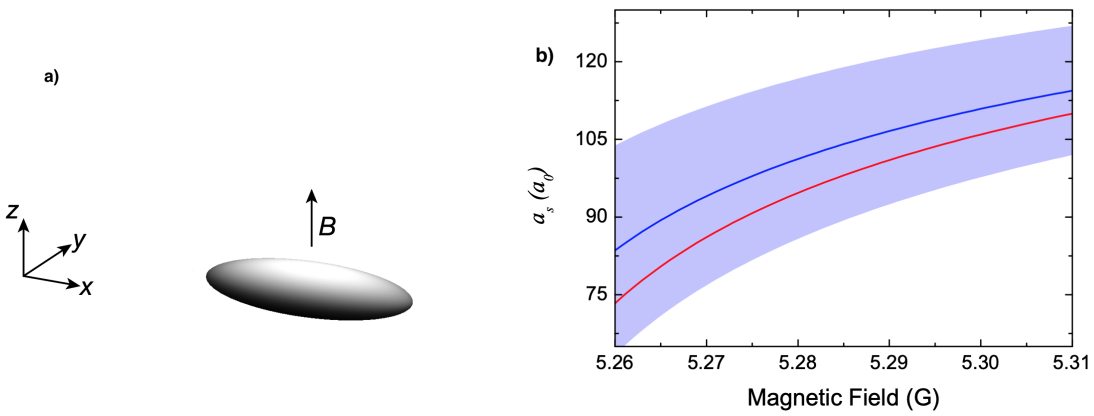

Figure 3.6: **Supersolid production: a)** The resulting optical dipole traps produces an effective potential with an in-plane aspect ratio of 3:1 and a strong confinement in the polarized z-axis. **b)** Contact scattering length versus the magnetic field. The blue-solid line represents the best estimate for $a_s(B)$. The blue region sets the limits confidence, given the experimental uncertainty. The red-solid line is the conversion of $a_s(B)$ used throughout the paper, obtained by comparing experimental and theoretical observations. Taken from [7].

$\Delta B_1 = 32$ mG and $\Delta B_1 = 8$ mG respectively, while the third one is of order of 1 mG [7]. The resulting dependence of the scattering length with the magnetic field is illustrated in figure 3.6.b. Considering the dipolar scattering length of dysprosium of $a_{dd} = 130\,a_0$, the condensate has a dipolar strength of $\varepsilon_{dd} = 0.83$. The s-wave scattering length is then tuned with a 70 ms linear ramp to $a_s = 114\,a_0$ ($\varepsilon_{dd} = 1.14$), close to the supersolid transition. The transition, at these frequencies and atoms number, is located around $\varepsilon_{dd} = 1.38$, which correspond to $a_s \simeq 94\,a_0$. After the first ramp, a secondary linear ramp of 30 ms brings the system in the supersolid regime. The systematic uncertainty on a_s of about $3a_0$ gives an uncertainty on ε_{dd} of 3%.

The transition BEC-SS is crossed as adiabatically as possible, i.e., slow enough to prevent exchange of energy between the apparatus and the atoms. However, the crossing of the phase transition naturally excites in the supersolid regime the axial breathing mode. The typical amplitude of this breathing oscillation on the supersolid width is about 10%. Even tuning the scattering length ramp parameters, we cannot avoid this small excitation of the system. This amplitude is, therefore, the minimum accessible to the supersolid. The oscillation is revealed by monitoring the width momentum distribution in the x-direction $\tilde{n}(k_x)$ after a TOF expansion. This naturally triggered oscillation was use to probe the character of the excitation modes in a dipolar supersolid (see section 2.2.3).

3.3.2 Supersolid analysis

A non-interacting Bose-Einstein condensate with a certain in trap Gaussian distribution $n(x, y)$, when released expands with a velocity distribution according to the uncertainty

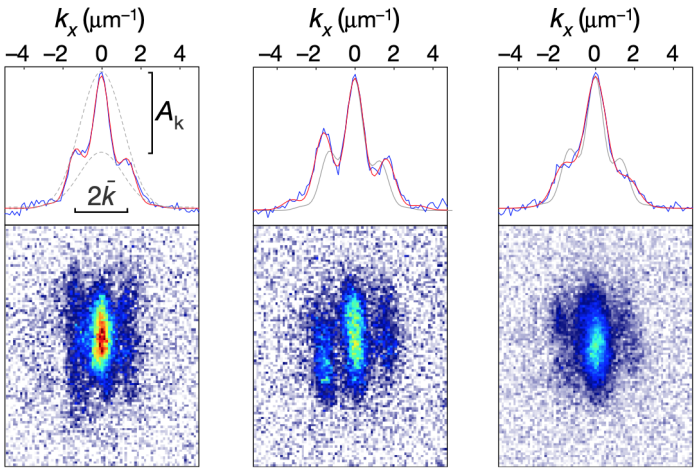

Figure 3.7: **Momentum distribution of a dipolar supersolid:** two dimensional absorption images after TOF at 3 different evolution time 25 ms, 40 ms and 95 ms (lower panels) and related fits of the one-dimensional distribution $n(k_x)$ with the function (3.16). Adapted from [7].

principle

$$v_i = \frac{\hbar}{m\sigma_i(0)} \tag{3.11}$$

where $\sigma_i(0)$ is the confinement of the condensate in the i-direction. Considering the ground state of the harmonic oscillator, the confinement is given by the trap frequencies by the oscillator length $a_{ho,i} = \sqrt{\hbar/m\omega_i}$. The width at a time t after the release reads

$$\sigma_i^2(t) = \sigma_i^2(0)(1 + \omega_{0,i}^2 t^2) \tag{3.12}$$

for $t^2 \gg 1/\omega_0^2$ the shape of the condensate is determined only by the trap frequencies. Therefore given an initial Gaussian-like density distribution, acquiring the image in TOF corresponds to observe the momentum distribution of the condensate $\tilde{n}$

$$n(x, y) \rightarrow TOF \rightarrow \tilde{n}(k_x, k_y) \tag{3.13}$$

As we discussed in section 2.2.3 the supersolid corresponds to a modulated BEC in the x-direction with the phase locked throughout the cloud. The distribution along the modulation $\tilde{n}(k_x)$ after the free expansion of the cloud can be modeled with a multiple slit function, where the slits correspond to density peaks, i.e. coherent droplets. Our current resolution prevents us from estimating if more than two stripes are present.

The resulting distribution is the product of the interference pattern with the diffraction pattern $I = I_{int} I_{diff}$. The double-slit interference of an incident plane wave at a distance d fixes the position of the fringes according to

$$I_{int} = I_0 \cos^2\left(\frac{\pi d \sin\theta}{\lambda}\right) \tag{3.14}$$

while the single-slit diffraction with width D modulates the peaks amplitude according to

$$I_{diff} = I_0 \sin^2\left(\frac{\pi D \sin\theta}{\lambda}\right) \Big/ \left(\frac{\pi D \sin\theta}{\lambda}\right)^2 \tag{3.15}$$

where θ is the propagation angle of the scattered wave from the center of the incident beam. However, our cloud is slightly different from a homogeneous plane wave propagating through well defined and fixed slits. The interference pattern must take into account the original background density distribution of the trapped atoms, therefore the fit must be modulated with a Gaussian. Secondly, some of the background distribution remains and it is necessary to sum a Gaussian with the modulation in the fit. And ultimately, while the distance between the droplets (slits) is fixed ($d \simeq 1/k_{rot}$), their position throughout the cloud varies from shot to shot. It is like the incident wave hits the slits with a different phase each time. The interference pattern is "moved" using a phase ϕ. The final fit function reads

$$\tilde{n}(k_x) = C_0\, e^{-(k_x - k_{0,x})^2/2\sigma_x^2}\left[1 + A_k \cos^2\left(\frac{\pi}{\overline{k}}(k_x - k_{0,x}) + \phi\right)\right] \tag{3.16}$$

where $k_{0,x}$ is the center of the cloud, σ_x its dimension after the expansion, C_0 the amplitude of the background Gaussian and $C_0 A_k$ the amplitude of the stripes with period $\overline{k}$. The interference amplitude A_k provides information on the depth of the density modulation. The interference phase ϕ provides instead a measure of the robustness of the stripe pattern, both in what concerns the phase locking between the stripes and their relative distances. An example of the fit is shown in figure 3.7.

The modulated term is essentially the Fourier transform of the in-trap lattice, while the background Gaussian is related to the unmodulated component of the in-trap density. Because of the non-trivial expansion of a dipolar gas, in particular, due to the interaction term in the Hamiltonian, it is not possible to analytically relate the in trap density to the distribution in k space.

3.3.3 Lifetime of a dipolar supersolid

As illustrated in figure 3.8.b, when the transition BEC-SS is performed, the modulation pattern grows till the metastable value of $A \simeq 0.5$ with an exponential increase in approximately 10 ms. The modulation remains stable for ~ 30 ms and then decreases until, over 100 ms, the characteristic supersolid pattern disappears (third image of figure 3.7). The loss of modulation is caused by the decrease of the atom number (figure 3.8.a), which has the effect of leveling the droplets. This loss of supersolid character is, however, not related to the loss of phase coherence since the latter remains high at any time despite quantum and thermal phase fluctuations, and the axial breathing oscillation [7].

The main contribution that diminishes the number of atoms of a degenerate gas is the phenomena called three-body losses. This phenomenon is an inelastic scattering process consisting of the interaction among three atoms, resulting in one molecule and one free atom.

$$3\mathrm{Dy} \rightarrow \mathrm{Dy}_2 + \mathrm{Dy} \tag{3.17}$$

Two atoms can not combine directly, because, to get rid of the momentum and the energy released from the molecule binding energy, a third atom needs to participate in the process.

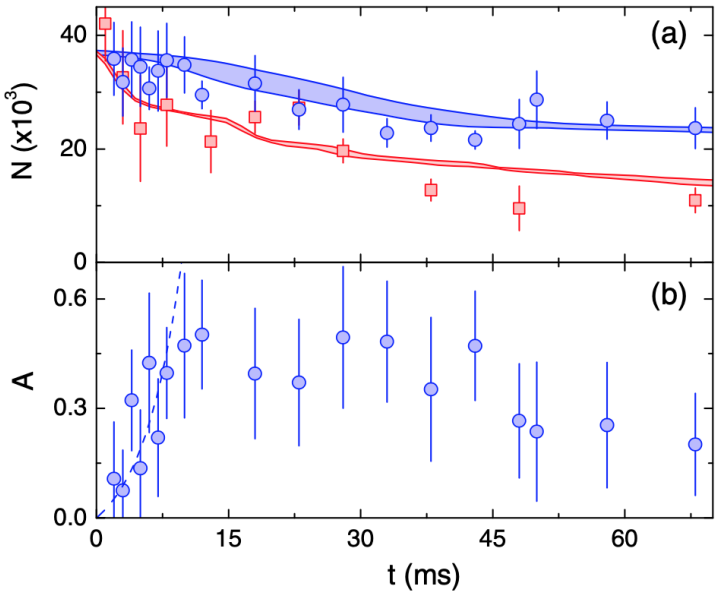

Figure 3.8: **Atom number and modulation pattern: a)** The lifetime of a supersolid is about 100 ms. The number of atoms follows an exponential decay: $N(t) = N_0 \exp(-t/\tau)$, with decay rate $\tau \simeq 100$ ms. The shaded areas show the dynamical simulations for a SS (blue) and ID (red). **b)** Time evolution of the interference amplitude A in the supersolid. The dashed line is an exponential fit to the initial ($t \leq 10$ ms) growth. The error bars represent the standard deviation of about 40 measurements. Taken from [7].

The binding energy is transformed into kinetic energy that results in the loss of the molecule and the atom. For a thermal gas, the rate of the recombination is

$$\frac{dn}{dt} = -K_3 n^3 \tag{3.18}$$

where K_3 is the three-body recombination coefficient of the species considered. Seems natural that the process is proportional to the third power of the density. The probability of a single particle to be in a certain volume V is proportional to n. Thus for three particles is proportional to n^3.

By integrating (3.18) and considering that in a BEC due to indistinguishability of particles the three-body coefficient is only the sixth part of the thermal coefficient, we get

$$\frac{1}{N}\frac{dN}{dt} = -\frac{K_3}{6}\langle n^2 \rangle \tag{3.19}$$

the decay time of the condensate is therefore $\tau_{loss} = 1/K_3\langle n^2 \rangle$. The value of the three-body coefficient of ^{162}Dy is $K_3^{BEC} = 1.5 \times 10^{-27}$ cm^6/s [7].

Since the three-body losses is proportional to $\langle n \rangle^2$ phenomenon limits the peak density of the system. In a BEC the majority of losses happen in the central region, while in a SS or ID in the center of the droplets. With the value of decay rate and K_3 coefficient it is possible to calculate the mean density $\langle n \rangle \simeq 5 \times 10^{14}$cm^{-3}. This is about 10 times larger than the calculated BEC density, suggesting that, in both modulated regimes, the Lee-Huang-Yang (LHY) repulsion has a stabilizing role.

Chapter 4

Observation of NCRI in a dipolar supersolid

The central result of this thesis is reported in this chapter: the observation of a reduced moment of inertia (NCRI) when a trapped dipolar supersolid of ^{162}Dy is excited through the scissors mode. From the measured moment of inertia, we infer a superfluid fraction which is different from zero and of the order of unity, providing direct evidence of its superfluid nature.

The first section of this chapter is devoted to discussing the methods employed to excite the scissors mode of a BEC and a SS in order to unveil their superfluid behavior. We analyzed the time-of-flight images to get information on the shape evolution and the scissors frequency of the gas.

The finite temperature analysis of the scissors mode performed in section 4.2.2 shows that, while the BEC oscillates with a single frequency, a thermal cloud oscillates with two frequencies, as expected from section 2.3.2. This confirms the collisionless regime of our system, hence its truly superfluid character.

Once confirmed the superfluid nature of the sample, using the procedure explained in section 3.3.1, we investigate the scissors oscillation in the supersolid phase. We observe a reduction of the scissors frequency, pointing to an increase of the fraction of the rotational inertia. Subsequently, from the measured scissors frequency and a numerical estimation of the system's deformation β, we extract the moment of inertia and we infer a superfluid fraction different from zero and of order of unity. We also compare the superfluid fraction with the theoretical Leggett's prediction introduced in section 1.2.4.

The scissor mode of the incoherent droplet crystal has not been investigated because of its short lifetime due to three-body losses [7], although, following Leggett's criterion, an almost zero superfluid fraction is expected [49].

4.1 Exciting the scissors mode

Our experiment starts with a dipolar quantum gas trapped in an harmonic trap with variable trapping frequencies (I will discuss later how we choose the final trapping frequencies). As shown in figure 3.6.a the dipoles are oriented in the z-direction by a magnetic field B,

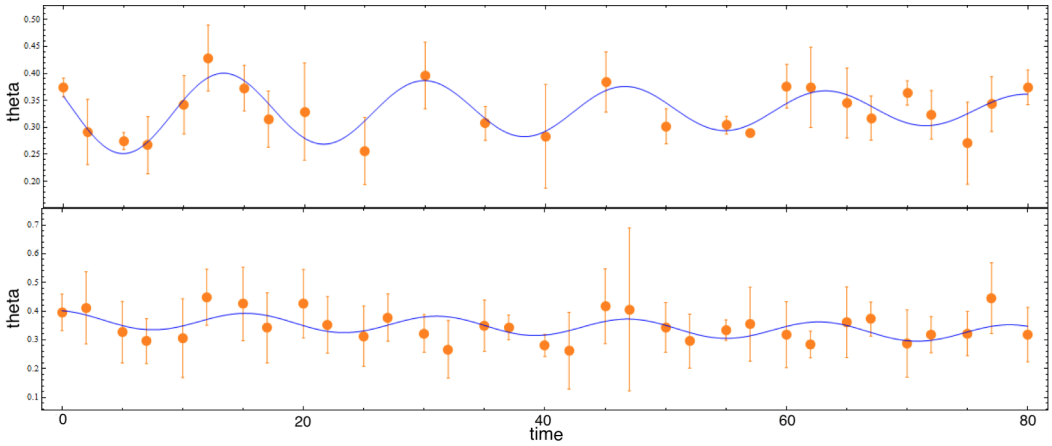

Figure 4.1: **Typical scissors frequencies in a trap with aspect ratio 3:1** Above, a BEC with $\varepsilon_{dd} = 1.3$ oscillates with $\omega_{sc} = 0.93\,\omega_\perp$. Below a SS with $\varepsilon_{dd} = 1.45$ oscillates with $\omega_{sc} = 0.95\,\omega_\perp$. Considering a value of $\omega_\perp \simeq 65$ Hz, this implies a very low difference in the frequency, at the limit of our experimental sensibility of 1-2 Hz.

which we use also to tune the contact interaction, through a Feshbach resonance. Our purpose is to imprint an oscillation of the cloud in the (x, y) plane and let it evolve for a variable time t, to study the evolution of the in-trap angle $\theta(t)$ from which can be extrapolated the scissors frequency ω_{sc}. Since in the supersolid phase different modes are extremely coupled (as shown in section 2.2.3), particular attention has been paid to avoid an excessive excitation of the modes other than scissors. In the following I will describe in detail our excitation scheme.

4.1.1 Choice of experimental parameters

Our purpose is to observe the difference in the rotational inertia I/I_c between the supersolid and a classical system by measuring the scissors frequency. As explained in section 1.2.4, a perfect superfluid rotates with a classical inertia when the value of β approaches unity (equation (2.41)). As predicted from Leggett (section 1.2.4), a supersolid behaves in between a perfect superfluid and a rigid body, since its superfluid fraction is smaller than one. Hence, if we want to appreciate the difference when I/I_c changes from a BEC to a SS, we need to study the scissors oscillation of a BEC only weakly deformed (with $\beta \ll 1$). As discussed in section 3.3.1 we create the condensate using the optical traps ODT1-ODT2, with typical in-plane frequencies $(\omega_x, \omega_y) \simeq 2\pi \times (20, 60)$Hz. The aspect ratio is 3:1, which corresponds to a geometry factor $\alpha = 0.8$. Since for our values of a_s the magnetostriction sets a value of β higher than α, we have that $I/I_c = \beta^2 > \alpha^2$ is very close to one. Hence, when we measure the scissors frequency in the BEC regime, we cannot distinguish it from a rigid body rotation (within our experimental error bar of 1-2 Hz). It will be therefore impossible to experimentally distinguish the rotational inertia of a supersolid from that of a supersolid. In figure 4.1 it is shown the scissors frequency of a BEC and a SS, in this trap configuration. We observe that their frequencies are very similar, namely about

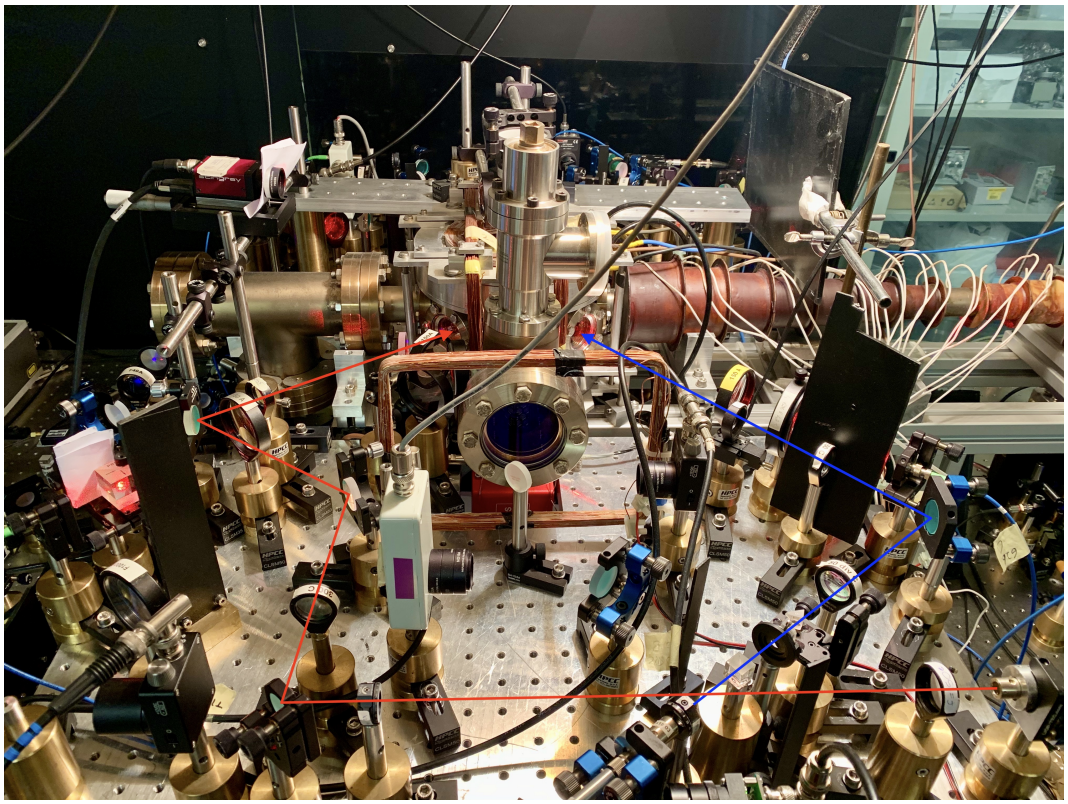

Figure 4.2: **Scheme of the optical beams of ODT2 and ODT3** In blue (red) is showed the path of the beam that generate ODT2 (ODT3) from the optical fiber to the experimental chamber. The trap frequencies are $\omega_{x,y,z} \simeq 2\pi(23,46,90)$ Hz.

$\omega_{sc} \simeq 0.93 \div 0.95\,\omega_{\perp}$. Therefore we need to diminish the value of α by changing the trap frequencies to appreciate a difference in the rotational inertia.

To increase the frequency contrast between the superfluid and the supersolid regime we choose to change the aspect ratio from 3:1 to 2:1. This aspect ratio is achieved with trap frequencies of $(\omega_x, \omega_y) \simeq 2\pi \times (23, 46)$Hz while keeping the confinement along the z-axis unchanged ($\omega_z \simeq 2\pi \times 90$ Hz). Obtaining this aspect ratio with the laser beams ODT1-ODT2 was not possible. Since the two traps are not orthogonal (the angle between them is $\sim 40°$), it is difficult to change independently the frequencies in the plane. Therefore we have chosen to implement a third optical dipole trap (ODT3).

The ODT3 is generated with the same Nd:YAG used for the ODT2. The two optical dipole traps are independently controlled by two different acoustic optical modulators (AOMs), which also detune their wavelengths for avoiding interference between the two beams. They are also both stabilized in power by feedback loops. The waist on the atoms of the ODT3 is 80μm. A picture of the two beams path on the experimental table is is illustrated in figure 4.2.

After the cloud is condensed with the procedure explained in section 3.3.1, we turned on the ODT3 with a 100 ms linear ramp and then and turned off ODT1 with, again, a 100 ms linear ramp. In the new optical trap $\alpha = 0.6$ and the BEC-supersolid transition is located

at $\varepsilon_{dd} = 1.42$ (not at $\varepsilon_{dd} = 1.38$ as in the previous trap). In the BEC regime β varies due to magnetostriction from $\beta = 0.7$ at $\varepsilon_{dd} \sim 1.3$ to $\beta = 0.75$ near the transition line. Beyond the transition, simulations gives a value of $\beta \sim 0.8$ right after the transition up to $\beta \sim 0.95$ near the incoherent droplets transition. Therefore, following equation (2.34) we expect the scissors frequency to fall up to 10% from the BEC to the SS regime.

4.1.2 Excitation methods

After we have the condensate in the traps ODT2 and ODT3, we adiabatically tune the scattering length through Feshbach resonances to the desired value of the interaction parameter ε_{dd} in the range $1.2 \div 1.5$, depending on the phase willing to study. Then we excite the scissors mode imprinting a rotation of the cloud in the (x, y) plane with two different techniques for the BEC and the SS.

The first excitation method consists of switching on momentarily (5 ms) the trap ODT1. The second method excites the scissor mode by changing temporarily (5ms) the intensities of the optical traps ODT2 and ODT3. As the two traps are not perfectly orthogonal ($\theta \simeq 80°$) the atom cloud starts to oscillate. The second method is more gentle than the first one. Let's explain what we intend with this sentence.

The first technique imprints a large amplitude oscillation on the angle, namely about 0.3 rad after the expansion. Hence, it provides a good resolution of the scissors frequency ω_{sc}. Nevertheless it also excites the axial breathing mode of about 20%. In the BEC regime, since the axial breathing mode and the scissors mode are normal modes, the evolution of $\theta(t)$ does not depend on the amplitude of the axial mode [52]. We have proven this supposition by exciting the axial breathing mode in the BEC regime from 10% to 40% finding no shift in the measured scissors frequency, which is always consistent with the prediction (2.40).

In the supersolid phase instead, the two modes are not normal modes, indeed they are coupled and one influences the evolution of the other [11]. We already explained in section 3.3 that the adiabatic crossing of the BEC-SS transition excites the axial breathing mode of about 10%. Interestingly, as it is shown in figure 4.3 (blue points), if we excite the SS with the first method, we see a rise in the scissors frequency toward the BEC value. It looks like the supersolid lattice is averaged out and the system is fully superfluid.

The second method imprints instead a lower amplitude oscillation on the scissors mode, namely about the 50 mrad. Thus, when we excite the SS with this technique, the resolution on the measure of the frequency is lower than the first method. Nevertheless, with a small excitation of the scissors mode, also the axial breathing mode is excited very little. Indeed, we see only a $\sim$10% amplitude oscillation of the latter, as when the scissors oscillation is not excited at all. As it is shown in figure 4.3 (orange points), we observe that when the axial breathing mode is excited by approximately 10% the the scissors frequency decays abruptly in the supersolid phase and is much lower than what is expected for a BEC. These results will be commented more in detail in section 4.3.1.

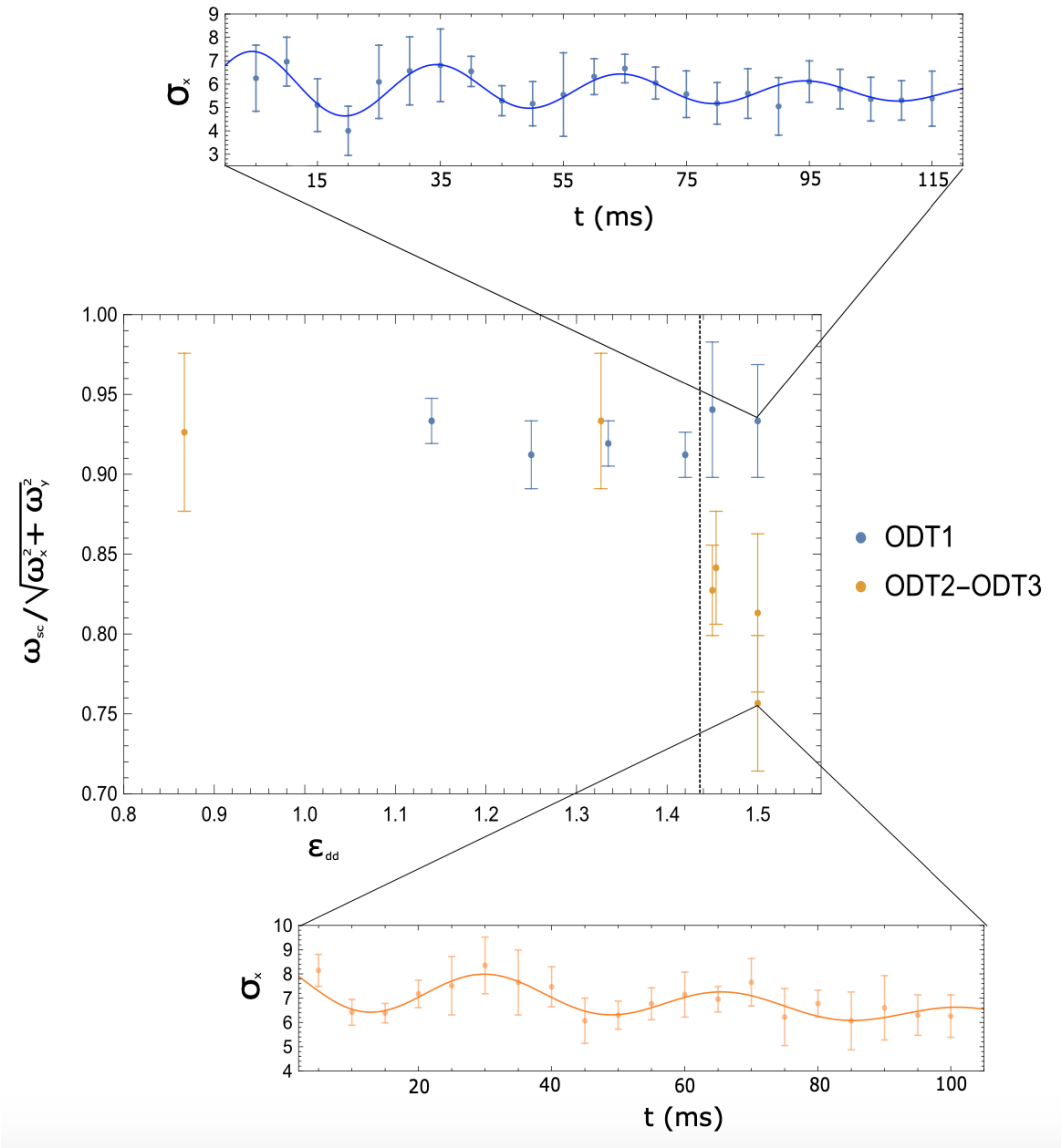

Figure 4.3: **Scissor oscillation with the axial breathing mode:** Here is plotted the scissors frequency vs dipolar interaction strength. The scissors is excited by lighting 5 ms the ODT1 (blue dots) or by changing the intensity of the traps ODT2-ODT3 (orange dots). The scissors excited with the first method oscillates tith the same frequency at the value of a perfect superfluid, while the scissors excited with the second method shows a decrease of the frequency in the SS regime. Above, the supersolid excited with the first method shows an axial breathing amplitude of $\sim 25\%$ and oscillated with a scissors frequency proper of a BEC. Below, when excited with the second method shows an axial breathing amplitude of $\sim 10\%$ and a scissors frequency is lower of about $10 \div 20\%$ from the BEC value. The black dashed line indicates the BEC-SS transition.

4.2 Analysis procedure

To determine the scissors frequency, after the excitation we let the system evolve in trap for a variable time t. Then we turn off the lasers and let the cloud expand. After a fixed expansion time t_{exp} we take absorption imaging and extrapolate the angle $\theta(t)$ by fitting the density distribution after time-of-flight $\tilde{n}(k_x, k_y)$, with the appropriate rotated 2D distribution. An example of typical raw time-of-flight distributions and relative fitting functions is shown in figure 4.4.

4.2.1 Scissors analysis

As we discussed in section 3.3.2 the imaging gives the column density of the cloud, so it is like an effective integration in the z direction. We fit the supersolid with a modulated gaussian in the x direction and a normal gaussian in the y direction. To extract the angle oscillation we are interested in the two dimensional momentum distribution $\tilde{n}(k_x, k_y)$ after the free expansion of the cloud. Since the expansion is isotropic, the angle always changes the same way during the expansion

To fit the angle of the condensate or the supersolid shown in figure 4.4, we transform the coordinates in the lab frame (k_x, k_y) following the usual 2D rigid rotation

- $k_x \to k'_x = k_x \cos\theta - k_y \sin\theta$
- $k_y \to k'_y = k_x \sin\theta + k_y \cos\theta$

The final 2D fitting function is the product of the 1D density modulation (3.16) times a gaussian in the y direction and reads

$$\begin{aligned}\tilde{n}(k'_x, k'_y) = C_0\, e^{-\frac{\left(k_x\cos\theta - k_y\sin\theta\right)^2}{2\sigma_x^2} - \frac{\left(k_x\sin\theta + k_y\sin\theta\right)^2}{2\sigma_y^2}} \times \\ \times\left[1 + C_1\cos^2\left(\frac{k_x\cos\theta - k_y\sin\theta}{k_{rot}}\pi + \phi\right)\right]\end{aligned} \tag{4.1}$$

where the modulation parameters are the same of the fit (3.16) and (σ_x, σ_y) is the width of the cloud after the expansion. With this fit it is now possible to extrapolate the rotation angle θ from the density distribution at a fixed time.

To extract the scissors frequency ω_{sc} we plot the angle oscillation by sampling the in trap evolution time t. The time evolution of the angle $\theta(t)$ after the expansion is fitted with a sinusoide

$$\theta(t) = \theta_0 + A'\cos\left(\sqrt{\omega_{sc}^2 + \tau^{-2}}\, t + \varphi\right)e^{-t/\tau} \tag{4.2}$$

where A' the amplitude after the expansion, τ the damping time, φ the oscillation offset phase and θ_0 is the offset angle between the axis of the trap and the axis of the imaging, constant in every shot.

While the scissors frequency is not affected by the expansion [15], the evolution of the amplification factor A'/A, where A is the in trap amplitude oscillation, depends on the non-trivial change of the shape of the cloud and therefore is not easy to determine.

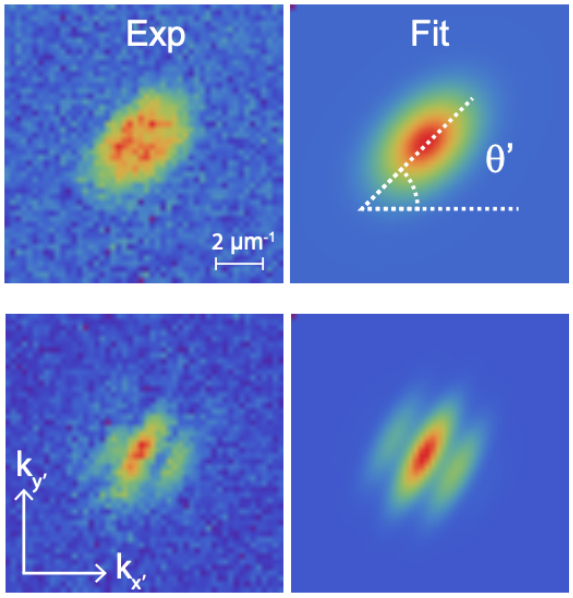

Figure 4.4: **Experiment vs fit:** On the left: images taken with an expansion time of 95 ms. On the right: the correspondent two dimensional fit. Above: an elliptical BEC rotated of an angle θ'. Below: a stripes array typical of the expanded 1D supersolid.

Nevertheless it has been demonstrated that for times $t_{exp} \gg 1/\omega_{sc}$ approaches the value of ~ 2 regardless the trap geometry [54].

An example of the evolution of $\theta(t)$ is shown in figure 4.5 for two different ε_{dd}: in the BEC regime ($\varepsilon_{dd} = 1.2$) and in the supersolid regime ($\varepsilon_{dd} = 1.5$). Each data point in the figure is the average of 4 and 10 images. The maximum time of the oscillation in trap is restricted by the lifetime of the system. As discussed in section 3.3.3 three-body losses is the main contribution that lowers its lifetime. For a BEC the lifetime can be as long as 1000 ms, but for a SS and a DC it is much lower, due to the high density of the droplets. For a BEC is sufficient to study the first 200 ms to have low uncertainty on the scissors frequency, while for a SS because the lifetime does not exceed 100 ms the uncertainty is higher.

4.2.2 Finite temperature analysis

Finite temperature analysis in our system was made for two important reasons. The first and more intuitive reason is to demonstrate that our system is in the collisionless regime. Following the discussion in section 2.3.2, in this regime a thermal cloud oscillates with two frequencies; therefore the emergence of a single frequency in the scissors mode is a direct consequence of superfluidity. The second, and more subtle reason, is to speculate what effects can have the temperature on the scissors frequency of the supersolid.

Creating a "hot" supersolid, i.e., with a large thermal fraction, is in general difficult. We achieve supersolidity only with the coldest condensates, without an observable thermal

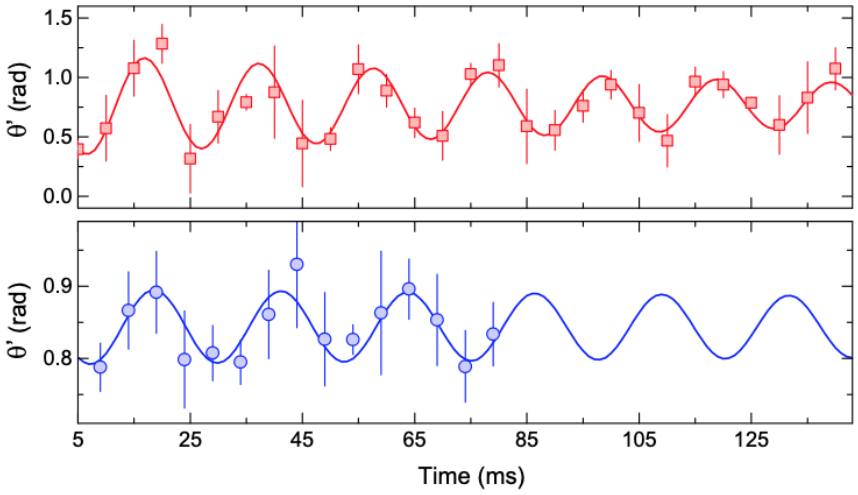

Figure 4.5: **Scissors oscillation of a BEC and a SS:** A scissors oscillation of a BEC (above) and a supersolid (below). For every time t has been taken between 4 and 10 images with a sampling rate of 5 ms. The dots are the weighted average and the line is the fit (4.2), from which it is extrapolated the frequency ω_{sc}. The angle of every distribution has been extrapolated from TOF 2D distribution using the fit (4.1). The lower lifetime of the supersolid is due to three-body losses.

fraction. Moreover, we are not sure that a dipolar supersolid is in thermal equilibrium [7]. Therefore, we perform the thermal analysis in the BEC regime at $\varepsilon_{dd} = 1.14$, where the temperature can be easily measured with the following procedure.

In the imaging process explained in section 3.2.3, when the image is taken after TOF, the sample expands. The velocity distribution of the condensed component follows equation (3.11), while the velocity distribution of the thermal component is a Maxwell-Boltzmann. Therefore, it is possible to extrapolate the temperature from the gaussian width of the thermal cloud with the following relation

$$(\sigma^2(t_{TOF}) - \sigma^2(0)) = \frac{k_B T}{m} t_{TOF}^2 \tag{4.3}$$

where $\sigma(0)$ is the in-trap width. When the thermal fraction is less than $\sim 30\%$ the fitting analysis cannot distinguish the thermal distribution from the condensed distribution and the temperature cannot be measured.

As explained in section 3.2.2 the final temperature of the cloud is controlled by evaporative cooling, hence to get higher temperatures we performed a shorter evaporation procedure. In our trap the BEC transition temperature for a cloud with $\sim 4 \times 10^4$ atoms is $T_c \approx 60\,\mathrm{nK}$. Since the minimum detectable thermal fraction for a BEC is approximately 25%, from equation (2.6) the lower observable temperature is approximately $T \approx 0.6\,T_c \approx 35\,\mathrm{nK}$.

As is illustrated in figure 4.6, for $T < T_c$ no detectable thermal fraction was present, so we measured the scissors frequency only for the superfluid component. The expansion

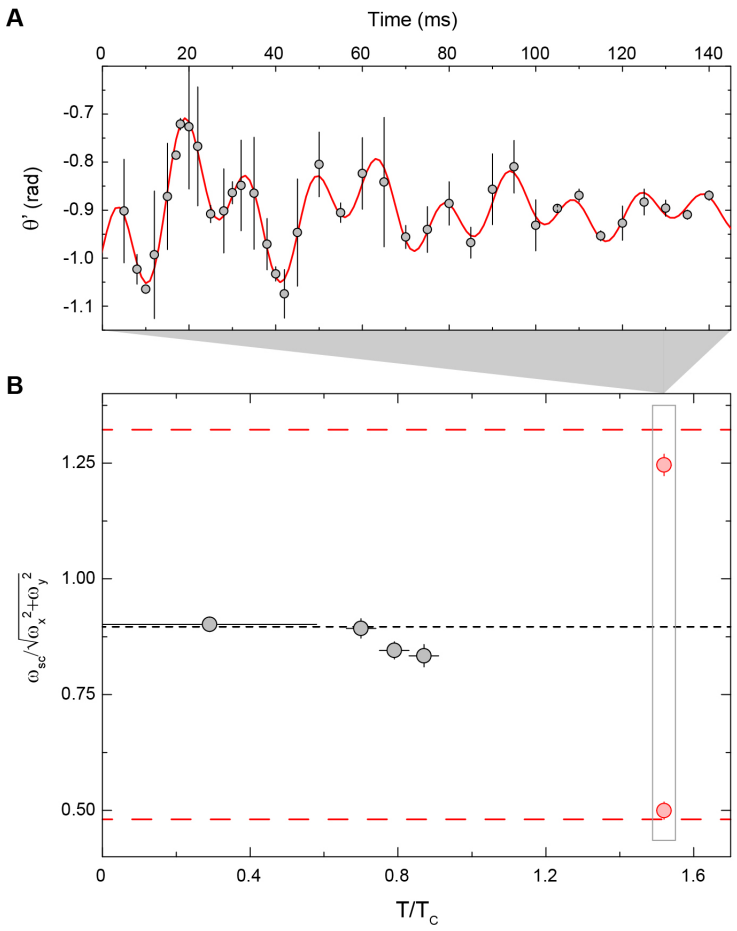

Figure 4.6: **Thermal behaviour: a)** The beats of the two frequencies $\omega_{\pm} = |\omega_x \pm \omega_y|$ of the scissors mode at $T = 1.5\,T_c \approx 90\,\text{nK}$ oscillating around $\theta_0 \sim -0.9$ rad. Using the fit (4.4) we measured $\omega_+ = 66$ Hz and $\omega_- = 25$ Hz, with the same amplitude, implying that the energy is equally distributed between the modes. The damping time τ of a thermal cloud is much larger than in a superfluid. **b)** The scissors frequency is plotted versus the temperature and is normalized with the non dipolar value $\omega_\perp = \sqrt{\omega_x^2 + \omega_y^2}$ (corresponding to $\beta = \alpha$). For the BEC (grey dots) is $\omega_{sc} \sim 0.9\,\omega_\perp$ and increasing the temperature lowers till about a 10% until for $T > T_c$ (red dots) splits into two frequencies. The dashed grey (red) line is the theoretical expected value for a BEC (thermal gas in the collisionless regime).

time was the typical 95 ms. We observed a single frequency at $\omega \simeq 0.9\,\omega_\perp = 2\pi \times 46$ Hz. This result is in very good agreement with equation (2.34) with our experimental parameters. Increasing the temperature the scissors frequency remains unchanged until $T = 0.7\,T_c$. Then it decreases to $\omega \simeq 0.8\,\omega_\perp = 2\pi \times 41$ Hz at $T = 0.8\,T_c$. This decrease in the frequency can be justified as an effect of the interaction with the thermal component [55].

For $T > T_c$ the cloud became thermal. Because of the higher velocities of the particles we needed to decrease the expansion time to 4 ms in order to observe the cloud. We observed two distinct frequencies. As the single frequency fit (4.2) could no longer be used, we used the following two frequencies fit

$$\theta(t) = \theta_0 + A'_+ \cos\left(\sqrt{\omega_+^2 + \tau_+^{-2}}\, t + \varphi_+\right) e^{-t/\tau_+} + A'_- \cos\left(\sqrt{\omega_-^2 + \tau_-^{-2}}\, t + \varphi_-\right) e^{-t/\tau_-} \quad (4.4)$$

from which we extrapolated the frequencies $\omega_\pm \simeq 2\pi \times (66, 25)$ Hz, very close to the expected values for a weakly interacting thermal gas of $\omega_\pm = |\omega_x \pm \omega_y| = 2\pi \times (69, 23)$ Hz. From this analysis we can conclude that the system is in the collisionless regime.

In conclusion, the fact that we see that the scissors frequency of the BEC does not change up to 0.7 T_c, and then decreases only slightly, convinces us that in the supersolid the scissors frequency is not too influenced by temperature. Also, the supersolid is created starting from a BEC with the lower temperature achievable, which is below the observable temperature threshold.

4.3 Results

In the following we will present our experimental results in the BEC an SS regimes of the scissors frequency. We will use the resulting frequencies to estimate the fraction of inertia I/I_c in the supersolid, to quantify the NCRI effects. Finally, we will compare the experimental measure with Leggett's estimation.

4.3.1 Rotational inertia and superfluid fraction

Using the methods explained in sections 4.1.2 and 4.2.1 we are now able to excite and measure the scissors frequency. We performed a series of measurement in a cloud with a typical atom number of $N = 3.5 \times 10^4$, with ε_{dd} ranging from 1.25 to 1.5. The experimental values are plotted in the figure 4.7.a. The frequencies are normalized with the in-plane frequency $\omega_\perp$. As explained in section 3.3.1 the uncertainty on ε_{dd} of about 3%. With our current sensibility on the magnetic field, we can manipulate a_s with Feshbach resonances to sample only two points in the region of the SS: at $\varepsilon_{dd} \sim 1.45$ and at ~ 1.5.

In the BEC regime, for $\varepsilon_{dd} < 1.42$, in the absence of magnetostriction the frequency should be independent from ε_{dd}, with a value of $\omega_{sc} = \omega_\perp$. Instead the elongation along the z-axis increases β and, accordingly to equation (2.34), the system still oscillates with a single frequency (see figure 4.5), but the oscillation frequency decreases to $\omega_{sc} \simeq 0.9\,\omega_\perp$, and it weakly depends on ε_{dd}, in agreement with the mean-field theory, equation (2.1.3). After the BEC-SS transition, at $\varepsilon_{dd} = 1.45$, the frequency clearly reduces of about 10%. This behavior suggests an abrupt increase of the momentum of inertia of the system in the supersolid phase.

The experimental results are compared to the theoretical predictions which simulated a system with atom numbers and trap frequencies similar to our experiment: $\omega_{x,y,z} = 2\pi \times$ (20,40,80)Hz. The scissors frequency is calculated with a sum rule approach [39] and by numerically solving the extended GPE (2.25), with the addition of the rotating

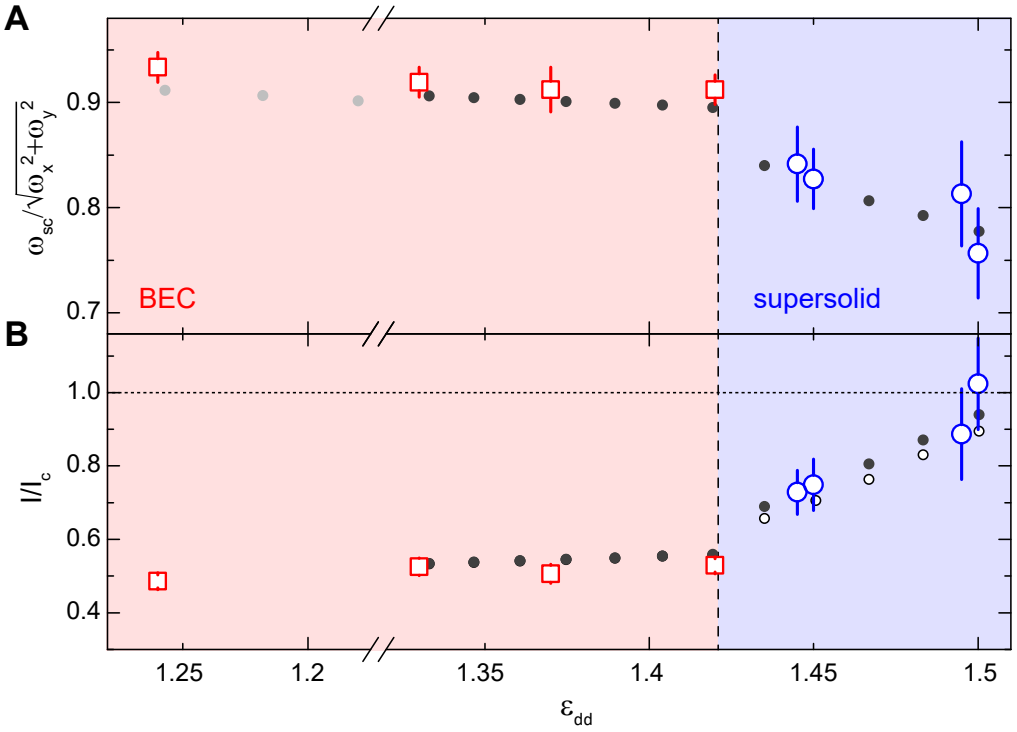

Figure 4.7: **Scissors frequency and fraction of inertia: a)** Here is presented the measured scissors frequency for the BEC (red squares) and the SS (blue dots) along with the numerical prediction by a sum rule approach of the scissors frequency without the LHY therm (grey dots) and with the LHY term (black dots). **b)** The fraction of inertia is obtained using equation (2.40), with the measured scissors frequency and the simulated value of β by the Trento's BEC group [49]. The white dots in the supersolid phase consider only the geometrical factor on the increase of the rotational inertia, while the black dots consider also the decrease of the superfluid fraction. The vertical dashed line separating the BEC and SS regime was determined numerically.

term $-\Omega L_z\psi$. The two approaches give equal results, and are shown as black point in figure 4.7. Remarkably, there is excellent agreement between theoretical and experimental results. The theory gives access also to the system's deformation β. In particular the ground state configuration is determined by evolving the eGPE (2.25) in imaginary time. Both theoretical approaches are only approximations of the real experiment, but they work pretty well when compared with more microscopic (Monte Carlo) simulations [45].

From the measured scissors frequency we determine the fraction of inertia I/I_c though equation (2.40), employing the value of β given by the calculated ground state. We used the value of β given by the theoretical calculated ground state. The resulting values are plotted in 4.7.b. In the BEC regime the momentum of inertia is about half the classical value and is compatible with the expected value for a fully superfluid system, equation (2.41). In the supersolid regime, at $\varepsilon_{dd} = 1.45$, the momentum of inertia increases towards the classical value, however without reaching it. This result provides evidence of non-classical rotational

inertia of the supersolid.

The change of I/I_c is in principle due to both the system's deformation and the decreasing of the superfluid fraction when the supersolid forms. To highlight the change of the superfluid fraction we compared the experimental data of I/I_c in the supersolid regime with the theoretical prediction for a perfect superfluid with the same density distribution (white dots in figure 4.7). More directly, we calculate the superfluid fraction from equation (2.43), employing the experimental frequencies and the theoretical β. The results are shown in figure 4.8. In the BEC regime, using equation (2.43) we observe $f_s = 1$, as expected for a dipolar BEC [51]. In the supersolid regime, we can reliably calculate the superfluid fraction only for the data-points just after the BEC-supersolid transition, at $\varepsilon_{dd} = 1.45$. Remarkably, the superfluid fraction of the supersolid remains very large, $f_s \sim 0.9$. Given the measurement uncertainty, f_s is compatible with unity and incompatible with zero. This result demonstrates the superfluid nature of the dipolar supersolid under rotation.

4.3.2 Comparison with Leggett's model

As shown previously, the superfluid fraction in the supersolid may be lower than one. Here we compare the measured superfluid fraction with the one predicted from Leggett's argument for our system. As discussed in section 1.2.4, in its original argument Leggett considered a supersolid confined in an annulus geometry of length $2\pi R$ much grater than the supersolid unit cell λ, and thickness $d \ll R$, such that the system is effectively one-dimensional. With proper periodic boundary conditions it is possible to unroll the annulus, and the system can be mapped to an infinite 1D line with the symmetry defined by the lattice structure. With this approximation the integral (1.22) is exact when calculated in the unit cell λ.

Our experimental system is very different from the one considered by Leggett, for at least two reasons. 1) We have a three-dimensional cloud confined in a cigar-like trap with a modulation length λ of order of the cloud size. Moreover the rotation is intended in all the (x, y) plane and not only in a 1D annulus, where the curl's superfluid velocity can be finite even without vortices. 2) Leggett's approach does not consider the intrinsic superfluidity of each singular droplet, aspect that may be important near the droplet crystal phase where Leggett's contribution gives vanishing superfluidity. With this considerations we should not expect a strict quantitative prediction from Leggett's argument for our system, but only a qualitative behaviour.

The white triangles of figure 4.8 show Leggett's estimation of the value of Q_0 with our density profile $\rho(x)$, i.e., equation (1.22). We estimated the integral in the grey area of length $l \simeq 5\mu$m between the two central peaks. $\rho(x)$ is obtained integrating the numerical calculated [49] three-dimensional density $\rho(x, y, z)$ in the y and z-directions, and the averaged density is defined as $\langle\rho\rangle = \frac{1}{l}\int_{l/2}^{l/2} \rho(x)dx$. This choice of the interval l is motivated by the necessity of exclude the edges of the system from the calculation, where the inhomogeneity of the trap becomes relevant and both the BEC and the SS result in a vanishing value of Q_0, due to the very low density in those regions. The same procedure is performed in the BEC and SS phase.

In the BEC regime the superfluid fraction is in agreement with the expected value of a perfect superfluid. In the supersolid regime, f_s drops initially to values around 0.25 and decreases further as the system approaches the droplet crystal regime. Such large

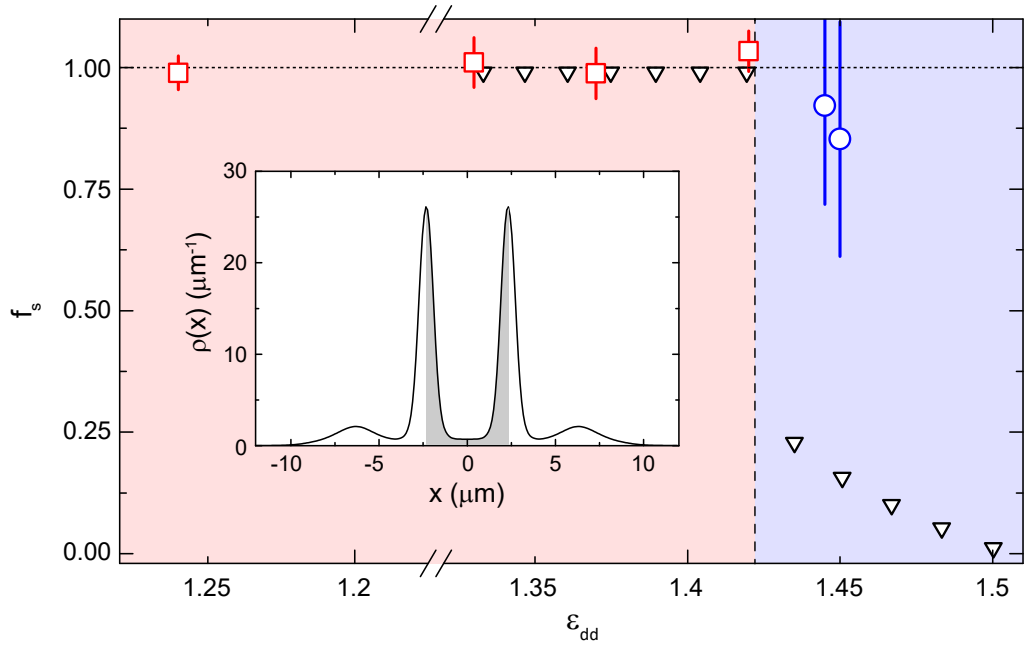

Figure 4.8: **Superfluid fraction from BEC to SS:** Here we present the observed (red squares and blue dots) superfluid fraction of our system and the numerical prediction (white triangles), although the 1D density profile $\rho(x)$ of the supersolid. The large uncertainty on the supersolid regime is mainly due to the denominator contribution $(1-\beta^2)$ of equation (2.43). In the SS phase $\beta \simeq 0.8 \div 0.9$, thus this gives a high value of the standard deviation σ_{f_s} in the calculation of error propagation. On the other hand the simulated values in the SS regime are low due to the low density contribution at the center of the supersolid. The evident different values between the calculated superfluid fraction with our measurements shows the limits of the estimation.

values compared to the helium case are due to the relatively large overlap between density maxima, see the inset of figure 4.8. The values corresponding to the experimental data are $f_s \sim 0.15$, therefore within an order of magnitude from the experimental values.

Conclusion

In conclusion, in this thesis I have established the superfluid nature of the dipolar supersolid by characterizing its non-classical rotational inertia. In particular I observed a reduced moment of inertia (NCRI) when a trapped dipolar supersolid of ^{162}Dy is excited through the scissors mode. From the measured moment of inertia, I infer a superfluid fraction which is different from zero and of the order of unity. Since a perfect superfluid rotates with a momentum of inertia I close to the classical value I_c if its density distribution not cylindrical symmetric, to observe a reduction of the inertia I/I_c from the BEC to the supersolid regime I choose to study the scissors mode of a system only weakly deformed. To achieve such geometry I upgraded the existing experimental setup, implementing new optical potentials for trapping and manipulating the atoms. I then planned and realized the excitation scheme for the scissors mode. To avoid the coupling between the scissors and the axial breathing mode in the supersolid regime, I excited the scissors with a "gentle" kick by changing momentarily the power of the optical trap potentials. I studied the scissors frequency extrapolating the angle oscillation by fitting the expanded column density with a rotating fitting function, consisting of a two-dimensional gaussian with a modulation in the direction of the droplets. Accordingly, the angle is fitted with a sinusoid function. Since three-body losses limits the supersolid lifetime, the oscillation is studied for no more than ~ 100 ms. To better understand the thermal behaviour of the system, I performed thermal analysis in the BEC regime. By studying the oscillation above the BEC critical temperature I demonstrated that our system is in the collisionless regime, confirming the truly superfluid nature of the oscillation below T_c. On the other hand, exciting the scissors oscillation with different superfluid fractions I find no frequency dependence from the temperature below $T = 0.7\,T_c$, suggesting that the presence of a residual thermal component at the typical temperatures of the experiment is irrelevant to the dynamics of the system in the supersolid regime. Note that a similar analysis for the supersolid regime is not possible, since in our setup the supersolid can be formed only at the lowest temperatures. Finally I compared the measured superfluid fraction with the one predicted from Leggett's argument for our system. Considering the two different geometries between our system and Leggett's annular geometry, we find agreement within an order of magnitude.

The supersolid is particularly interesting when compared to standard superfluids, because its reduced superfluid fraction is due to the breaking of the translational invariance, and not to thermal effects. The techniques we have demonstrated, with an improvement of the measurement precision, might allow testing whether the superfluid fraction of the supersolid is indeed smaller than unity. Achieving larger systems might also allow studying

quantitatively the theoretical connection between superfluid fraction and density modulation, as well as observing the appearance of quantized vortices for large angular velocities.

Bibliography

[1] Aleksandr F Andreev and I M Lifshitz. Quantum theory of defects in crystals. *Soviet Physics Uspekhi*, 13(5):670–670, may 1971.

[2] G. V. Chester. Speculations on bose-einstein condensation and quantum crystals. *Phys. Rev. A*, 2:256–258, Jul 1970.

[3] A. J. Leggett. Can a solid be "superfluid"? *Phys. Rev. Lett.*, 25:1543–1546, Nov 1970.

[4] E. Kim and M. H. W. Chan. Probable observation of a supersolid helium phase. *Nature*, 427(6971):225–227, jan 2004.

[5] Duk Y. Kim and Moses H. W. Chan. Absence of supersolidity in solid helium in porous vycor glass. *Phys. Rev. Lett.*, 109:155301, Oct 2012.

[6] Sebastien Balibar. The enigma of supersolidity. *Nature*, 464(7286):176–182, mar 2010.

[7] L. Tanzi, E. Lucioni, F. Famà, J. Catani, A. Fioretti, C. Gabbanini, R. N. Bisset, L. Santos, and G. Modugno. Observation of a dipolar quantum gas with metastable supersolid properties. *Phys. Rev. Lett.*, 122:130405, Apr 2019.

[8] L. Santos, G. V. Shlyapnikov, and M. Lewenstein. Roton-maxon spectrum and stability of trapped dipolar bose-einstein condensates. *Phys. Rev. Lett.*, 90:250403, Jun 2003.

[9] Fabian Böttcher, Jan-Niklas Schmidt, Matthias Wenzel, Jens Hertkorn, Mingyang Guo, Tim Langen, and Tilman Pfau. Transient supersolid properties in an array of dipolar quantum droplets. *Phys. Rev. X*, 9:011051, Mar 2019.

[10] L. Chomaz, D. Petter, P. Ilzhöfer, G. Natale, A. Trautmann, C. Politi, G. Durastante, R. M. W. van Bijnen, A. Patscheider, M. Sohmen, M. J. Mark, and F. Ferlaino. Long-lived and transient supersolid behaviors in dipolar quantum gases. *Phys. Rev. X*, 9:021012, Apr 2019.

[11] L. Tanzi, S. M. Roccuzzo, E. Lucioni, F. Famà, A. Fioretti, C. Gabbanini, G. Modugno, A. Recati, and S. Stringari. Supersolid symmetry breaking from compressional oscillations in a dipolar quantum gas. *Nature*, 574(7778):382–385, 2019.

[12] Mingyang Guo, Fabian Böttcher, Jens Hertkorn, Jan-Niklas Schmidt, Matthias Wenzel, Hans Peter Büchler, Tim Langen, and Tilman Pfau. The low-energy goldstone mode in a trapped dipolar supersolid. *Nature*, 574(7778):386–389, 2019.

[13] G. Natale, R. M. W. van Bijnen, A. Patscheider, D. Petter, M. J. Mark, L. Chomaz, and F. Ferlaino. Excitation spectrum of a trapped dipolar supersolid and its experimental evidence. *Phys. Rev. Lett.*, 123:050402, Aug 2019.

[14] D. Guéry-Odelin and S. Stringari. Scissors mode and superfluidity of a trapped bose-einstein condensed gas. *Phys. Rev. Lett.*, 83:4452–4455, Nov 1999.

[15] O. M. Maragò, S. A. Hopkins, J. Arlt, E. Hodby, G. Hechenblaikner, and C. J. Foot.

Observation of the scissors mode and evidence for superfluidity of a trapped bose-einstein condensed gas. *Phys. Rev. Lett.*, 84:2056–2059, Mar 2000.

[16] L. Tanzi, J. G. Maloberti, G. Biagioni, A. Fioretti, C. Gabbanini, and G. Modugno. Evidence of superfluidity in a dipolar supersolid from non-classical rotational inertia, 2019.

[17] Massimo Boninsegni and Nikolay V. Prokof'ev. Colloquium: Supersolids: What and where are they? *Reviews of Modern Physics*, 84(2):759–776, May 2012.

[18] Anthony James Leggett. *Quantum Liquids*. Oxford University Press, sep 2006.

[19] G. B. Hess and W. M. Fairbank. Measurements of angular momentum in superfluid helium. *Phys. Rev. Lett.*, 19:216–218, Jul 1967.

[20] Anna Eyal, Xiao Mi, Artem V. Talanov, and John D. Reppy. Search for supersolidity in solid 4he using multiple-mode torsional oscillators. *Proceedings of the National Academy of Sciences*, 113(23):E3203–E3212, May 2016.

[21] Ján Nyéki, Anastasia Phillis, Andrew Ho, Derek Lee, Piers Coleman, Jeevak Parpia, Brian Cowan, and John Saunders. Intertwined superfluid and density wave order in two-dimensional 4he. *Nature Physics*, 13(5):455–459, feb 2017.

[22] N. Henkel, R. Nath, and T. Pohl. Three-dimensional roton excitations and supersolid formation in rydberg-excited bose-einstein condensates. *Physical Review Letters*, 104(19), May 2010.

[23] J Lang, F Piazza, and W Zwerger. Collective excitations and supersolid behavior of bosonic atoms inside two crossed optical cavities. *New Journal of Physics*, 19(12):123027, Dec 2017.

[24] Yun Li, Lev P. Pitaevskii, and Sandro Stringari. Quantum tricriticality and phase transitions in spin-orbit coupled bose-einstein condensates. *Physical Review Letters*, 108(22), May 2012.

[25] Zhen-Kai Lu, Yun Li, D.S. Petrov, and G.V. Shlyapnikov. Stable dilute supersolid of two-dimensional dipolar bosons. *Physical Review Letters*, 115(7), Aug 2015.

[26] Julian Léonard, Andrea Morales, Philip Zupancic, Tilman Esslinger, and Tobias Donner. Supersolid formation in a quantum gas breaking a continuous translational symmetry. *Nature*, 543(7643):87–90, Mar 2017.

[27] Jun-Ru Li, Jeongwon Lee, Wujie Huang, Sean Burchesky, Boris Shteynas, Furkan Çağrı Top, Alan O. Jamison, and Wolfgang Ketterle. A stripe phase with supersolid properties in spin–orbit-coupled bose–einstein condensates. *Nature*, 543(7643):91–94, Mar 2017.

[28] Julian Léonard, Andrea Morales, Philip Zupancic, Tobias Donner, and Tilman Esslinger. Monitoring and manipulating higgs and goldstone modes in a supersolid quantum gas. *Science*, 358(6369):1415–1418, Dec 2017.

[29] D. Petter, G. Natale, R.M.W. van Bijnen, A. Patscheider, M.J. Mark, L. Chomaz, and F. Ferlaino. Probing the roton excitation spectrum of a stable dipolar bose gas. *Physical Review Letters*, 122(18), May 2019.

[30] L. Chomaz, R. M. W. van Bijnen, D. Petter, G. Faraoni, S. Baier, J. H. Becher, M. J. Mark, F. Wächtler, L. Santos, and F. Ferlaino. Observation of roton mode population in a dipolar quantum gas. *Nature Physics*, 14(5):442–446, Mar 2018.

[31] Holger Kadau, Matthias Schmitt, Matthias Wenzel, Clarissa Wink, Thomas Maier, Igor Ferrier-Barbut, and Tilman Pfau. Observing the rosensweig instability of a quantum ferrofluid. *Nature*, 530(7589):194–197, 2016.

[32] C. R. Cabrera, L. Tanzi, J. Sanz, B. Naylor, P. Thomas, P. Cheiney, and L. Tarruell. Quantum liquid droplets in a mixture of bose-einstein condensates. *Science*, 359(6373):301–304, 2018.

[33] G. Semeghini, G. Ferioli, L. Masi, C. Mazzinghi, L. Wolswijk, F. Minardi, M. Modugno, G. Modugno, M. Inguscio, and M. Fattori. Self-bound quantum droplets of atomic mixtures in free space. *Phys. Rev. Lett.*, 120:235301, Jun 2018.

[34] D.S. Petrov. Quantum mechanical stabilization of a collapsing bose-bose mixture. *Physical Review Letters*, 115(15), Oct 2015.

[35] Matthias Wenzel, Fabian Böttcher, Tim Langen, Igor Ferrier-Barbut, and Tilman Pfau. Striped states in a many-body system of tilted dipoles. *Physical Review A*, 96(5), Nov 2017.

[36] Q. Beaufils, R. Chicireanu, T. Zanon, B. Laburthe-Tolra, E. Maréchal, L. Vernac, J.-C. Keller, and O. Gorceix. All-optical production of chromium bose-einstein condensates. *Phys. Rev. A*, 77:061601, Jun 2008.

[37] Mingwu Lu, Nathaniel Q. Burdick, Seo Ho Youn, and Benjamin L. Lev. Strongly dipolar bose-einstein condensate of dysprosium. *Phys. Rev. Lett.*, 107:190401, Oct 2011.

[38] K. Aikawa, A. Frisch, M. Mark, S. Baier, A. Rietzler, R. Grimm, and F. Ferlaino. Bose-einstein condensation of erbium. *Phys. Rev. Lett.*, 108:210401, May 2012.

[39] Franco Dalfovo, Stefano Giorgini, Lev P. Pitaevskii, and Sandro Stringari. Theory of Bose-Einstein condensation in trapped gases. *Reviews of Modern Physics*, 71(3):463–512, April 1999.

[40] C.J. Foot. *Atomic physics*. Oxford master series in physics. Oxford University Press, 2005.

[41] C. Pethick and H. Smith. *Bose-Einstein condensation in dilute gases*. Cambridge University Press, 2002.

[42] T Lahaye, C Menotti, L Santos, M Lewenstein, and T Pfau. The physics of dipolar bosonic quantum gases. *Reports on Progress in Physics*, 72(12):126401, nov 2009.

[43] Igor Ferrier-Barbut, Holger Kadau, Matthias Schmitt, Matthias Wenzel, and Tilman Pfau. Observation of quantum droplets in a strongly dipolar bose gas. *Phys. Rev. Lett.*, 116:215301, May 2016.

[44] F. Wächtler and L. Santos. Quantum filaments in dipolar bose-einstein condensates. *Phys. Rev. A*, 93:061603, Jun 2016.

[45] Hiroki Saito. Path-integral monte carlo study on a droplet of a dipolar bose–einstein condensate stabilized by quantum fluctuation. *Journal of the Physical Society of Japan*, 85(5):053001, May 2016.

[46] D. Baillie, R. M. Wilson, R. N. Bisset, and P. B. Blakie. Self-bound dipolar droplet: A localized matter wave in free space. *Phys. Rev. A*, 94:021602, Aug 2016.

[47] T. D. Lee, Kerson Huang, and C. N. Yang. Eigenvalues and eigenfunctions of a bose system of hard spheres and its low-temperature properties. *Phys. Rev.*, 106:1135–1145, Jun 1957.

[48] A. R. P. Lima and A. Pelster. Beyond mean-field low-lying excitations of dipolar bose gases. *Phys. Rev. A*, 86:063609, Dec 2012.

[49] S. M. Roccuzzo, A. Gallemí, A. Recati, and S. Stringari. Rotating a supersolid dipolar gas. *Phys. Rev. Lett.*, 124:045702, Jan 2020.

[50] R. M. W. van Bijnen, N. G. Parker, S. J. J. M. F. Kokkelmans, A. M. Martin, and D. H. J. O'Dell. Collective excitation frequencies and stationary states of trapped dipolar bose-einstein condensates in the thomas-fermi regime. *Phys. Rev. A*, 82:033612, Sep 2010.

[51] G. Hechenblaikner, E. Hodby, S. A. Hopkins, O. M. Maragò, and C. J. Foot. Direct observation of irrotational flow and evidence of superfluidity in a rotating bose-einstein condensate. *Physical Review Letters*, 88(7), Jan 2002.

[52] Moment of inertia and quadrupole response function of a trapped superfluid. 63.

[53] T. Nikuni. Finite-temperature theory of the scissors mode in a bose gas using the moment method. *Physical Review A*, 65(3), Feb 2002.

[54] M. Modugno, G. Modugno, G. Roati, C. Fort, and M. Inguscio. Scissors mode of an expanding bose-einstein condensate. *Phys. Rev. A*, 67:023608, Feb 2003.

[55] Onofrio Maragò, Gerald Hechenblaikner, Eleanor Hodby, and Christopher Foot. Temperature dependence of damping and frequency shifts of the scissors mode of a trapped bose-einstein condensate. *Phys. Rev. Lett.*, 86:3938–3941, Apr 2001.